A Thesis Submitted for the Degree of PhD at the University of Warwick

Permanent WRAP URL:

http://wrap.warwick.ac.uk/88010

Copyright and reuse:

This thesis is made available online and is protected by original copyright.

Please scroll down to view the document itself.

Please refer to the repository record for this item for information to help you to cite it.

Our policy information is available from the repository home page.

For more information, please contact the WRAP Team at: wrap@warwick.ac.uk

warwick.ac.uk/lib-publications

Superconductivity and Magnetism

in

Rare-Earth Nickel Borocarbides

Nicola Juliette Bancroft
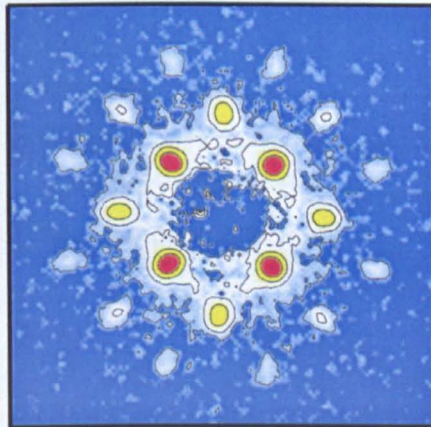
This thesis is submitted in fulfilment of the requirements for the degree of
Doctor of Philosophy in the Department of Physics at the University of Warwick.

September 2002

Contents

List of Figures

i

List of Tables

Acknowledgements

Many people have made important contributions to both the scientific and extra-curricular parts of my world over the last four (and more) years. If you are one, but find that your name does not appear below, this doesn't mean I didn't notice – I just can't mention *everybody*...

Every PhD student needs an interesting research avenue to stroll down and for mine I must thank my supervisor Don Paul. Admittedly, most of the best moments arrived at 4am when I was too exhausted to appreciate them but that's the way it goes in neutron scattering. Life in Superconductivity and Magnetism would have been far less amusing (and getting anything done, far more difficult) without the other members of the crossword consortium: Martin Lees, Geetha Balakrishnan, Martin Davis and John Key; vital support, particularly in the early days, has been provided by my fellow student Emma Chung. Other Warwick people I would particularly like to mention are Andy Howes and Jo Collingwood, both of whom have said the right things at crunch times.

The experiments on D22 would have been very dull (not to mention impossible) without Charles Dewhurst and Bob Cubitt; the work on Y- and $LuNi_2B_2C$ came about through a collaboration with the Birmingham group, primarily involving Ted Forgan, Paul Kealey, Tanya Riseman and Demetris Charalambous. The long hours ramping up to 4T and back on D23 were made almost enjoyable by the humour of Garry McIntyre, at least when his skills weren't urgently needed by 10 other experimental teams at once; fortunately, Jane Austen and Margaret Mitchell (amongst others) kept me entertained the rest of the time. Each instrument was kept in more-or-less working order through the invaluable efforts of the ILL technicians.

Of all my 'real world' friends I would especially like to thank Gemma Stratton and James Ayrton for their ongoing friendship and hospitality, through the good and not-so-good bits and everything in between.

Throughout my life I have been the lucky recipient of steadfast support and encouragement from my immediate family – Mum, Dad, Clair (in her own way), Granny and Grandpa. Without them, and all that they have done, I would almost certainly not be who I am today, or have come this far.

It appears to be traditional to end the acknowledgements with some note about your 'significant other', who will have not only provided love and support but also diligently proof-read the entire thesis on several occasions. Alas Dom has not read a single word of mine, nor been exceptionally helpful in its composition (as those who have encountered my tantrums resulting from his perpetual lateness will know); but he *has* fulfilled the other requirements with ease, and he does cook my dinner every night, and if it was a choice between proof-reading and cooking, I'd choose the food every time!

Declaration

The work presented in this thesis was carried out by me except where stated. The research was carried out in the Department of Physics at the University of Warwick or at the Institut Laue-Langevin, Grenoble, and I was either the sole experimentalist or a leading member of the experimental team. The experiments took place during the period of October 1998 to July 2001. No part of this work has been submitted for examination at any other institution.

Some of the work described in the thesis has been published as:

N.J. Bancroft, D.McK. Paul, G. McIntyre, C.C. Dewhurst & R. Cubitt, '*Magnetism and Superconductivity in ErNi$_2$B$_2$C*', in the Proceedings of the International Symposium on Advances in Superconductivity and Magnetism: Materials, Mechanisms & Devices 2001 [Pramana – Journal of Physics **58** Nos. 5&6 p907 (2002)].

Symbols

Below is a list of symbols used more than once in this thesis; those symbols only used on one occasion are defined at the point of use.

A	Vector potential field
a,b,c	Unit cell lattice vectors
a,b,c	Primary lattice axes
a*,b*,c*	Reciprocal lattice vectors
B	Magnetic induction
B_C, B_{C1}, B_{C2}	Critical fields of superconductors
b	Scattering length
d_{hkl}	Spacing of lattice planes with indices h,k,l
Δ	Superconducting energy gap
E_F	Fermi energy
ε	Local electric field
e	Charge of an electron
F	Free energy
F_s, F_n	Free energy of superconducting/normal state
F_N	Nuclear unit cell structure factor
F_M	Magnetic unit cell structure factor
F_{hkl}	Structure factor associated with reflection hkl
F_{hk}	Fourier coefficient (form factor)
f_{DG}	deGennes factor
Φ_0	Magnetic flux quantum
Φ	Incident neutron flux
ϕ	Scattering angle/instrument axis
ϕ	Order parameter
g_J	Landé g-factor
H	Magnetic field
H_{C1}, H_{C2}	Critical fields of type-II superconductors
H_1, H_2	Critical fields of VL transitions
h,ħ	Planck's constant; $ħ = h/2\pi$
hkl	Miller indices
I	Conduction electron-magnetic moment coupling
I_{hkl}	Integrated intensity
J	Current density
k,k'	Initial and final wave-vectors
κ	Ginzburg-Landau parameter

L	Lorentz correction
L	Bilayer repeat length
l	Electronic mean free path
λ_L	London penetration depth
λ	Penetration depth
λ	Wavelength (also λ_n)
M	Magnetisation
m	Mass of an electron
μ_0	Permeability of free space
μ_B	Bohr magneton
n, n_s	Total and superconducting electron densities
ν	Instrument angle
Q	Scattering vector
q	Modulation wave-vector
θ	Scattering angle/instrument axis
R	Rare-earth element
σ	Neutron scattering cross-section
T	Temperature
T_C	Superconducting transition temperature
T_N	Antiferromagnetic ordering temperature
T_{WF}	Weak ferromagnetic ordering temperature
t	Reduced temperature, T/T_C
τ	Reciprocal lattice vector
V	Sample volume
V_0	Unit cell volume
v	Velocity
Ω	Scattering angle
ω	Crystal rotation angle/instrument axis
ξ	Coherence length
Ψ	Superconducting wave-function

Abbreviations and Units

Å	Angstrom (10^{-10}m)
BCS	Bardeen, Cooper & Schrieffer
emu	Electromagnetic unit
GL	Ginzburg-Landau
ILL	Institut Laue-Langevin
K	Kelvin
μSR	Muon spin rotation
PSI	Paul Scherrer Institute
RKKY	Ruderman-Kittel-Kasuya-Yosida
SANS	Small angle neutron scattering
SDW	Spin density wave
T	Tesla
VL	Vortex lattice
VSM	Vibrating sample magnetometer

Abstract

This thesis describes investigations into the superconducting and magnetic properties of the rare earth nickel borocarbides, RNi_2B_2C. In chapter 1 the field of study is introduced and the basic properties of the materials described. Key theoretical concepts in superconductivity and properties of a vortex lattice are discussed in chapter 2. Chapter 3 describes how crystals are grown and characterised in the laboratory. The theoretical background and experimental techniques used in neutron scattering, the principal tool used in the experiments, are given in chapter 4. An investigation into the magnetic field distribution around vortices through the form factor ratio, F_{11}/F_{10}, in the non-magnetic compounds Y- and $LuNi_2B_2C$, is detailed in chapter 5. It is found that the current theoretical approaches do not provide a good description of this field distribution. Chapter 6 consists of an enquiry into the magnetic structures formed in $ErNi_2B_2C$ both with and without the application of a magnetic field. In zero field the development of a ferromagnetic component at low temperatures is analysed. The response to a magnetic field applied along three distinct crystallographic directions reveals more complicated behaviour than anticipated, including superlattice behaviour in the vicinity of the superconducting upper critical field for two of the orientations. Finally, a survey of the properties of the vortex lattice with applied field and temperature in $ErNi_2B_2C$ is presented in chapter 7. The $90°$ reorientation of the rhombic lattice at a critical field H_1 and the square-to-rhombic symmetry transition at H_2 are investigated. The development of magnetic order is found to have a dramatic impact on the vortex lattice in this material. The principal results arising from this thesis are summarised in chapter 8.

Chapter 1

Introduction

1.1 Fundamental Properties of Superconductors

1.1.1 Early Developments

During the 90 years since the discovery of superconductivity by H. Kamerlingh Onnes[1] the phenomenon has continuously provided new and exciting opportunities for research. Soon after he had first successfully liquefied helium, thereby opening up the possibility of experimentation at lower temperatures than before, Kamerlingh Onnes found that the electrical resistivity of mercury disappeared abruptly below a critical temperature (T_C) of 4.2K. After that initial discovery superconductivity was found in other metals like lead and tin, and in metallic alloys. The critical temperatures of the superconducting elements range from below 1K to 9.5K for niobium, the highest T_C of any element. Later, Meissner and Ochsenfeld[2] demonstrated that when a magnetic field was applied to a superconductor, the magnetic flux was excluded from the interior (figure 1-1). Above a critical field (B_C) the material returns to the normal state. This *Meissner effect* is generally regarded as the true test of whether a material is a superconductor. The flux is expelled regardless of the history of the sample and this is achieved by the circulation of a screening sheet of superconducting electrons ('supercurrent' density $\mathbf{J_s}$) near the surface. The magnetic field created by these currents completely cancels the externally applied field so that the magnetic induction $\mathbf{B}$ is zero deep inside the sample. The critical field is dependent on the temperature, with a maximum value at the limit of zero temperature and falling to zero at T_C. Figure 1-2 shows the thermodynamic phase diagram of such a superconductor, referred to as 'type-I'.

1.1.1 Type-II Superconductors and the Mixed State

In 1957 Abrikosov presented a new solution of Ginzburg-Landau theory for type-II. The state has interesting magnetic properties ...

T > T_C   T < T_C

B

J_s
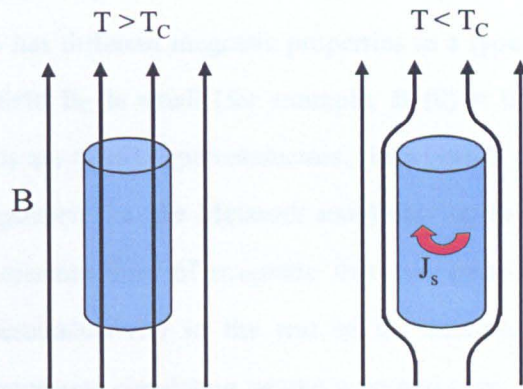
Figure 1-1: The Meissner Effect.

$B_C (T) \cong B_C (0) [1-(T/T_C)^2]$

$B_C (0)$

Normal state

Magnetic Field

Meissner state

0
 0

Temperature $T_C (0)$
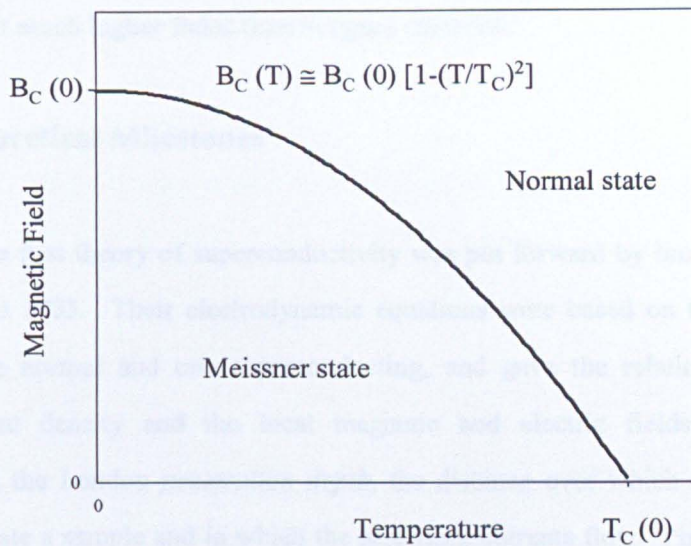
Figure 1-2: Thermodynamic phase diagram of a type-I superconductor.

1.1.2 Type-II Superconductivity and the Vortex Lattice

In 1957 Abrikosov[3] proposed a second class of superconductors that he called type-II. This group has different magnetic properties to a type-I superconductor, in which the critical field B_C is small (for example, $B_C(0) = 0.041T$ for mercury[4]). Most of the elements are type-I superconductors. In a type-II superconductor, there is complete flux expulsion (i.e. the Meissner state) only up to a lower critical field B_{C1}, above which discrete lines of magnetic flux can enter the material without destroying the superconductivity in the rest of the sample. Each flux line is maintained by supercurrents circulating around a normal core. Abrikosov predicted that these vortices would form a regular array - the *flux-line* (or *vortex*) *lattice*. As the applied magnetic field is further increased, more and more vortices enter until their cores overlap and superconductivity is finally destroyed at the upper critical field B_{C2}. The phase diagram of a type-II superconductor is shown in figure 1-3. This 'mixed state' is technologically important because it allows superconductivity to persist at much higher fields than in type-I materials.

1.2 Theoretical Milestones

The first theory of superconductivity was put forward by brothers H. and F. London[5] in 1935. Their electrodynamic equations were based on the idea of two fluids, one normal and one superconducting, and gave the relation between the supercurrent density and the local magnetic and electric fields. The theory introduced the London *penetration depth*, the distance over which magnetic fields can penetrate a sample and in which the screening currents flow. Pippard[6] was able to extend their equations beyond the local limit and in doing so proposed the second characteristic length of a superconductor - the *coherence length*. Later, Ginzburg and Landau[7] published a new theory based on the concept of a superconducting order parameter, similar to the magnetisation in a ferromagnet. In their theory the
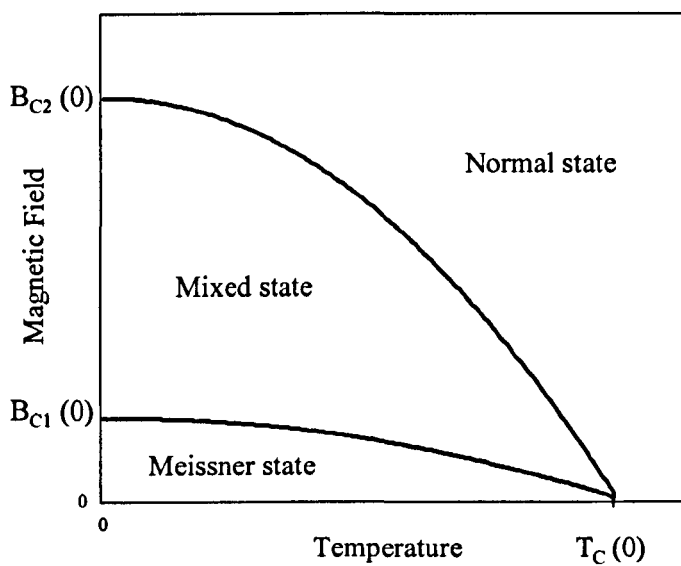
Figure 1-3: Thermodynamic phase diagram of a type-II superconductor.

coherence length relates to the distance over which the order parameter can vary. A landmark microscopic theory was put forward in 1957 by Bardeen, Cooper and Schrieffer[8]. They postulated that in the superconducting state, electrons form pairs (Cooper pairs), mediated by lattice vibrations (phonons). Because of this proposed pairing mechanism, the theory set an upper limit on critical temperatures of around 30K. It is well known that since the 1980's superconductivity has been found in materials with much higher T_C's, such as $YBa_2Cu_3O_7$ ($T_C \sim 92K$)[9]. Despite much effort, no theory of high temperature superconductivity has yet been globally accepted.

1.3 Magnetism and Superconductivity

Superconductivity is a surprisingly common property, and was observed early on in many metallic elements and alloys but not in those containing magnetic ions such as iron. Even trace amounts of paramagnetic impurities in known superconductors could cause a severe reduction in T_C or even prevent superconductivity entirely. The arrival of the BCS theory improved the understanding of why superconductivity was suppressed or destroyed by magnetic impurities – the local magnetic moments could break up the Cooper pairs; this is known as magnetic pair breaking. However, this work on added impurities did not really shed light on the interaction between superconductivity and *long range* magnetic order, due to the inhomogeneous distribution of the magnetic impurity atoms.

In the latter half of the 1970's superconductivity was discovered in several families of rare earth ternary compounds even though those systems contained magnetic rare earth atoms arranged on a regular lattice. The first reported were the molybdenum chalcogenides, RMo_6S_8 (R = rare earth element) in 1975[10] and then RMo_6Se_8 (1976)[11], followed by the rhodium borides RRh_4B_4 (1977)[12]. Since then

superconductivity has been discovered in other magnetic materials including several compounds of uranium, such as UPt_3[13]. In most cases, the magnetic ordering is antiferromagnetic in nature, so that zero net magnetisation is seen over the superconducting length scales, and the magnetic ordering temperature is lower than the superconducting transition temperature; for example, $TmRh_4B_4$ exhibits superconductivity below 10K and orders antiferromagnetically below 0.4K. Very often the development of this antiferromagnetic order results in the suppression (or sometimes even enhancement, as in the case of $SmRh_4B_4$) of the upper critical field in the superconducting phase. In cases where ferromagnetic ordering occurs, such as $ErRh_4B_4$, the effect is more severe and superconductivity is destroyed at the Curie temperature; this is known as re-entrant superconductivity. Typical data are shown in figure 1-4. Extensive research has been carried out into these families of materials, as well as those discovered since, such as the rare-earth rhodium tin compounds, to further the understanding of the microscopic coexistence of long range magnetic order and superconductivity. A review of the properties of these materials is given by Maple[14].

1.4 Rare-Earth Nickel Borocarbides - RNi₂B₂C

1.4.1 Introduction

In 1994 two separate research groups reported superconductivity in quaternary systems: Nagarajan *et al.*[15] in Y-Ni-B-C (T_C up to 12K) and Cava *et al.*[16] in Y-Pd-B-C (T_C to 23K). These materials showed transition temperatures higher than those usually seen in intermetallic compounds. The superconducting phase in the nickel based materials was determined to be YNi_2B_2C with $T_C = 16.6K$[17]. Superconductivity was observed not only in the non-magnetic Y- and Lu- materials, but also for the magnetic rare earth elements Ho, Er, Tm, and eventually Dy[18]. The discovery of these materials invoked intense interest. With a range of magnetic and
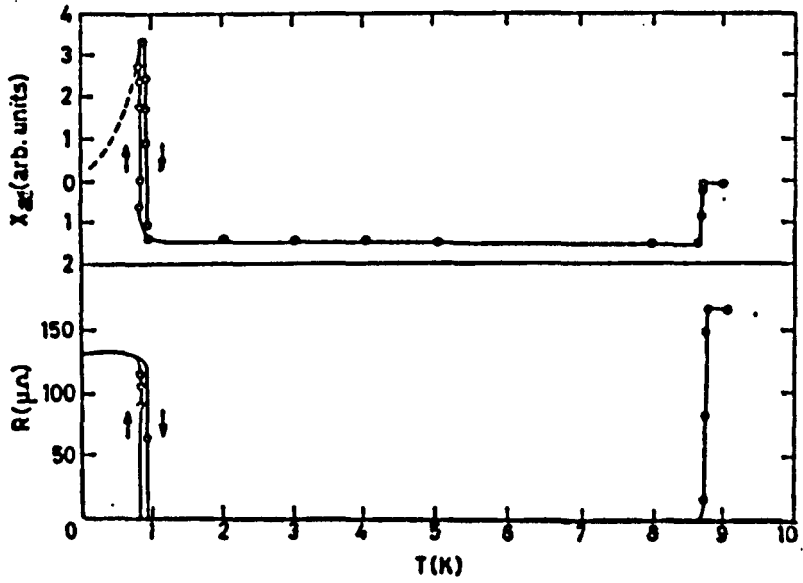
Figure 1-4: Susceptibility and resistance of the ferromagnetic superconductor $ErRh_4B_4$. Reproduced from reference 12.

non-magnetic materials with transitions at temperatures easily accessible to the laboratory researcher, the borocarbides are an excellent system with which to experiment. The preparation of single crystal samples is relatively straightforward[19] compared to the materials discovered previously. In addition, while the Ho-, Er- and Tm- compounds, like the majority of magnetic superconductors, order magnetically at temperatures below the superconducting transition, $DyNi_2B_2C$ unusually has $T_N >$ T_C. Thus the borocarbide materials provide a new system in which to test the understanding gained from previous work, and an opportunity to extend this understanding further. The principal transition temperatures of selected RNi_2B_2C compounds are listed in table 1.1.

R	$T_C(K)$	$T_N(K)$
Y	15.6	-
Lu	16.5	-
Dy	6	10.5
Ho	8.5	8
Er	10.5	6
Tm	11	1.5

Table 1.1: Transition temperatures of some RNi_2B_2C compounds

1.4.2 Crystal Structure

Siegrist *et al.*[20] reported that the crystal structure of $LuNi_2B_2C$ consists of alternating layers of Lu-C and Ni-B, not unlike the layered structures of other superconductors such as the high-T_C cuprates. The crystal structure is body centred tetragonal (space group I4/mmm) as shown in figure 1-5. The structure was later found to be the same for all R[21]. In these materials, any magnetic properties are usually attributed solely to the rare earth elements (see below) with the Ni carrying no magnetic moment[21]. The superconductivity is generally believed to be due to the Ni 3*d* electrons[22]; the layered crystal structure, keeping the magnetic components
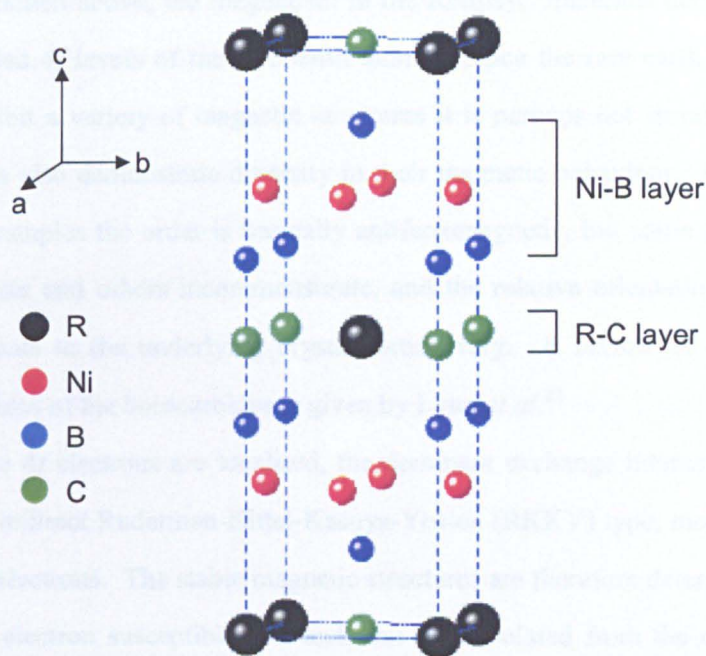
Figure 1-5: Crystal structure of the RNi$_2$B$_2$C family showing a single unit cell.

separate from the superconducting paths, is therefore vital in permitting the two antagonistic phenomena to coexist on a microscopic level.

1.4.3 Magnetic Order

As mentioned above, the magnetism in the RNi_2B_2C materials derives from the partially filled $4f$ levels of the rare earth atoms. Since the rare earth elements themselves exhibit a variety of magnetic structures it is perhaps not surprising that the borocarbides also demonstrate diversity in their magnetic behaviour. For all of the magnetic examples the order is basically antiferromagnetic, but some structures are commensurate and others incommensurate, and the relative orientations of the magnetic moments to the underlying crystal lattice vary. A review of the basic magnetic structures of the borocarbides is given by Lynn *et al.*[21]

Since the $4f$ electrons are localised, the dominant exchange interaction is of the long range, indirect Ruderman-Kittel-Kasuya-Yosida (RKKY) type, mediated by the conduction electrons. The stable magnetic structures are therefore determined by the conduction electron susceptibility, which can be calculated from the electronic band structure. Rhee *et al.*[23] examined the electronic band structure of $LuNi_2B_2C$ and found maxima in the susceptibility for wave-vectors of (0.6,0,0) and (0,0,0.9), close to the wave-vectors observed in the structures of magnetic borocarbides such as $HoNi_2B_2C$.

For an RKKY type interaction the antiferromagnetic ordering temperature T_N depends on the coupling between the conduction electrons and rare earth moments, I, and the quantum numbers of the $4f$ shell via the de Gennes factor f_{dG} which is

$$f_{dG} = (g_J - 1)^2 J(J+1) \qquad (1.1)$$

where

$$g_J = 1 + \frac{J(J+1) + S(S+1) - L(L+1)}{2J(J+1)} \qquad (1.2)$$

The temperature dependence of T_N is given by

$$T_N \propto I^2 f_{dG} \qquad (1.3)$$

For the borocarbides I is roughly constant across the series, so that T_N should vary linearly with f_{dG}; this is observed experimentally[24].

Magnetic order has been reported for R = Dy, Ho, Er and Tm, which are also superconductors, and R = Nd, Pr, Tb, Gd and Sm. These have mostly been investigated by neutron diffraction, except for the Gd and Sm materials, whose structures were determined by magnetic x-ray scattering as those rare-earths are highly absorbent to neutrons. Two of the most interesting compounds are the superconducting Ho- and $ErNi_2B_2C$, both of which reveal changes in the magnetic ordering as the temperature is further cooled below T_N. For R = Ho, an incommensurate spiral along the c-axis forms below $T_N = 8K$, but over the range 5-6K there is a second incommensurate spiral along a. Below 5K these spirals collapse into a commensurate structure where the moments are ferromagnetically aligned along the [1 1 0] direction, and these planes are antiferromagnetically coupled along c[21]. In $ErNi_2B_2C$, an incommensurate, transversely polarised spin density wave is formed below $T_N = 5.8K$[25,26]. The propagation wave-vector is along the a-axis, with the moments lying along b, as shown in figure 1-6. It has also been reported[27] that a ferromagnetic component forms below 2.3K; this component is the subject of the first part of chapter 6 of this thesis.

A common feature of the magnetic borocarbides is that they undergo changes in magnetic structure (metamagnetic transitions) when they are subjected to magnetic fields. The critical fields of these transitions vary both with temperature and with the relative orientation of the crystal to the applied field[28]. The metamagnetic behaviour of $ErNi_2B_2C$ is investigated in the second part of chapter 6.

Figure 1-6: Magnetic structure of $ErNi_2B_2C$ below $T_N = 5.8K$ over a magnetic unit cell (top) and the arrangement over a crystal unit cell (bottom). Only the fundamental harmonic of the spin density wave is illustrated.

1.4.4 Superconductivity in RNi_2B_2C

As has already been mentioned, superconductivity has been observed in two non-magnetic variants, Y- and $LuNi_2B_2C$, as well as in several magnetic compounds. The occurrence of superconductivity in the non-magnetic compounds is very useful as it allows the effects of magnetic order on superconductivity to be separated from the intrinsic superconducting properties of these materials. The superconductivity itself is generally considered to be conventional, i.e. phonon mediated (BCS-like), in nature. The higher critical temperatures of the non-magnetic examples (table 1.1) indicate that the magnetism in these materials suppresses T_C as might be expected. This suppression, ΔT_C, should from theory be related (as are the T_N) to the de Gennes factor via

$$\Delta T_C \propto - I^2 N(E_F) f_{dG} \qquad (1.4)$$

where $N(E_F)$ is the density of electronic states at the Fermi surface. Since $N(E_F)$ is, like I, approximately constant across the RNi_2B_2C series, this again gives a linear relation between ΔT_C and f_{dG}, which is roughly what is seen experimentally[29].

The magnetic compounds also have considerably reduced upper critical fields when compared to their non-magnetic counterparts. Typical published values of B_{C2} for $LuNi_2B_2C$ are around 7T for fields applied along the c-axis[30]; the comparable value for the magnetic Er material is around 1.5T. There is some anisotropy in these materials, with the critical fields dependent on whether the field is applied along the c-axis or within the ab plane; however this anisotropy is small compared to the very large differences found in, for example, the high-T_C cuprates[31]. For those specimens with $T_N < T_C$ (R = Ho, Er, Tm) the development of magnetic order at T_N causes additional suppression[29] of B_{C2}. This is seen most clearly in $HoNi_2B_2C$ and to a lesser extent in $ErNi_2B_2C$, and is attributed to magnetic pair breaking. The degree of suppression is also anisotropic, as shown for the Er compound[32] in figure 1-7. This is perhaps not surprising, since the magnetic moments have a preferred orientation and so the magnetically ordered state is obviously highly anisotropic itself.
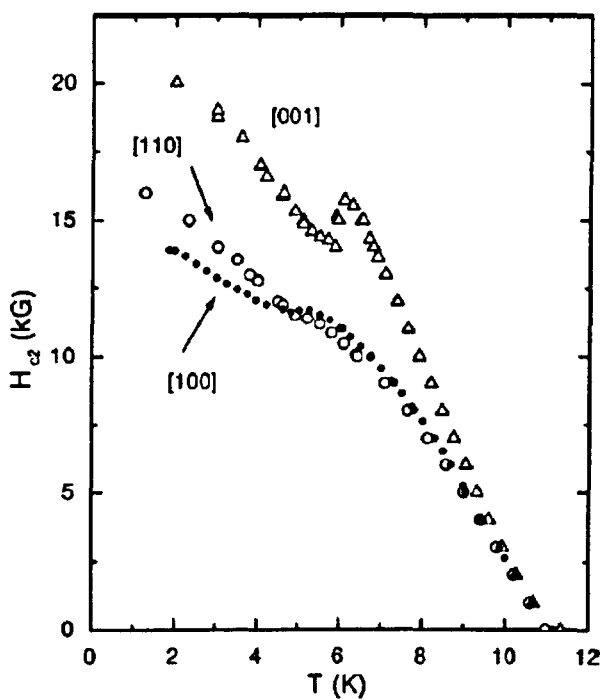
Figure 1-7: Variation of the upper critical field of $ErNi_2B_2C$ with temperature for magnetic fields applied along different directions. Reproduced from reference 32.

The magnetic order in these materials also impacts on the superconductivity in a more subtle way. In real materials, in the mixed state ($B_{C1} < B < B_{C2}$) vortices may become stuck or *pinned* to features such as defects in the crystal structure. In the borocarbides, which are type-II superconductors, it has been observed that the presence and type of magnetic order affect the degree of pinning. In HoNi$_2$B$_2$C[33] pinning is noticeably stronger in the narrow temperature range 5-6K in which the magnetic order includes a spiral along the *a*-axis, compared to the temperature regions above and below this zone which do not have this particular spiral. Pinning also increases significantly below T_N in the Er compound[34] (again, an *a*-axis modulated structure) and shows a further increase at temperatures below 2.3K where a ferromagnetic component is proposed to develop[35]. These features show how intricately the magnetic behaviour and superconductivity are interwoven.

1.4.5 The Vortex Lattice in RNi$_2$B$_2$C

The superconducting members of the RNi$_2$B$_2$C family show unusual behaviour in the mixed state. In 'high' magnetic fields, applied along the crystal *c*-axis, the lattice symmetry is square[36,37], in contrast to the majority of superconductors in which the expected hexagonal lattice is formed. If the applied field is reduced the lattice changes its symmetry to that of a rhombic (i.e. distorted hexagonal) lattice. In the rhombic phase there are two domains oriented at 90° to each other. The square lattice and square-to-rhombic symmetry transition were observed first in the magnetic Er compound[38], but this atypical behaviour is not caused by the magnetic order since it occurs in the non-magnetic Y- and Lu variants[39,40]. The properties of the mixed state in the non-magnetic compounds are examined in chapter 5 of this thesis. The behaviour of the vortex lattice in the magnetic ErNi$_2$B$_2$C, including its reaction to the onset of magnetic order at T_N, is the subject of chapter 7.

References

[1]   H. Kamerlingh Onnes, Commun. Leiden Comm. **120b** (1911)

[2]   W. Meissner & R. Ochsenfeld, Naturwissenschaften **21** 787 (1933)

[3]   A.A. Abrikosov, Sov. Phys. JETP **5** 1174 (1957) [English translation of Zh. Eksp. Teor. Fiz **32** 1422 (1957)]

[4]   N.W. Ashcroft & N.D. Mermin, *Solid State Physics* (Saunders College Publishing 1975)

[5]   F. & H. London, Proc. Roy. Soc. A **149** p24 (1935)

[6]   A.B. Pippard, Proc. Roy. Soc. A **216** p547 (1953)

[7]   V.L. Ginzburg & L.D. Landau, Zh. Eksp. Teor. Fiz **20** p1064 (1950) (in Russian)

[8]   J. Bardeen, L.N. Cooper & J.R. Schrieffer, Phys. Rev **108** p1175 (1957)

[9]   M.K. Wu *et al.*, Phys. Rev. Letts. **58** No. 9 p908 (1987)

[10]   A.L. Fischer *et al.*, S.S.Comms. **17** p721 (1975)

[11]   R.N. Shelton *et al.*, Phys. Lett. A **56** p213 (1976)

[12]   W.A. Fertig *et al.*, Phys. Rev. Lett. **38** p987 (1977)

[13]   G.R. Stewart *et al.*, Phys. Rev. Lett. **52** p679 (1984)

[14]   M.B. Maple, Physica B **215** p110 (1995)

[15]   R. Nagarajan *et al.*, Phys. Rev. Lett **72** p274 (1994)

[16]   R.J. Cava *et al.*, Nature **367** p146 (1994)

[17]   R.J. Cava *et al.*, Nature **367** p252 (1994)

[18]   C.V. Tomy *et al.*, Physica C **248** p349 (1995)

[19]   B.K. Cho *et al.*, Phys. Rev. B **52** p3684 (1995)

[20]   T. Siegrist *et al.*, Nature **367** p254 (1994)

[21]   J.W. Lynn *et al.*, Phys. Rev. B **55** No. 10 p6584 (1997)

[22]   L.C. Gupta, Physica B **223** p56 (1996)

[23]   J.Y. Rhee *et al.*, Phys. Rev. B **51** No. 21 p15585 (1995)

[24]   P.C. Canfield *et al.*, Physics Today (October 1998)

[25]   J. Zarestky *et al.*, Phys. Rev. B **51** p678 (1995)

[26]   S.K. Sinha *et al.*, Phys. Rev. B **51** p681 (1995)

[27]   P.C. Canfield *et al.*, Physica C **262** p249 (1996)

[28]   P.C. Canfield & S.L. Bud'ko, J. Alloy. Comp. **262** p169 (1997)

[29]   H. Eisaki *et al.*, Phys. Rev. B **50** p647 (1994)

[30]   K.D.D. Rathnayaka *et al.*, Phys. Rev B **55** No. 13 p8506 (1997)

[31]   D.R. Tilley & J. Tilley, *Superfluidity and Superconductivity* (I.O.P 1996)

[32]   S.L. Bud'ko & P.C. Canfield, Phys. Rev. B **61** No.22 p14932 (2000)

[33]   C.D. Dewhurst *et al.*, Phys. Rev. Letts. **82** No.4 p827 (1999)

[34]   C.D. Dewhurst *et al.*, Phys. Rev. B **63** p60501 (2000)

[35]   P.L. Gammel *et al.*, Phys. Rev. Letts. **84** No.11 p2497 (2000)

[36]   U. Yaron *et al.*, Nature **382** p236 (1996)

[37]   M. Yethiraj *et al.*, Phys. Rev. Letts. **78** No.25 p4849 (1997)

[38]   M.R. Eskildsen *et al.*, Phys. Rev. Letts. **78** No.10 p1968 (1997)

[39]   D.McK. Paul *et al.*, Phys. Rev. Letts. **80** No.7 p1517 (1998)

[40]   M.R. Eskildsen *et al.*, Phys. Rev. Letts. **78** No. 3 p487 (1997)

Chapter 2

Superconductivity

2.1 Introduction to the Theories of Superconductivity

More detailed treatments of these theories are provided by the references and texts listed in the bibliography at the end of this chapter.

2.1.1 The London Equations

London and London[1] proposed a theory of the electrodynamics of superconductors that explained the observations that had been made at the time: perfect conductivity and the Meissner effect. Their theory followed the two-fluid concept, in which a fraction of the total conduction electron density is superconducting, i.e. this fraction is not scattered by impurities or defects. In Gorter and Casimir's two fluid model[2] the superconducting fraction n_s is zero above T_C, and increases smoothly below T_C until it reaches the total electron density n.

The two London equations are

$$\varepsilon = \mu_0 \lambda_L^2 \frac{d}{dt} \mathbf{J_s}$$
(2.1)

and

$$\mathbf{h} = -\lambda_L^2 \nabla \wedge \mathbf{J_s}$$
(2.2)

where ε and $\mathbf{h}$ are the *local* electric and magnetic fields respectively, $\mathbf{J_s}$ is the supercurrent density and μ_o is the permeability of free space. The parameter λ_L in the constant of proportionality for both equations is defined by

$$\lambda_L^2 = \frac{m}{\mu_0 n_s e^2}$$
(2.3)

where m and e are the mass and charge of the electron. With the hindsight provided by the microscopic BCS theory, substituting m by 2m, e→2e and n_s→n_s/2 still reduces to 2.3.

The first London equation (2.1) describes perfect conductivity since an electric field accelerates the superconducting electrons freely rather than simply maintaining their velocity against resistance as in a normal metal. The second (2.2) describes the Meissner effect. Substituting in Maxwell's equation $\mathbf{J} = \nabla \wedge \mathbf{h}$ we obtain

$$\nabla^2 \mathbf{h} = \frac{\mathbf{h}}{\lambda_L^2} \qquad (2.4)$$

A homogenous magnetic field cannot be a solution of this equation unless the applied field is zero. For the classic example of a superconductor-vacuum boundary (figure 2-1), with a magnetic field H_0 applied parallel to the side of a slab, the solution to 2.4 gives the field inside the superconductor

$$h = H_0 \exp\left(- x/\lambda_L\right) \qquad (2.5)$$

This shows that the magnetic field falls off inside the superconductor over a length λ_L, which can now be identified as the London penetration depth. Within this distance from the edge of the slab, supercurrents flow that create a field inside the superconductor that exactly cancels the applied field – the Meissner effect. Within the two-fluid model, the predicted variation of n_s with temperature, $n_s \propto 1\text{-}t^4$ (where t = T/T_C), which is in good agreement with experimental data, leads to a temperature dependence of the penetration depth of the form

$$\lambda(T) = \frac{\lambda(0)}{\sqrt{\left(1 - t^4\right)}} \qquad (2.6)$$

The behaviour of the London penetration depth with temperature is shown in figure 2-2.

Both of the London equations, 2.1 and 2.2, are encapsulated within a relation between $\mathbf{J_s}$ at a particular point and the vector potential $\mathbf{A}$ at that point which can be imagined as a replacement of Ohm's law for a superconductor:
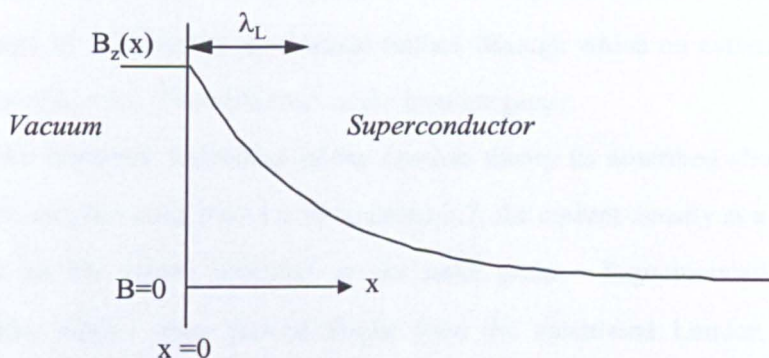
Figure 2-1: Magnetic field penetration into a superconductor at an interface with vacuum showing the London penetration depth λ_L.
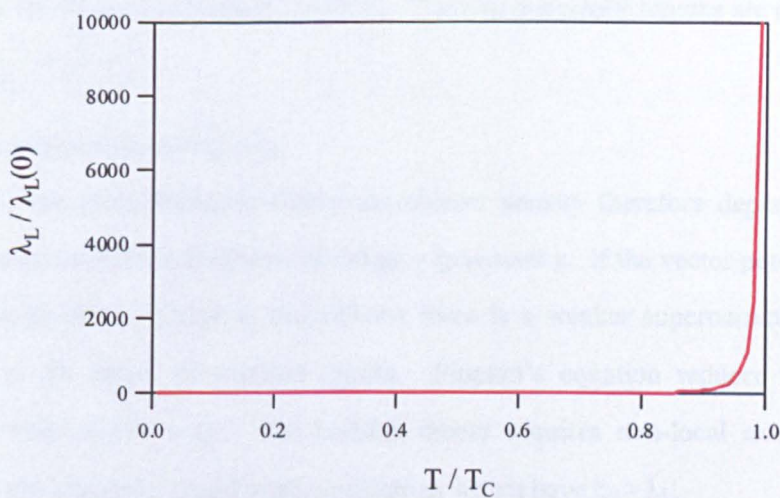
Figure 2-2: Variation of the penetration depth with temperature in the London two-fluid approach.

$$J_s = -\frac{1}{\mu_0 \lambda_L^2} A \qquad (2.7)$$

where the gauge of A in 2.7 is specified: the divergence is zero ($\nabla . A = 0$) and the component of A normal to an external surface through which no external current is fed is zero ($A_n = 0$). This is known as the London gauge.

An important restriction of the London theory as described above is that it considers only the *local limit* i.e. in equation 2.7, the current density at a point r *only* depends on the vector potential *at the same point*. Experimentally measured penetration depths often proved longer than the calculated London penetration depths. Pippard also found that the penetration depth increased as the mean free path *l* decreased in alloys by changing the amount of impurity. As a result, Pippard[3] proposed a non-local replacement of the London equation

$$J(r) = \frac{1}{\mu_0 \lambda^2} \frac{1}{\xi_0} A(r) \qquad (2.8)$$

which introduced an intrinsic coherence length of the pure material, ξ_0. He also provided the Pippard coherence length ξ_P. The two coherence lengths are related by

$$\frac{1}{\xi_P} = \frac{1}{\xi_0} + \frac{1}{l} \qquad (2.9)$$

In a pure superconductor $\xi_P = \xi_0$.

In the electrodynamic theory the current density therefore depends on the vector potential field in a volume of radius $\sim \xi_P$ around r. If the vector potential does not maintain its full value in this volume there is a weaker supercurrent response leading to the larger penetration depths. Pippard's equation reduces to a local relation when $\lambda_L(T) \gg \xi_P$. The London theory requires non-local extensions to describe the elemental type-I superconductors, which have $\xi_0 > \lambda_L$.

2.1.2 Ginzburg-Landau Theory

Ginzburg and Landau[4] published a phenomenological theory of superconductivity based on Landau's work on second order phase transitions. The true value of the theory was not appreciated fully until Gor'kov[5] proved that the GL theory was a limiting case of the microscopic (BCS) theory under particular conditions – the temperature must be close to T_C and variations of the superconducting wave-function, ψ, not too rapid. The GL theory has the advantage over the London theory that it can cater for spatial variations in n_s and fields large enough to change it.

In the absence of a magnetic field the transition from the normal state to the superconducting state is of second order. Landau[6] had previously developed a theory of the thermodynamics of second order phase transitions based on an order parameter that is zero above the critical temperature and non-zero below, such as the spontaneous magnetisation in a ferromagnet. The first assumption of his theory is that the free energy below the critical temperature can be expanded in terms of the order parameter ϕ as

$$F = F_n + \alpha\,\phi^2 + \frac{\beta}{2}\phi^4 \qquad (2.10)$$

where F_n is the free energy of the normal state. The second assumption is that the coefficients α and β are functions of temperature. Their temperature dependences are found by examining the value of ϕ at the minimum of the free energy (ϕ_0), i.e. when

$$\frac{\partial F}{\partial \phi} = \alpha\,\phi_0 + \beta\phi_0^{\,3} = 0 \qquad (2.11)$$

which has solutions $\phi_0 = 0$ and $\phi_0^{\,2} = -\alpha/\beta$. The requirements are that $\phi_0 = 0$ is the only solution above T_C and $\phi_0 \neq 0$ is the only solution below T_C. Landau used

$$\alpha(T) = a(T\text{-}T_C) \qquad (2.12)$$

$$\beta(T) = \beta$$

where a and β are positive constants. Figure 2-3 shows the variation of the free energy with ϕ using these temperature dependences. For $T > T_C$ the minimum free energy is for $\phi = 0$; below T_C minima occur at $\pm\,\phi_o$ as required.

Ginzburg and Landau suggested a similar order parameter for the superconducting state and used a superconducting wavefunction ψ. Adjustments to the original theory are necessary as in general the order parameter must now be a function of position, and the coupling of the supercurrents and magnetic field must be taken into account. The modulus $|\psi^*\psi|^2$ is related to the number of superconducting electrons, n_s.

The basic postulate of the GL theory applied to superconductivity was to write the free energy as

$$F_s(r,T) = F_n(r,T) + \alpha|\psi|^2 + \frac{\beta}{2}|\psi|^4 + \frac{1}{2m^*}\left|\left(-i\hbar\nabla - e^*A\right)\psi\right|^2 + \frac{\mu_0 h^2}{2} \quad (2.13)$$

where subscripts s and n denote the superconducting and normal state respectively. The temperature dependences of the parameters α and β are the same as in Landau's original theory. The modulus, $|\psi|$, is used because ψ is a complex quantity. If ψ is zero $(T > T_C)$ only the first and last terms remain - these are the normal state free energy and magnetic energy as expected. If there are no fields or gradients ($\nabla\psi$ and A are zero) we have just

$$F_s(r,T) - F_n(r,T) = \alpha|\psi|^2 + \frac{\beta}{2}|\psi|^4 \quad (2.14)$$

The right hand side is the first two terms in a power expansion of the condensation energy, in terms of $|\psi|^2$; this is sufficient in the region near to T_C. The remaining term in 2.13 is just the kinetic energy of a particle with wavefunction ψ. In light of the BCS theory, with pairs of electrons forming the 'superconducting carriers', we know $m^* = 2m$ and $e^* = 2e$. The effect of the gradient term is to prevent ψ from varying too rapidly. An important consequence of the Ginzburg-Landau approach is that the wave function cannot vary over lengthscales smaller than
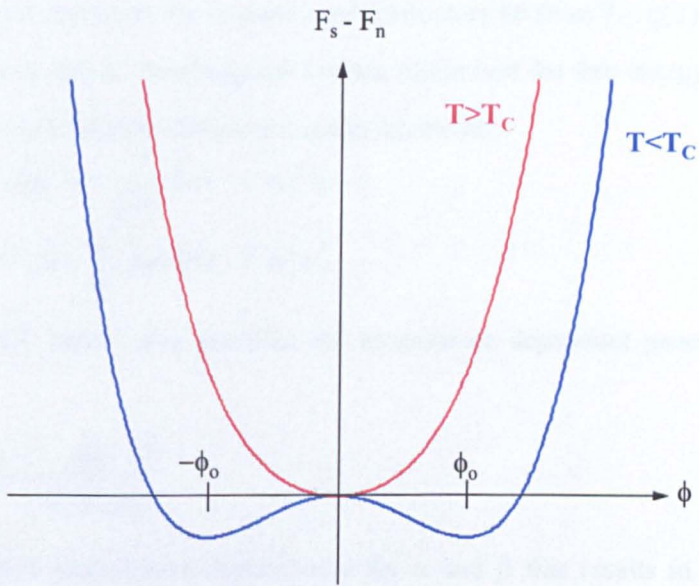
Figure 2-3: Variation of the condensation energy F_s-F_n with wave-function ϕ using the Ginzburg-Landau temperature dependences.

$$\xi(T) = \left(\frac{\hbar^2}{2m|\alpha|}\right)^{\frac{1}{2}} \tag{2.15}$$

Thus $\xi(T)$ is the temperature dependent coherence length (figure 2-4) that sets a minimum spatial extent over which ψ can vary, such as the radius of a vortex core in the mixed state. It is not the same coherence length as that used by Pippard in the electrodynamic approach, but in pure superconductors far from T_C, $\xi(T) \approx \xi_0$.

To determine ψ and $\mathbf{A}$, Ginzburg and Landau minimised the free energy with respect to ψ and $\mathbf{A}$ to produce the Ginzburg-Landau equations:

$$\alpha\psi + \beta|\psi|^2\psi + \frac{1}{2m^{\bullet}}\left(i\hbar\nabla - e^{\bullet}\mathbf{A}\right)^2\psi = 0 \tag{2.16}$$

$$\mathbf{J} = \nabla \wedge \mathbf{h} = \frac{e^{\bullet}}{m^{\bullet}}\left[\psi\left(-i\hbar\nabla - e^{\bullet}\mathbf{A}\right)\psi\right] \tag{2.17}$$

The GL theory also provides the temperature dependent penetration depth given by

$$\lambda(T) = \left(\frac{m\beta}{4e^2\mu_0|\alpha|}\right)^{\frac{1}{2}} \tag{2.18}$$

Using Landau's temperature dependences for α and β this results in $\lambda \propto (1-t)^{-1/2}$. Near to T_C this has the same form as Gorter and Casimir's $(1-t^4)^{-1/2}$. An important parameter arising from the GL theory is the ratio of the two characteristic lengths, known as the Ginzburg-Landau parameter:

$$\kappa = \frac{\lambda(T)}{\xi(T)} \tag{2.19}$$

From the definitions of λ and ξ, κ is independent of temperature, and it is the measure of whether a material is a type-I or type-II superconductor (section 2.2).
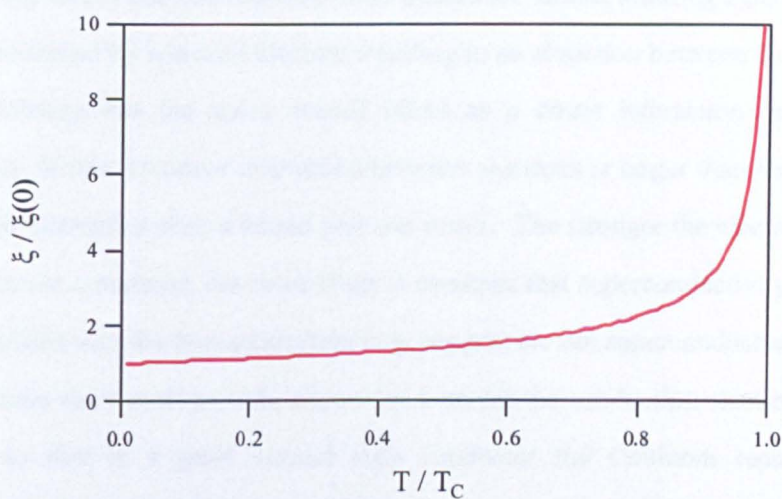
Figure 2-4: Variation of the Ginzburg-Landau coherence length with temperature.

2.1.3 BCS Theory

The BCS theory of superconductivity[7] was the first to propose a mechanism by which superconductivity could occur - the pairing of electrons, mediated by vibrations of the underlying crystal lattice (phonons). The importance of the lattice had been suggested experimentally by the observation of the isotope effect[8], where the critical temperature varies with atomic mass as $T_C \propto M^{-a}$ where a ~ 0.5. The underlying idea is that one electron could disturb the lattice, emitting a phonon which is later absorbed by a second electron resulting in an attraction between the electrons. This exchange has the same overall effect as a direct interaction between the electrons. If this attractive interaction between electrons is larger than the repulsive Coulomb interaction then a bound pair can result. The stronger the electron-phonon interaction in a material, the more likely it becomes that superconductivity can exist. This explains why the best conductors (e.g. copper) are not superconductors; for high conductivity there must be little interaction between the conduction electrons and the lattice, so that in a good normal state conductor the Coulomb repulsion will overcome any electron-electron attraction.

The simplified potential used in the BCS theory can be written as

$$V_{k,k'} = -V \qquad |E_k| < \hbar\omega_D \text{ and } |E_{k'}| > \hbar\omega_D \qquad (2.20)$$

$$0 \qquad \text{otherwise}$$

where ω_D is the Debye frequency for the phonons. This describes the interaction between two electrons whose energies (measured from E_F) are within $\hbar\omega_D$ of the Fermi surface energy E_F. As $\hbar\omega_D$ is always much smaller than E_F, this shell around the Fermi surface is very thin. The interaction turns out to be strongest when the electrons have equal but opposite momenta (i.e. $\hbar k$ and $-\hbar k$) giving zero momentum of the centre of mass. Through symmetry arguments Cooper found that the two electrons in the pair had opposite spins. The wave-function of the pair is spatially symmetric, like an atomic s-orbital: the pairing state is referred to as s-wave, spin singlet.

18

The BCS ground state is very different to the normal ground state. In the normal ground state all available states are filled up to the Fermi energy E_F. In the BCS ground state there are unoccupied states below E_F and occupied states above it, but the reduction in energy gained via the condensation energy of a pair outweighs the increased kinetic energy. The theory also includes an energy gap Δ, which corresponds to the energy needed to break an electron pair. The energy of any excited states must be at least $E_o+\Delta$, where E_o is the ground state energy. The existence of this energy gap in superconductors is borne out experimentally; for example, in absorption spectra, a photon whose energy is smaller than the energy gap cannot be absorbed. If the effect of a magnetic field is to be considered, the gap becomes a function of position $\Delta(r)$. Δ plays the role of the wave-function in the BCS theory.

The BCS theory successfully explained why magnetic impurities are so damaging to superconductivity. The interaction of the Cooper pair with the impurity spin causes a difference in energy between the two electrons because of the different orientations of their spins relative to the impurity atom spin. If this energy difference is greater than the binding energy of the electron pair then no pairs can survive and superconductivity cannot occur.

2.2 The Mixed State in Superconductors

2.2.1 General Properties of the Vortex Lattice

Type-II superconductivity occurs in materials that have $\lambda \gg \xi$. For applied magnetic fields between the upper and lower critical fields, B_{C1} and B_{C2}, the sample admits magnetic flux in the form of flux-lines (vortices). A vortex consists of a normal core of radius $\sim \xi$, around which currents flow over a radius $\sim \lambda$. Inside the vortex, the superconducting wave-function is zero (figure 2-5). Such a vortex is
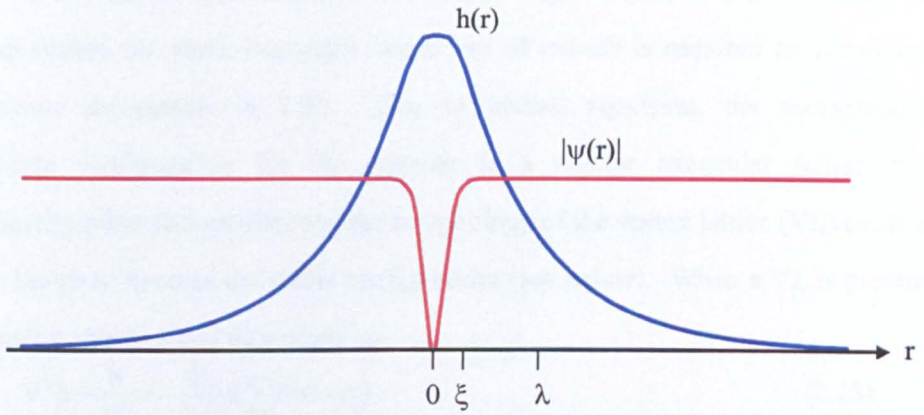
Figure 2-5: Variation of magnetic field and superconducting wave-function for an isolated vortex.

impossible in a type-I superconductor where $\lambda \ll \xi$. Each vortex carries one quantum of magnetic flux denoted Φ_0 where

$$\Phi_0 = \frac{h}{2e} = 2.07 \times 10^{-15} \text{ Tm}^{-2} \tag{2.21}$$

The magnetic field structure of a single vortex in the London limit ($\xi \rightarrow 0$) is described by

$$h(r) = \frac{\Phi_0}{2\pi \lambda^2} K_0\left(\frac{r}{\lambda}\right) \tag{2.22}$$

where K_0 is a zeroth order Hankel function. At higher fields, where the density of vortices makes the cores important, some sort of cut-off is required to curtail the logarithmic divergence in 2.22. Due to mutual repulsion, the energetically favourable configuration for the vortices is a regular triangular lattice, but occasionally other factors affecting the morphology of the vortex lattice (VL) cause a square lattice to become the stable configuration (see below). When a VL is present the London equation can be written[9] as

$$\nabla^2 h - \frac{h}{\lambda^2} = -\frac{\Phi_0}{\lambda^2} \hat{z} \sum_r \delta(r - r_i) \tag{2.23}$$

where the applied field (and therefore the flux-lines) are along the z-direction; r_i is the position of the ith vortex and $\hat{z}$ is a unit vector along z.

A VL comprised of equilateral triangles is in reality not often observed. Generally, there is some distortion; this often due to the anisotropy in the underlying crystal structure, which is introduced to theoretical models by incorporating a second rank mass tensor which reflects the different effective electron masses along the crystal axes. Both the penetration depth and coherence length will vary depending on the direction in which the magnetic field is applied, leading to anisotropic vortices and VL morphologies.

In any real superconductor there will be places in the material where a vortex may become stuck or *pinned*. Additional energy is required to move the pinned vortex away from such a site. There are many different possible pinning sites such as crystal defects and twin boundaries. In the borocarbides pinning is also affected by

magnetic structures[10,11]. Pinning can be detected through magnetisation measurements, since it affects the movement of vortices in or out of the sample on varying the applied magnetic field, leading to hysteresis. Pinning can also hinder the movement of flux-lines caused by the application of a transport current (via the Lorentz force) up to a depinning critical current; since the movement of vortices leads to energy dissipation, this is important for potential applications of superconductors.

2.2.2 The Vortex Lattice in RNi$_2$B$_2$C Materials

In some systems, under appropriate conditions, a square VL is observed. This is the case in the superconducting RNi$_2$B$_2$C compounds[12-14] when a magnetic field applied along the c-axis exceeds a critical value denoted H$_2$. Below H$_2$ a rhombic (i.e. distorted triangular) lattice exists, which itself undergoes a 45° reorientation relative to the crystal lattice at a lower field value H$_1$. This behaviour has been approached theoretically by introducing non-local corrections to both the GL and London theories.

Non-locality becomes important in clean high-κ materials (such as the borocarbides) where the electronic mean free path l is large compared to the coherence length ξ. Kogan[15] introduced a third length scale called the 'non-locality range', related to both l and ξ. Its magnitude determines how close vortices must be for non-local effects to become important. In dirty materials where the mean free path is small, the non-local effects vanish. In YNi$_2$B$_2$C it has been shown experimentally that the non-locality causes a four-fold distortion of the supercurrents around the vortex core[16]. This distortion leads to anisotropy in the inter-vortex interactions, so that when vortices become sufficiently close-packed the square lattice becomes the stable configuration. Kogan[17] has extended the London model to included non-local corrections and computed the minimum in the free energy under different conditions to find the stable VL structures. This approach successfully

predicts the square-to-rhombic transition as well as the low field reorientation of the rhombic lattice. The rhombic phases are degenerate with respect to a 90° rotation when the field is applied along the c-axis, so that two domains are formed. Since the mean free path is expected to decrease with increasing temperature this leads to a predicted increase in H_2, at which the (2nd order) transition from rhombic to square symmetry occurs. The behaviour close to T_N (where the London model is invalid) has been approached by making non-local corrections to the Ginzburg-Landau theory by Park and Huse[18], who predicted that the H_2 line should intersect the upper critical field H_{C2}.

References

[1]   F. and H. London, Proc. Roy. Soc. A **149** p24 (1935)

[2]   C.J. Gorter & H.D.B Casimir, Physica **1** p306 (1934)

[3]   A.B. Pippard, Proc. Roy. Soc. A **216** p547 (1953)

[4]   V.L. Ginzburg & L.D. Landau, Zh. Eksp. Teor. Fiz **20** p1064 (1950) (in Russian)

[5]   L.P. Gor'kov, Sov. Phys. JETP **9** p1364 (1959) [English translation of Zh. Eksp. Teor Fiz. **36** p1918 (1959)]

[6]   L.D. Landau Phys. Z. Sowjet **11** p545 (1937)

[7]   J. Bardeen *et al.*, Phys. Rev. **108** p1175 (1957)

[8]   E. Maxwell, Phys. Rev. **78** p477 (1950); C.A. Reynolds *et al.*, Phys. Rev. **78** p487 (1950)

[9]   M. Tinkham, *Introduction to Superconductivity* (McGraw-Hill 1975)

[10]   C.D. Dewhurst *et al.*, Phys. Rev. Letts **82** No. 4 p827 (1999)

[11]   C.D. Dewhurst *et al.*, Phys. Rev. B **63** p60501 (2002)

[12]   U. Yaron *et al.*, Nature **382** p236 (1996)

[13]   M.R. Eskildsen *et al.*, Phys. Rev. Letts. **78** No. 3 p487 (1997)

[14]   M. Yethiraj *et al.*, Phys. Rev. Letts. **78** No. 25 p4849 (1997)

[15]   V.G. Kogan *et al.*, Phys. Rev. B **54** No. 17 p12386 (1996)

[16]   M. Yethiraj *et al.*, Phys. Rev. B **58** No. 22 pR14767 (1998)

[17]   V.G. Kogan *et al.*, Phys. Rev. B **55** No. 14 pR8693 (1997)

[18]   K. Park & D.A. Huse, Phys. Rev. B **58** No. 14 p9427 (1998)

Additional Bibliography

D.R. Tilley & J. Tilley, *Superfluidity and Superconductivity* (I.O.P 1996)

M. Cyrot & D. Pavuna, *Introduction to Superconductivity and High-T_C Materials* (World Scientific 1992)

C.P. Poole *et al.*, *Superconductivity* (Academic Press 1995)

Chapter 3

Crystal Growth and Characterisation

3.1 Single Crystal Growth

Single crystals of RNi_2B_2C are grown using a high temperature flux method with Ni_2B as the flux. This technique has been used extensively to grow these compounds - see for example Cho *et al*[1]. Pellets of RNi_2B_2C are prepared by arc-melting stoichiometric quantities of the constituent elements on a water-cooled hearth under flowing argon. The arc furnace is shown schematically in figure 3-1. Before each melt the chamber is evacuated and refilled with argon at least three times to provide an inert atmosphere, and before melting the sample materials a piece of titanium is melted to remove any remaining oxygen. The purity of each of the constituent elements used is 99.9% or higher.

A sphere of Ni metal is first melted alone as some mass is lost at this stage. The mass of the Ni piece after this melting is used to calculate the quantities of the other elements required. The first element added is boron. Enriched boron (^{11}B) is used if the crystals are intended for neutron scattering experiments as ^{10}B strongly absorbs neutrons. Pieces of the appropriate rare earth metal and finally fragments of carbon are added. After each melting the sample is weighed to ensure that enough of the added materials are taken into the pellet; this is particularly important when adding the ^{11}B which is supplied in powdered form and tends to fly away when the arc is brought near. In each case the amount of material added is within 3% of the correct stoichiometric quantity. After adding the final constituents, the pellet is turned and re-melted several times to encourage a homogeneous composition. The

Electrode

Argon
out

Tungsten
tip

Quartz
window

To
pump

Argon
in

Titanium
piece

Hearth

Materials to be
melted
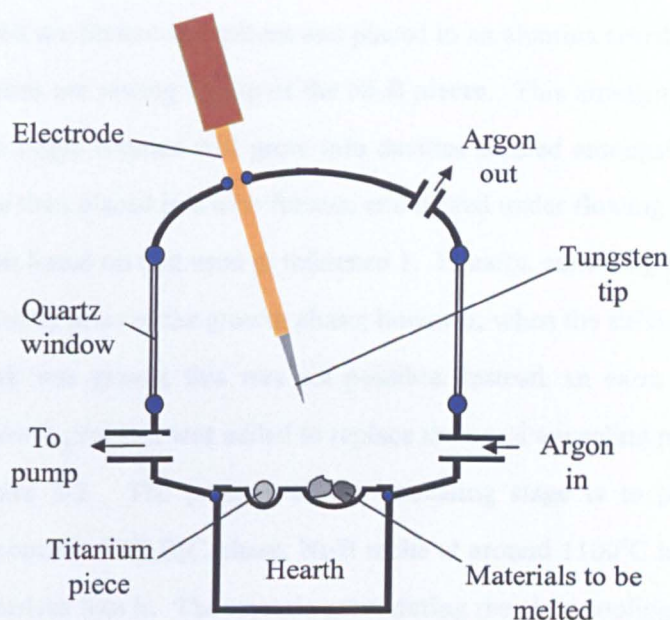
Figure 3-1. Schematic representation of the argon arc furnace.

final pellet has a typical mass of 5-7g. Pellets of Ni_2B of similar mass are also produced by this method.

The pellets are broken into pieces and placed in an alumina crucible such that the RNi_2B_2C pieces are resting on top of the Ni_2B pieces. This arrangement is used in the hope that single crystals will grow into cavities formed amongst the pieces. The crucibles are then placed in a tube furnace and heated under flowing argon using a growth program based on that used in reference 1. Usually, annealing at 1050°C is carried out separately prior to the growth phase; however, when the $ErNi_2B_2C$ crystal used in this work was grown, this was not possible. Instead, an extra 'annealing' section of the growth program was added to replace the usual annealing procedure as indicated in figure 3-2. The purpose of the annealing stage is to promote the formation of the correct RNi_2B_2C phase. Ni_2B melts at around 1100°C and some of the RNi_2B_2C dissolves into it. The crystals grow during the slow cooling from 1490 to 1200°C. The resulting crystals are plate-like and are either embedded in the surface of the flux or (more usefully) growing out from the surfaces into a cavity. The crystals can then be cut out from the flux using a diamond wheel saw and a wire saw for more delicate cuts. The resulting crystals are characterised using x-ray Laue photography and magnetisation measurements; this process is made considerably simpler by the natural tendency of the crystals to grow with the *c*-axis perpendicular to the plate surface.

3.2 Magnetisation Measurements

The magnetisation measurements described in this thesis were carried out using an Oxford Instruments vibrating sample magnetometer (VSM). The basic idea of VSM measurements is to detect an a.c. voltage generated in sense coils by the sample in response to being vibrated inside an applied magnetic field. The experimental set-up is shown in figure 3-3[2]. A superconducting solenoid inside the
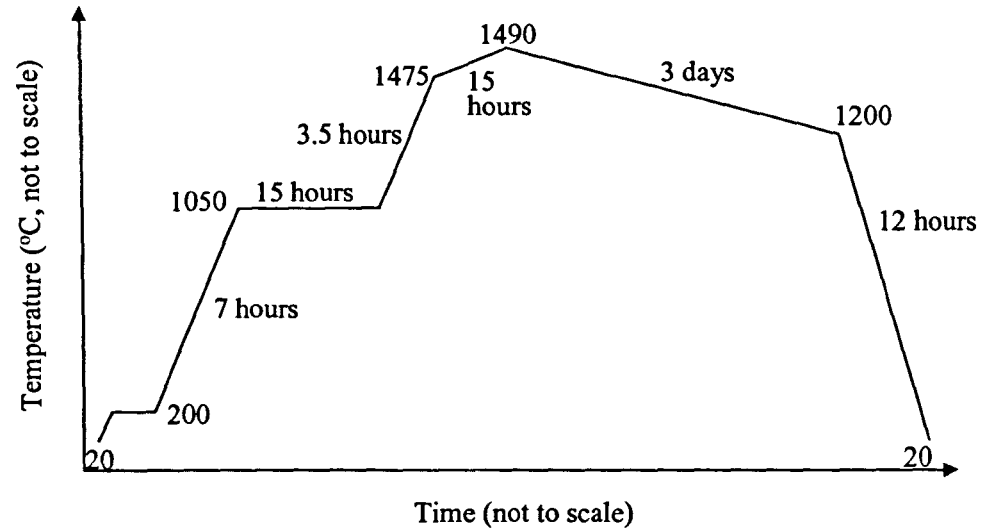
Figure 3-2. Temperature cycle used in growth of ErNi$_2$B$_2$C crystals.
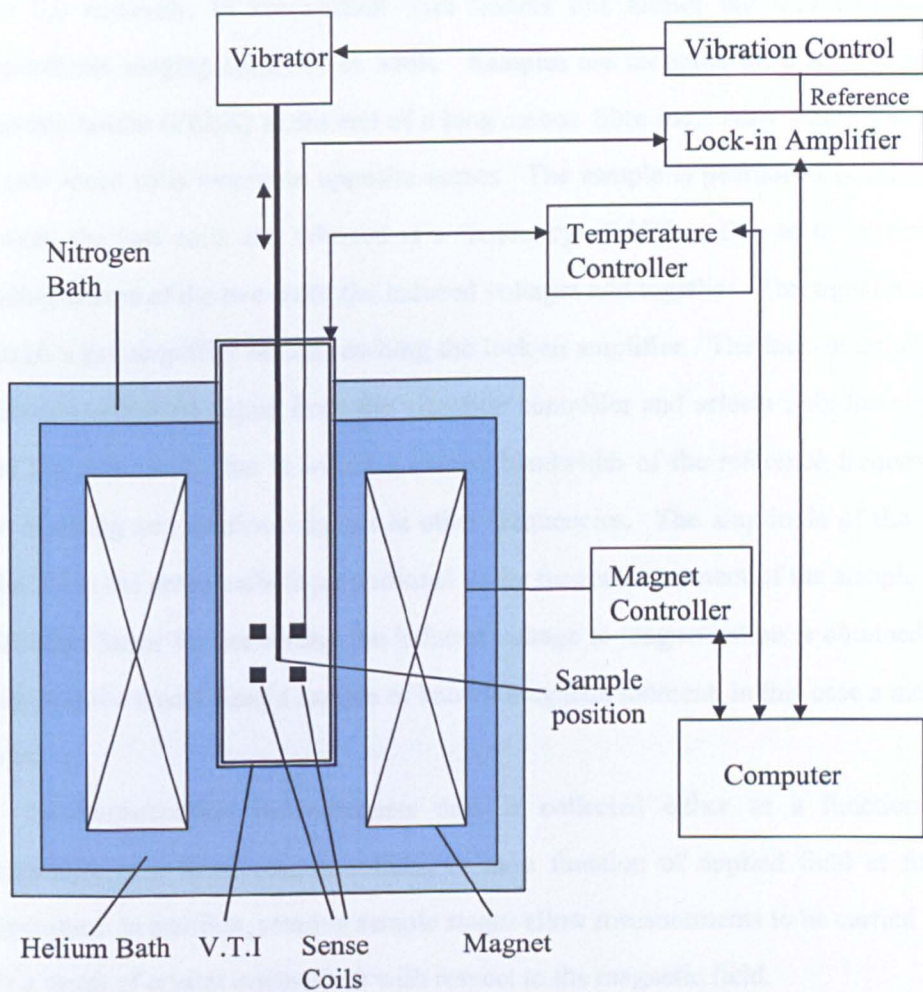
Figure 3-3. Principal components of the vibrating
sample magnetometer (VSM) (after reference 2).

helium reservoir can apply fields of up to 12T at the sample position. A variable temperature insert (VTI), reaching into the bore of the magnet, is cooled by helium from the reservoir. In conjunction with heaters this allows the VTI to provide temperatures ranging from 1.4 to 300K. Samples are mounted on a suitable non-magnetic holder (PEEK) at the end of a long carbon fibre rod. Also within the VTI are two sense coils wound in opposite senses. The sample is positioned equidistant between the two coils and vibrated at a frequency of 55Hz. Due to the different winding senses of the two coils, the induced voltages add together. The signal passes through a pre-amplifier before reaching the lock-in amplifier. The lock-in amplifier receives a reference signal from the vibration controller and selects only the signal from the sense coils that is within a narrow bandwidth of the reference frequency, thus avoiding any spurious signals at other frequencies. The amplitude of the a.c. signal from the sense coils is proportional to the magnetic moment of the sample. A calibration factor for converting the induced voltage to magnetisation is obtained by measuring the signal from a sample of known magnetic moment, in this case a nickel sphere.

In magnetisation measurements data is collected either as a function of temperature in a fixed magnetic field, or as a function of applied field at fixed temperature. In addition, rotating sample stages allow measurements to be carried out over a range of crystal orientations with respect to the magnetic field.

References

[1]   B.K. Cho *et al.*, Phys. Rev. B **52** No 5, p3681 (1995)

[2]   Oxford Instruments VSM System Manual

[3]   C.D. Dewhurst, PhD Thesis (1997)

Chapter 4

Neutron Scattering

4.1 Introduction

During the last several decades x-ray and neutron scattering have been used extensively to investigate the properties of matter. This is possible because both neutron and x-ray beams can be produced with wavelengths of the order of an atomic spacing enabling determination of crystal structures. X-ray scattering, which depends on the density of electrons surrounding a nucleus, is inefficient for detecting the lighter elements, and cannot easily distinguish between neighbouring members of the periodic table. These limitations do not apply to neutrons, which are scattered from nuclei via the strong nuclear force. Scattering from different elements is non-systematic and varies even between isotopes of the same element. The most exciting property of the neutron, however, is that it possesses a magnetic moment that allows investigations of magnetic structures and excitations. The chargeless neutron can penetrate the bulk of the sample and provide information on the distribution and even the absolute orientation of magnetic moments; it is also used to probe the properties of vortex lattices in type-II superconductors. This magnetic moment has made neutron scattering an invaluable tool in the study of magnetism.

Neutron beams are produced at facilities throughout the world by various methods, principally spallation and nuclear reaction. In the spallation method protons strike a heavy target, for example tantalum, releasing neutrons. The beam may be produced continuously, as at the SINQ source at the Paul Scherrer Institut (PSI) in Switzerland, or can alternatively be pulsed as is the case at the ISIS facility. At the Institut Laue-Langevin (ILL) in France the neutron source is a nuclear reactor

that uses uranium fuel rods. Fast neutrons are produced by nuclear chain reaction. The neutrons may then pass through moderators, colliding with atoms of a light element such as deuterium, to produce beams with the required range of wavelengths. A cold moderator of liquid deuterium cooled to 25K can slow neutrons down sufficiently to provide the long wavelengths needed for small angle scattering. The majority of instruments use thermal neutrons produced using a moderator near to room temperature – these neutrons have wavelengths that are similar to typical inter-atomic distances and can be used for crystal or magnetic structure determination. For a detailed theoretical background to the subject, the reader is referred to texts such as those by Squires[1], Lovesey[2], and Bacon[3].

4.2 Nuclear Scattering

4.2.1 Neutron Scattering Cross-Sections

When a neutron approaches a nucleus, it may be either absorbed or scattered, unless it passes that nucleus without any interaction. In neutron scattering experiments the scattered neutrons are measured. The total scattering cross-section σ is defined as[1]

$$\sigma = \frac{\text{number of scattered neutrons per second}}{\Phi} \qquad (4.1)$$

where Φ is the incident neutron flux. Since Φ has dimensions of $(m^{-2}s^{-1})$, the cross-section has dimensions of area, (m^2). This includes all scattered neutrons regardless of energy or direction. In general we are interested in how many of those neutrons are scattered into a particular direction, say a solid angle $\Delta\Omega$ in a direction θ,ϕ as shown in figure 4-1. In this case the measured quantity is the differential cross-section:

$$\frac{d\sigma}{d\Omega} = \frac{\text{neutrons scattered into } \Delta\Omega \text{ per second}}{\Phi \, \Delta\Omega} \qquad (4.2)$$
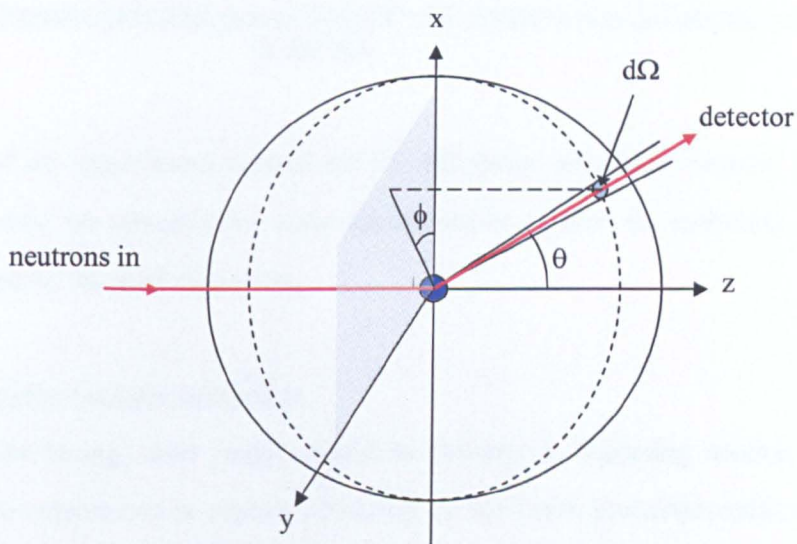
Figure 4-1: Scattering of neutrons from a nucleus into the
solid angle $\Delta\Omega$ in the direction θ,ϕ.

If energy analysis is also required, for example when investigating inelastic scattering, we may wish to consider only those neutrons scattered into $\Delta\Omega$ with final energy between E' and E'+ΔE'; then the partial differential cross-section is measured:

$$\frac{d^2\sigma}{dEd\Omega} = \frac{\text{neutrons with final energy E'<E<E'+}\Delta\text{E' scattered into }\Delta\Omega\text{ per second}}{\Phi\ \Delta E\ \Delta\Omega} \quad (4.3)$$

As all of the experiments carried out for this thesis are elastic neutron scattering experiments, we consider the static approximation, where the scattering centre is unaffected by the scattering event.

4.2.2 Neutron-Nucleus Interaction

The strong, short range interaction between an incoming neutron and the nucleus is represented in neutron scattering by the Fermi pseudopotential, which is not a true potential but which has been contrived to give the right results within the Born approximation framework. The Fermi pseudopotential at a distance r from the nucleus is defined as[2]

$$\hat{V}(r) = \frac{2\pi\hbar^2}{m}\, b\, \delta(R-r) \quad (4.4)$$

where R is the position vector of the nucleus and m the mass of the neutron. The quantity b is called the scattering length and provides an indication of the scattering power of a nucleus. b can be complex; the imaginary component corresponds to absorption of the neutron by the nucleus and is usually small. The real part is most often positive, corresponding to a repulsive potential, but for some elements it can be negative. Different isotopes of the same element have different nuclear scattering lengths, and if a nucleus possesses spin, it will have two scattering lengths depending on whether the neutron spin adds to or subtracts from the nuclear spin. For simplicity we assume a spinless nucleus and, as most nuclei have a small imaginary component, it is reasonable to consider the scattering length as a real quantity.

4.2.3 Scattering from a Single Bound Nucleus

If we take the origin at the position of the nucleus and the wave vector k of the incoming neutrons to be in the z-direction then the incoming plane wave has a wave-function of the form[3]

$$\Psi_{inc} = \exp(ik.\hat{z}) \tag{4.5}$$

With typical neutron wavelengths the nucleus is effectively a point scatterer leading to only s-wave scattering that is spherically symmetric. The wave-function of the scattered wave at a distance r from the nucleus is

$$\Psi_{sc} = -\frac{b}{r}\exp(ikr) \tag{4.6}$$

The magnitude of k is unchanged if the scattering is elastic.

If the velocity of the neutrons is v then the incident flux is given by

$$\Phi = v\,|\Psi_{inc}|^2 = v \tag{4.7}$$

and the number of scattered neutrons per second passing through an area dS is

$$v\,dS\,|\Psi_{sc}|^2 = v\,b^2\,d\Omega \tag{4.8}$$

From the definition of the differential scattering cross-section (4.2) it follows that

$$\frac{d\sigma}{d\Omega} = \frac{v\,b^2\,d\Omega}{v\,d\Omega} = b^2 \tag{4.9}$$

The integral gives a factor of 4π to give the relation between the total scattering cross-section and the scattering length b:

$$\sigma_{total} = 4\,\pi\,b^2 \tag{4.10}$$

4.2.4 Nuclear Scattering from Crystals

When considering the scattering arising from a regular array of atoms such as is formed in a crystalline solid, the scattering cross-section can generally be divided into two parts: the coherent (σ_{coh}) and incoherent (σ_{incoh}) cross-sections[3] i.e.

$$\sigma_{total} = \sigma_{coh} + \sigma_{incoh} \tag{4.11}$$

The coherent component is the result of in-phase scattering from all nuclei and is the basis of elastic diffraction experiments. The coherent cross section is defined as[1]

$$\sigma_{coh} = 4 \pi \bar{b}^2 \tag{4.12}$$

where $\bar{b}$ is the average of all the scattering lengths of the nuclei. The incoherent contribution is due to the different scattering lengths of isotopes, differences in nuclear spin, or both of these, and provides an angle-independent background to any measurement. The incoherent cross-section is thus related to deviations in the scattering length from the average:

$$\sigma_{incoh} = 4 \pi \overline{(b - \bar{b})^2} \tag{4.13}$$

4.2.5 Coherent Elastic Scattering: Diffraction

If V_0 denotes the volume of the unit cell, the coherent elastic scattering cross-section per unit cell is defined as[4]

$$\left(\frac{d\sigma}{d\Omega}\right)_{coh} = \frac{(2\pi)^3}{V_0} \sum_{\tau} |F_N(Q)|^2 \delta(Q - \tau) \tag{4.14}$$

where $F_N(Q)$ is called the nuclear unit cell structure factor and is given by

$$F_N(Q) = \sum_d b_d \exp(iQ.d - W_d(Q)) \tag{4.15}$$

The positions of the atoms within the unit cell are represented by the vectors d and the expression includes a term $\exp(-W_d(Q))$, known as the Debye-Waller factor, which is a temperature dependent factor relating to the thermally induced displacement of atoms from their regular positions. This factor is negligible at low temperatures but is included here for completeness. In these equations τ is any reciprocal lattice vector and Q is the scattering vector, which is the difference between the wavevectors of the incident and scattered beams, given by

$$Q = k' - k \tag{4.16}$$

where k' and k are the wavevectors of the scattered and incident neutrons respectively.

The reciprocal lattice is a very useful concept for describing diffraction conditions. Reciprocal lattice unit cell vectors are related to the crystal unit cell vectors via:

$$\mathbf{a}^* = 2\pi \frac{\mathbf{b} \times \mathbf{c}}{\mathbf{a}.\mathbf{b} \times \mathbf{c}}; \qquad \mathbf{b}^* = 2\pi \frac{\mathbf{c} \times \mathbf{a}}{\mathbf{a}.\mathbf{b} \times \mathbf{c}}; \qquad \mathbf{c}^* = 2\pi \frac{\mathbf{a} \times \mathbf{b}}{\mathbf{a}.\mathbf{b} \times \mathbf{c}} \qquad (4.17)$$

and have units of reciprocal length (m^{-1}). Any point on the reciprocal lattice based on these vectors corresponds to a set of planes of the crystal lattice i.e. the point at (ha^*,kb^*,lc^*) corresponds to the {hkl} set of planes, where the h,k,l are the Miller indices of that set of planes. The delta function in equation (4.14) specifies that diffraction – reinforcement of any scattered beam by other scattered beams – only occurs under very particular circumstances: when the scattering vector $\mathbf{Q}$ coincides with a reciprocal lattice vector. This diffraction condition is represented in figure 4-2. The wavevectors $\mathbf{k}$ and $\mathbf{k'}$ end on a sphere of radius $k = |\mathbf{k}|$, called the Ewald sphere. Diffraction can occur wherever the Ewald sphere crosses a reciprocal lattice point. From this diagram, equation (4.16) can be re-written as

$$|\mathbf{Q}| = |\tau| = 2\,k \sin\theta \qquad (4.18)$$

The magnitude of τ is $2\pi/d_{hkl}$, where d_{hkl} is the spacing between the lattice planes, and as the magnitude of the wavevector k is by definition equal to $2\pi/\lambda$, where λ is the neutron wavelength being used, equation (4.18) is simply

$$\lambda = 2\,d_{hkl} \sin\theta \qquad (4.19)$$

which is the well known Bragg equation – i.e. coherent elastic scattering is Bragg scattering.
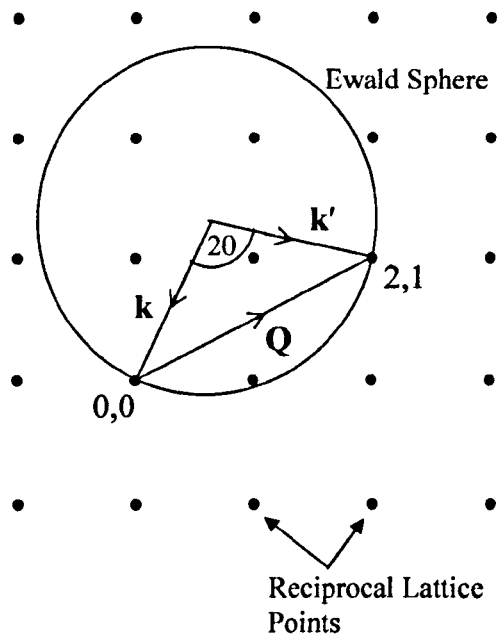
Figure 4-2: The diffraction condition in reciprocal space (in two dimensions). If the sample (and hence the reciprocal lattice) are rotated so that **Q** coincides with a reciprocal lattice vector, diffraction occurs.

4.3 Magnetic Scattering

4.3.1 Magnetic Neutron Diffraction

Elements such as transition metals and rare earth elements have incomplete electron shells ($3d$ and $4f$ respectively) and the unpaired electrons in these shells give the atom an overall magnetic moment. As the neutron also possesses a magnetic moment there is a magnetic dipole interaction between the two and so both nuclear and magnetic scattering can occur. Magnetic scattering differs from nuclear neutron scattering because it is anisotropic. This is due to the greater spatial extent of the magnetisation: for magnetic scattering the target is no longer a point target, and as a result the scattered amplitude has a dependence on $\sin\theta/\lambda$, where θ is the Bragg angle and λ the neutron wavelength (figure 4.3). This angular dependence is known as the magnetic form factor, which is different for each magnetic element and plays a similar role to the electronic form factor in x-ray scattering. Thus the intensity of magnetic scattering decreases rapidly with $|Q|$ - an important consideration in magnetic neutron scattering experiments. The form factor falls off less rapidly with $\sin\theta/\lambda$ for the magnetic rare earth ions, which have highly localised moments, compared to transition elements.

In materials that order magnetically below some transition temperature the moments form periodic structures and so neutrons can be coherently scattered from the magnetic structure as well as the underlying crystal structure. The positions of magnetic Bragg peaks are determined by the configuration of the magnetic moments and the intensities by their magnitude and orientation.

The coherent elastic magnetic scattering cross section per unit cell can be written as[4]

$$\left(\frac{d\sigma}{d\Omega}\right)_M = D\frac{(2\pi)^3}{V_0}\sum_\tau |F_M(Q)|^2 \,\delta(Q-\tau) \qquad (4.20)$$
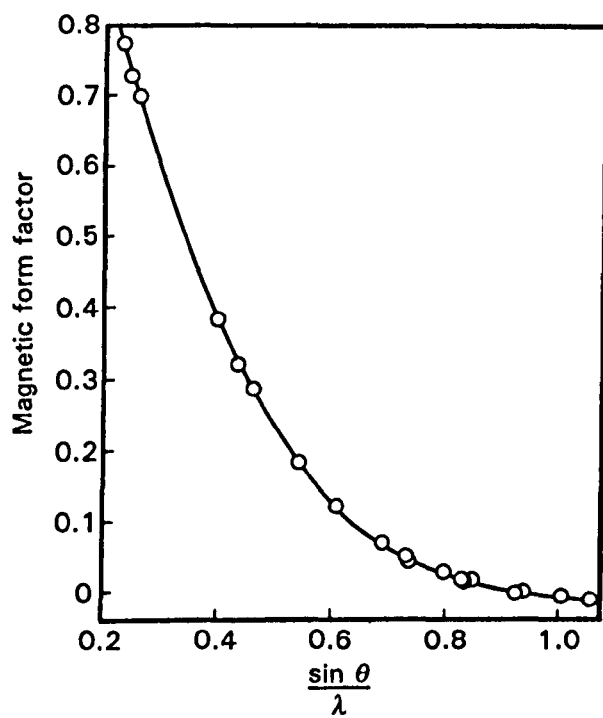
Figure 4-3: Illustration of decrease in the magnetic form factor with scattering vector **Q**, in this case for hexagonal cobalt. Reproduced from reference 11.

where the constant $D = \gamma^2 R_e^2 = 2.9 \times 10^{-29} \, m^2$, in which R_e is the classical electron radius and $\gamma = 1.91$ is the gyromagnetic ratio. $F_M(Q)$ is the magnetic unit cell structure factor given by

$$F_M(Q) = \hat{Q} \times \left\{ \sum_d \mu_d F_d(Q) \exp(iQ.d) \right\} \times \hat{Q} \qquad (4.21)$$

neglecting the Debye-Waller factor. μ_d is the moment of the dth atom, and F_d its associated magnetic form factor; $\hat{Q}$ is a unit vector. The most important change from the expression for the nuclear unit cell structure factor (4.15) is the orientational dependence introduced by the vector triple product in the magnetic structure factor. This is because neutrons are only scattered by components of the magnetisation that are perpendicular to the scattering vector Q.

4.3.2 Neutron Scattering from Different Magnetic Structures

The simplest example to consider is a single domain ferromagnet where all moments are aligned in the same direction. The magnetic unit cell is the same as the chemical unit cell, so that below the ordering temperature T_C the extra magnetic scattering will be observed superimposed on the nuclear Bragg peaks. In the case of a simple antiferromagnet, where neighbouring moments are aligned antiparallel to each other, the magnetic unit cell is at least twice as large as the chemical unit cell. A hypothetical example is shown in figure 4-4. As a result of the different unit cell sizes, no extra scattering is seen at the nuclear peaks, but instead new peaks emerge below T_N at (for this example) halfway positions corresponding to the doubled dimensions of the magnetic unit cell. For more complex magnetic structures, such as the incommensurate spin density waves frequently observed in the borocarbides, the positions of magnetic Bragg peaks vary widely depending on the precise nature of the ordering.
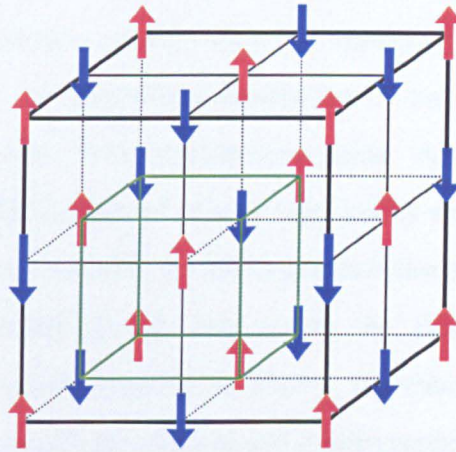
Figure 4-4: One magnetic unit cell for a hypothetical simple antiferromagnet showing doubled unit cell dimensions compared to the green chemical unit cell.

4.4 Experimental Neutron Diffraction

4.4.1 Experimental Arrangements

Magnetic structures are usually investigated using double or triple axis diffractometers. A schematic representation of a typical two-axis diffractometer is shown in figure 4-5a. A Maxwellian distribution of wavelengths arrives at the instrument from the source via the neutron beam guide. A monochromatic beam is usually required and this is obtained using a high quality single crystal oriented so that the Bragg condition is satisfied for the desired wavelength. For the same angle 2θ, however, wavelengths of λ/n also satisfy the Bragg condition causing contamination; this is usually removed by filters. The choice of monochromating crystal depends on the wavelength required and is often copper or pyrolytic graphite. The reflected neutrons pass through collimators on their way to the sample position. An aperture may be mounted at the end of the collimation section to produce different sizes and shapes of beam. The sample can be mounted in a conventional cryostat or cryomagnet (if a magnetic field is required) in which case it can only be rotated around a vertical axis (generally denoted ω) perpendicular to the incoming beam. An alternative option is a four-circle cryostat, which allows the sample to be positioned in almost any orientation with very few limitations, but it is not possible to support heavy equipment such as magnets. Sections of the sample environment equipment that neutrons must pass through on the way into or out of the cryostat are made of aluminium (if possible), which has negligible neutron absorption and incoherent scattering cross-section. After being diffracted by the sample, neutrons enter the detector. On triple axis spectrometers neutrons pass through an analyser (the third axis) before reaching the detector. Like the monochromator, the analyser is a single crystal and allows selection of a particular wavelength for detection. For basic structure determinations this is not necessary and a two-axis instrument is sufficient. The angle between the incoming beam and the detector corresponds to 2θ

A

Cryostat

Sample

k′

k

ω

ω

2θ

Collimators

Detector

Monochromating
crystal

Neutrons
from source

ω,2θ

B

Detector

k

k′

v

Cryostat +
Sample
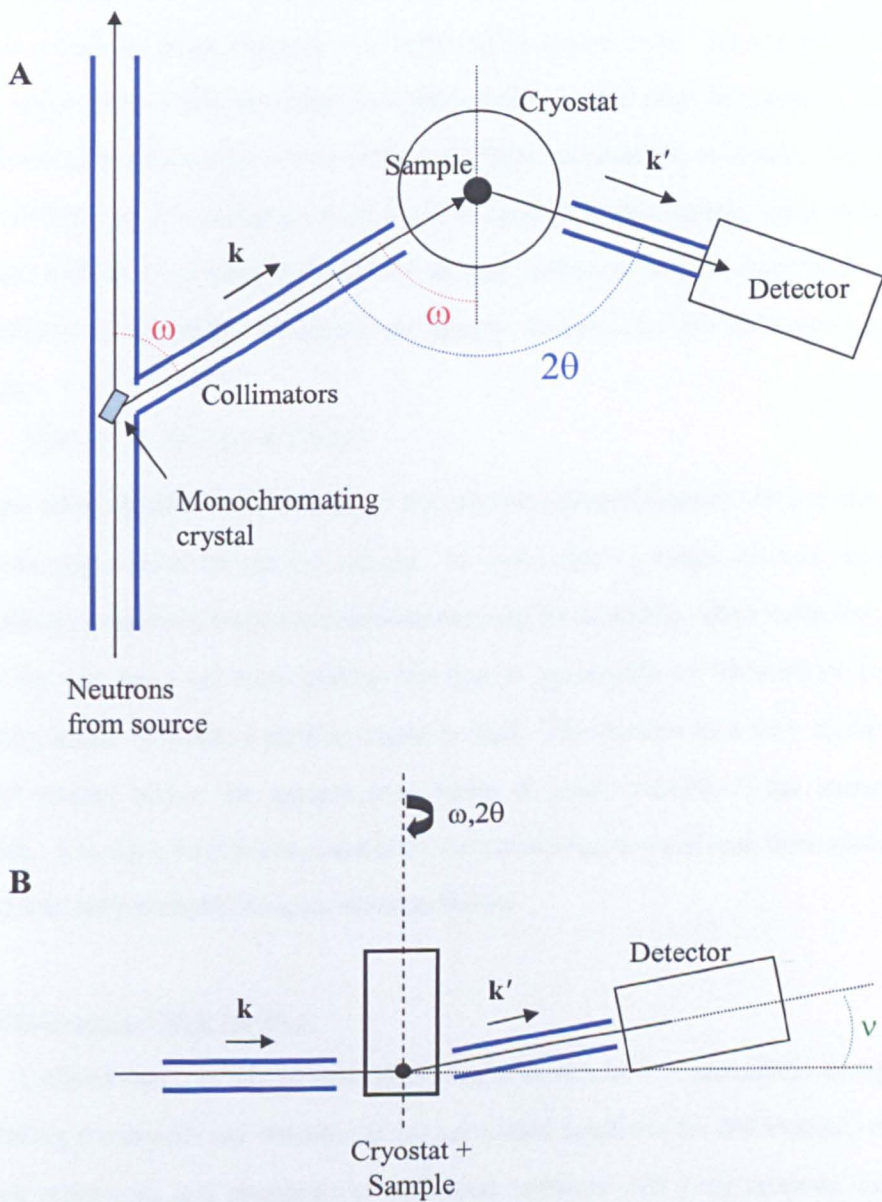
Figure 4-5: Schematic representation of a two-axis diffractometer such as D23
at ILL, showing a) bird's eye and b) side view, including elevation of the
detector through an angle v.

and it is coaxial with ω. In some cases the detector may be lifted out of the plane through a limited angle denoted ν as indicated in figure 4.5b. This is particularly useful where four-circle cryostats are unavailable; in this case the sample usually only needs to be remounted in two or three different orientations to obtain a complete set of reflections. If a magnetic field is to be applied to the sample, the number of available reflections is more limited if the sample properties depend on its orientation with respect to the field. Neutrons are usually detected in ^{3}He detectors via the reaction[5]

$$^3_2\text{He} + \text{n} \rightarrow \,^3_1\text{H} + \text{p} + 0.77\text{MeV}$$
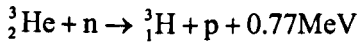
in a gas filled chamber under voltage; the emitted charged particle ionises the gas, thus inducing a pulse of electric current. In some cases a single detector is used; alternatively a position sensitive multidetector may be available. Data collection can be carried out for a set time interval but this is vulnerable to fluctuations in the incoming beam. Instead, a monitor count is used. The monitor is a very inefficient detector placed before the sample that counts a small fraction of the incoming neutrons. The use of a monitor count allows direct comparison of data from different instruments with different incident neutron fluxes.

4.4.2 Obtaining a Value for $|F_{hkl}|$

Unfortunately, in any neutron scattering experiment it is unrealistic to expect that placing the sample and detector in the calculated positions for observation of the required reflections and counting the diffracted neutrons will yield accurate values for the squares of the structure factors, $|F_{hkl}|^2$. In single crystal diffraction experiments the sample is usually rotated through the Bragg condition for a particular reflection and the number of neutrons is measured at points within the scan. Instead of finding intensity only at one point as implied by the delta functions in equations (4.14) and (4.20) there is diffracted intensity spread out over a range of angles about the calculated position. Even for a perfect crystal this occurs because -

a) a small spread of wavelengths around the desired value is obtained from even the best monochromating crystal and b) the collimation is not perfect. The net result is a narrow range of values of incident wavevector at the sample position. This means that there is not a unique scattering vector for a particular reflection and correspondingly the Bragg condition is satisfied over a small range of angles. In a low quality crystal this situation is made worse. A statistical function such as a Gaussian distribution can then be fitted to the resulting data set. Thus the measured quantity becomes the integrated intensity, I_{hkl}. The relation between I_{hkl} and $|F_{hkl}|$ can be written as[6]

$$I_{hkl} = \frac{N_{hkl}\omega}{\Phi} = \frac{\lambda^3 V}{V_0^2}|F_{hkl}|^2 \tag{4.22}$$

where N is the number of diffracted neutrons, V the sample volume, and ω the rotation angular velocity (so that its reciprocal is the measuring time at each point). Several corrections must also be made, relating both to the geometry used and the sample. These are:

1. Temperature: the Debye-Waller factor, relating to thermal effects, was mentioned previously; it is negligible at very low temperatures.

2. Absorption: in all of the analyses above, it has been assumed that the incident beam is not significantly absorbed by the sample but in some cases a correction relating to attenuation of the beam must be made. The [11]B isotope is used in RNi_2B_2C samples to avoid this problem although for the more absorbing rare-earth elements it is still necessary to include this correction.

3. Extinction: there are two types. In a very perfect crystal, with large domains, the incident beam may be appreciably reduced by diffraction within each domain so that distant areas receive significantly lower incident intensity; this is primary extinction. If the domains are small, and slightly misaligned, diffracted beams may be rescattered by other blocks; this is secondary extinction. Extinction is very difficult to calculate accurately since a mixture of both types is usually

present. It can be reduced by using a smaller crystal, at the expense of loss of intensity, or a shorter wavelength.

4. Lorentz factor: different points in reciprocal space pass through the Ewald sphere with different velocities so that for an angular scan of fixed rate, points with different scattering vectors get differing windows of opportunity to satisfy the Bragg condition. For the geometry shown in figure 4-6, it can be shown[6] that the Lorentz factor is given by $L^{-1} = \sin\gamma\cos\nu$; for reflections in the equatorial plane ('normal beam geometry') it is just $L^{-1} = \sin(2\theta)$.

4.5 Neutron Diffraction from the Vortex Lattice in Superconductors

4.5.1 Introduction

In the mixed state of a type-II superconductor vortices form a periodic array – the magnetic flux line or vortex lattice (VL) (as described in chapter 2). When neutrons enter the sample diffraction from this lattice can occur as it does from any other periodic magnetic or nuclear structure. The experimental set-up required in order to observe this diffraction is completely different from a standard crystal or magnetic structure determination. Firstly, the distance between planes of flux lines is much larger than crystal lattice spacings. The distance between these planes for the square lattice is given by

$$d = \sqrt{\frac{\Phi_0}{B}} \qquad (4.23)$$

where Φ_0 is the flux quantum and B is the magnetic field in Tesla. For the smaller, more usual triangular lattice

$$d = \sqrt{\frac{\sqrt{3}}{2}\frac{\Phi_0}{B}} \qquad (4.24)$$

This means that for an applied field of perhaps 0.5T, the d-spacing of the square lattice is 640Å, much larger than interatomic spacings. A typical wavelength used is 14Å. Longer wavelengths of up to 40Å are available but at much reduced neutron
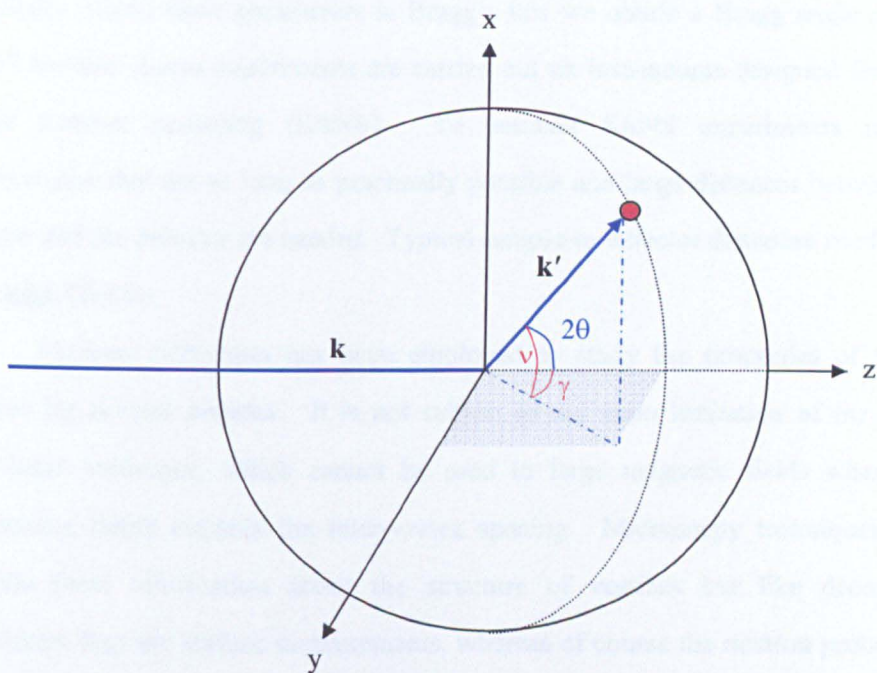
Figure 4-6: Scattering geometry used to calculate Lorentz factors in magnetic and crystal structure determinations (after ref. 6).

flux; also the longer the wavelength used, the more susceptible to gravity the beam becomes. Using these parameters in Bragg's law we obtain a Bragg angle of only $0.63°$; for this reason experiments are carried out on instruments designed for small angle neutron scattering (SANS). To conduct SANS experiments neutron wavelengths that are as long as practically possible and large distances between the sample and the detector are needed. Typical sample-to-detector distances used are in the range 10-18m.

Neutron diffraction has been employed to study the properties of vortex lattices for several decades. It is not subject to the main limitation of the Bitter decoration technique, which cannot be used in large magnetic fields where the penetration depth exceeds the inter-vortex spacing. Microscopy techniques may provide local information about the structure of vortices but like decoration techniques they are surface measurements, whereas of course the neutron probes the bulk of the sample.

4.5.2 Experimental Set-up

The typical SANS instrument set-up is shown in figure 4-7. The required neutron wavelength is provided by a rotating *velocity selector*; the speed of rotation is chosen to allow the required wavelength to pass. For intensity reasons a small range of wavelengths is actually transmitted through the selector, with a typical wavelength spread ($\Delta\lambda/\lambda$) of 10%. Neutrons then pass through sections of collimators that can be removed individually to give the required collimation length. Increasing the collimation length leads to improved resolution but diminished neutron flux at the sample. An aperture may be added to the end of the guide sections. After passing through the sample environment the neutrons enter the detector chamber which is under vacuum to reduce scattering from air. The area multidetector can be moved along the length of the chamber and may be tilted if required. A beam-stop is usually positioned so as to protect the centre of the detector from the unscattered beam

~40m

ω

ϕ

2θ

Velocity
selector

Collimation sections

Sample +
environment

Area multidetector in
evacuated chamber
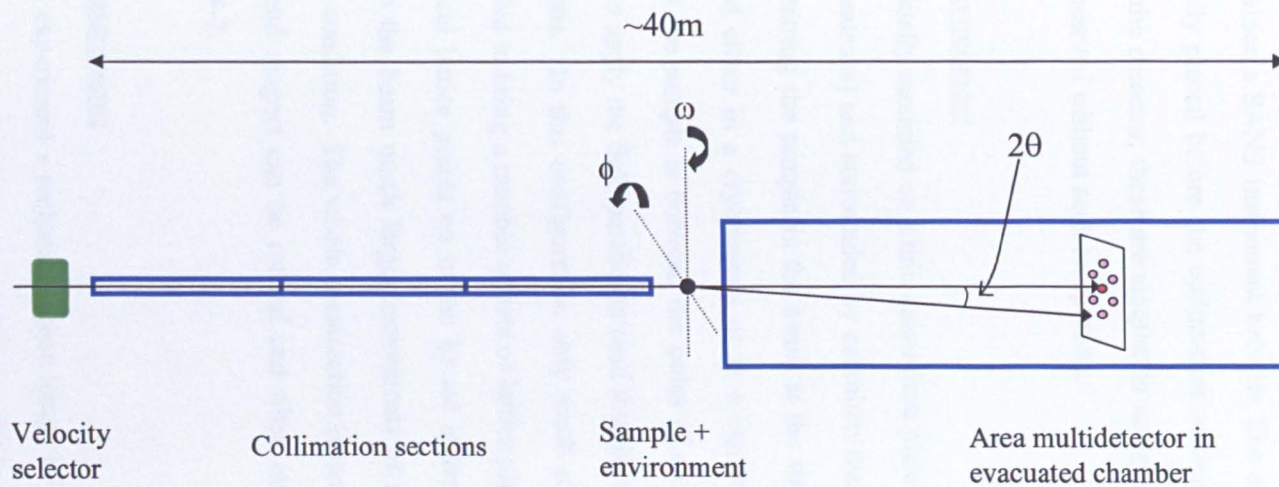
Figure 4-7: Schematic representation of a small angle scattering
instrument such as D22, ILL.

unless attenuators have been placed in the beam upstream of the sample. The D22 (ILL) and SINQ_SANS (PSI) detectors are 128x128 pixels in total covering almost a square metre. Since a SANS instrument behaves like a pinhole camera, a circular aperture is usually placed before the collimation sections which results in circular Bragg spots on the detector; these are simpler to analyse than the rectangular spots that would be observed without such an aperture.

4.5.3 Sample Environment

The crystal is usually mounted on a thin aluminium plate (i.e. a holder that is almost transparent to neutrons) and surrounded by cadmium that absorbs neutrons. This is helpful when centring the sample in the beam at the start of the experiment. The sample is placed either in a cryomagnet or in a standard cryostat which is itself mounted so that the sample is between the poles of an electromagnet. The usual arrangement is to apply the field parallel to (and therefore align the flux-lines to) the incoming neutrons. In this configuration only small rotations of the sample and magnet are needed to bring a number of sets of lattice planes to the Bragg condition (i.e. the reciprocal lattice points on to the Ewald sphere). If the field is applied perpendicular to the beam much larger movements of the sample are required to reach the Bragg condition. The whole construction is mounted on a goniometer and so the sample and magnet can be rotated and tilted around the different axes as indicated in fig 4-7.

4.5.4 SANS Measurements

During a SANS experiment a reciprocal space image of the VL is produced on the detector. This image is related to the real space lattice by a 90° rotation and re-scaling of the axes. Therefore if the experiment has been set up correctly it is a relatively simple matter to observe the lattice morphology (square or triangular) and orientation of the VL relative to the crystal axes. The sample is 'rocked' through the

Bragg condition for a particular set of lattice planes by rotating usually in ω, and in ϕ if a complete picture of the VL is required. Thus the shape of the VL may be easily examined as a function of temperature or applied field. However, more detailed information can be learned by examining the intensity of reflections.

As usual the measured quantity is the integrated intensity which for a VL (normalised to incident neutron flux) is given by[7]

$$I_{hk} = \left(\frac{\mu}{4}\right)^2 \frac{\lambda_n^2 V}{\Phi_0^2} \frac{2\pi}{Q_{hk}} |F_{hk}|^2 \qquad (4.25)$$

where μ is the neutron magnetic moment in nuclear magnetons, λ_n is the neutron wavelength and the F_{hk} are the form factors for each h,k reflection; the other symbols have their usual meanings. The internal magnetic field distribution, being periodic, can be written as a Fourier sum[8]

$$h(\mathbf{r}) = \sum_{hk} F_{hk} \exp(i\mathbf{Q}.\mathbf{r}) \qquad (4.26)$$

In the London limit, i.e. far from H_{C2} where the vortex cores are unimportant, the form factors are given by

$$F_{hk} = \frac{B}{1 + Q_{hk}^2 \lambda^2} \qquad (4.27)$$

In this case λ is the penetration depth. For typical fields and the penetration depths under consideration, the form factors can be approximated by $B/Q^2\lambda^2$. As $I_{hk} \propto |F_{hk}|^2/Q_{hk}$, this means that $I_{hk} \propto \lambda^{-4}$, making it difficult to observe the scattering from superconductors with long penetration depths such as the high-T_C cuprates; also $I_{hk} \propto Q^{-5}$, so that higher order diffraction is very weak indeed. It is often necessary, particularly when investigating VLs in large-λ materials, to subtract a background measurement taken at $T > T_C$ or $H > H_{C2}$ to observe the VL signal. As penetration depths increase as T_C is approached the diffracted intensity drops quickly and much longer counting times are needed to achieve statistically acceptable data.

At fields where the lattice spacing is sufficiently reduced that the effect of the vortex cores needs to be considered the simple London description above is

inadequate. In these conditions the form factors can be approximated for the square lattice[9] by

$$F_{hk} = \frac{\Phi_0}{(2\pi)^2 \lambda^2} \exp\left(-\frac{2\pi^2 \xi^2 B}{\Phi_0}\right)$$
(4.28)

i.e. both the penetration depth and coherence length can be extracted from measurements of the field dependence of the intensity of the VL peaks, though only under the assumption that this expression for the form factors is correct.

Many of the corrections used in standard diffraction also apply to SANS experiments. Debye-Waller and absorption factors must be considered in appropriate circumstances. The Lorentz correction for the small angle case is given[9] by $L^{-1} = \cos(\eta_Q)$, where the sample is rotated through ω at fixed ϕ, using the angles defined in figure 4-8.

In common with normal magnetic or nuclear diffraction techniques, the resolution of the SANS diffractometer is limited by the wavelength spread and collimation before the sample and, in this case, by the size of the pixels of the multidetector. The beam divergence means that spots on the detector always have a finite size. These instrumental factors also result in a finite 'rocking curve' width in the same way that they do for standard diffraction, even for an ideal VL. The imperfections of the VL, such as mosaic spread and non-straightness of the flux-lines, also contribute to the rocking curve width of the peaks, so that if the instrumental parameters are very well understood it is possible to extract information on the degree of perfection of the VL[10].

Figure 4-8: Scattering geometry used in calculation of Lorentz
factors in SANS experiments (after ref. 9).

References

[1] G.L. Squires, *Introduction to the Theory of Thermal Neutron Scattering* (CUP 1978)

[2] S.W. Lovesey, *Theory of Neutron Scattering from Condensed Matter* Volume 1 (OUP 1984)

[3] G.E. Bacon, *Neutron Diffraction* (OUP 1975)

[4] P.J. Brown in 'Treatise on Materials Science Technology', Volume 15 - *Neutron Scattering* (Academic Press 1979)

[5] R. Scherm and B. Fak in 'Neutron and Synchrotron Radiation for Condensed Matter Studies' Volume 1 - *Theory, Instruments and Methods* (Springer-Verlag 1993)

[6] G.J. McIntyre in 'Neutron and Synchrotron Radiation for Condensed Matter Studies' Volume 1 - *Theory, Instruments and Methods* (Springer-Verlag 1993)

[7] D.K. Christen *et al.*, Phys. Rev. B **15** No.9 p4506 (1977)

[8] M. Tinkham, *Introduction to Superconductivity* (McGraw-Hill 1975)

[9] M.R. Eskildsen, PhD Thesis (1998)

[10] R. Cubitt *et al.*, Physica C **180-1** p377 (1992)

[11] L. Dobrzynski & K. Blinowski, *Neutrons and Solid State Physics* (Ellis Horwood 1994)

Chapter 5

The Vortex Lattice in Non-Magnetic Borocarbides

5.1 Introduction

For a superconductor in the mixed state ($B_{C1} < B < B_{C2}$) the internal magnetic field variation of the vortex lattice (VL) can be described in terms of the Fourier components (form factor) (§4.5.4). SANS provides a tool by which these Fourier components may be examined, since the integrated intensity of each Bragg peak (I_{hk}) $\propto |F_{hk}|^2/Q_{hk}$, although the sign of a particular Fourier component cannot be deduced through this method. In this chapter, the variation of the ratio of the two strongest components, F_{10} and F_{11}, of the VL are investigated in the non-magnetic borocarbides Y- and $LuNi_2B_2C$ ($T_C = 15.5K$ and $16K$ respectively). These compounds are ideal for studying the superconducting properties of the borocarbides without the added complication of magnetic order.

For a conventional superconductor, in modest magnetic fields ($B \ll B_{C2}$) where the vortex cores are unimportant, the London theory (which neglects the cores) is usually employed to describe the mixed state. In this case the form factors[1] are given by

$$F_{hk} \propto \frac{1}{1 + \lambda^2 Q_{hk}^2} \tag{5.1}$$

where $Q_{hk} = |Q_{hk}|$. In larger magnetic fields (i.e. approaching B_{C2}) the effect of the vortex cores must be included and the Abrikosov solution deriving from the Ginzburg-Landau theory becomes more suitable. For the square lattice considered here the form factors[2] are given by

$$F_{hk} \propto -(-1)^{h^2+k^2+hk} \exp\left(-\frac{\pi}{2}(h^2+k^2)\right) \qquad (5.2)$$

As described in chapter 2, the superconductivity in the rare earth nickel borocarbides has to date been most successfully described in terms of the London model with corrections to include non-local terms[3]; this approach qualitatively accounts for the magnetic field-induced transitions in the symmetry of the vortex lattice observed in decoration and neutron scattering experiments[4-7]. The expression for the form factors can be extended to include the non-local corrections but relies on accurate values for parameters such as products of Fermi surface velocities of the material. The form factors for the borocarbides can be written for a vortex lattice with the field applied along the crystal c-direction, as

$$F_{hk} \propto \frac{1}{1+\lambda_{ab}^2 Q^2 + \lambda_{ab}^4 \left[C_1 Q^4 + C_2 Q_x^2 Q_y^2\right]} \qquad (5.3)$$

The constants C_1 and C_2 are determined by the Fermi averages, the superconducting energy gap $\Delta(T)$, the penetration depth, temperature and scattering due to non-magnetic impurities. The different values of $|F_{11}/F_{10}|$ given by the three models are given in table 5.1. The value given by the non-local approach is for $LuNi_2B_2C$, using current estimates of the relevant parameters[8] in equation 5.3; there the Fermi averages, calculated from the band structure, are given as $<v^2> = 5.12\times10^{12}$ and $<v_a^2> = 1.87\times10^{12}$ $(ms^{-1})^2$. No estimates for the Fermi averages are yet available for YNi_2B_2C, but the two compounds are very similar. The non-local theory clearly predicts that a much more rapid fall off of the form factor with Q will be observed experimentally (after appropriate Lorentz corrections) than expected from the standard London model. As the temperature is increased towards $T_C(B)$, the influence of non-locality decreases since the non-locality range is dependent on the electronic mean free path - which will itself decrease as the temperature is increased. As a result, the effect of the non-local corrections should vanish near T_C, where the vortex cores also become important, and the form factors in the borocarbides should tend towards the Abrikosov values.

Model	F_{11}/F_{10}
London, $\lambda = 710\text{Å}$	0.50
Abrikosov	0.21
Kogan non-local, $\lambda_{ab} = 710\text{Å}$	0.12

Table 5.1: Ratio of F_{11}/F_{10} for different models.

The crystal of YNi_2B_2C was grown by the Superconductivity and Magnetism group at Warwick University and has a mass of 24mg. The $LuNi_2B_2C$ crystal was provided by P. C. Canfield of Ames Laboratory/Iowa State University, USA, and has a mass of 1g. Initial SANS measurements on YNi_2B_2C were carried out on the SINQ-SANS instrument at PSI, followed by more detailed measurements on both compounds on D22 at ILL; only data obtained on D22 are shown here.

5.2 Experimental Results

5.2.1 YNi₂B₂C

Initally, the single crystal of YNi_2B_2C was mounted in a cryomagnet with a magnetic field of 0.5T applied along the crystal [0 0 1] direction. According to previous experiments on the vortex lattice in this material the VL symmetry should be square at all temperatures in this field[9]. Figure 5-1 shows data collected at a temperature of 2.7K. The axes have been converted to show intensity as a function of scattering vector $\mathbf{Q}$. To produce the VL, the sample was cooled from $T > T_C$ in the required field. This image consists of data-sets collected whilst varying ω and ϕ (see figure 4-7) simultaneously to bring each Bragg reflection to the diffraction condition in a circular fashion, rather than the usual method of collecting full rocking curves for the two angles independently. Background data, collected above T_C but otherwise by the same method, has been subtracted. In any case, the data shows that under these conditions the symmetry of the VL is square, as would be expected based
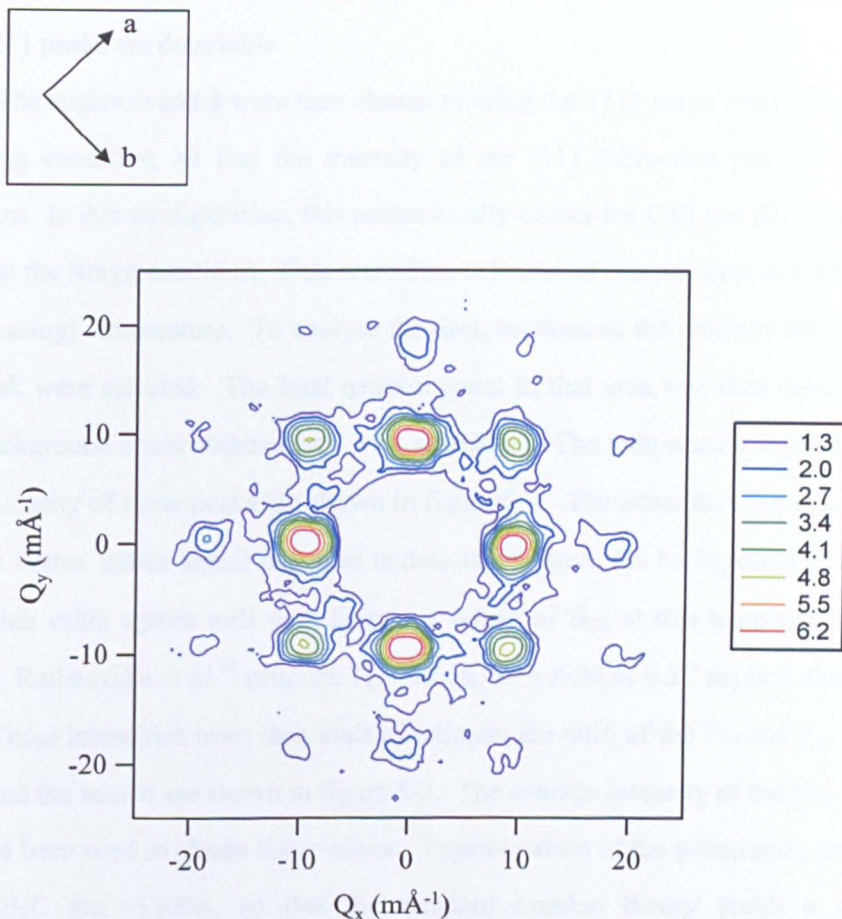
Figure 5-1: SANS diffraction pattern obtained from YNi_2B_2C in an applied magnetic field of 0.5T. The temperature is 2.7K. The intensity is on a logarithmic scale to enhance the weak higher order diffraction peaks. Background data collected at 16K have been subtracted and the centre of the detector masked. The spots are slightly square because the circular aperture in the beam guide was removed to provide maximum incident intensity.

on previous work. The {10}, {11} and {20} peaks are clearly present, and even the weak {21} peaks are detectable.

The angles ω and ϕ were then chosen to bring the {11} set of lattice planes to the Bragg condition, so that the intensity of the (11) diffraction peak is at the maximum. In this configuration, this automatically causes the (10) and (01) peaks to also be at the Bragg condition. Data were then collected at this position as a function of (increasing) temperature. To analyse the data, sections of the detector containing each peak were selected. The total neutron count in that area was then calculated, and a background count obtained at $T > T_C$ subtracted. The temperature dependences of the intensity of these peaks are shown in figure 5-2. The intensities fall smoothly until the vortex lattice signal becomes undetectable above the background at about 13K. This value agrees well with literature values of B_{C2} at this temperature; for example, Rathnayaka et al.[10] estimate $T_C \sim 13.5$K for a field of 0.5T applied along c.

These intensities were then used to estimate the ratio of the F_{10} and F_{11} form factors and the results are shown in figure 5-3. The average intensity of the two {10} peaks has been used to obtain these values. Typical values of the penetration depth[10] in YNi_2B_2C are ~1200Å, so that the standard London theory yields a (field independent) ratio for $|F_{11}/F_{10}|$ of 0.50 as it does for the Lu compound (table 5.1). Across the temperature range 2-10K the ratio of the form factors decreases gradually from 0.57(1) at 2.4K to 0.49(1) at 9.5K. This suggests that at low temperatures the field distribution falls off even less rapidly than predicted by the core-neglecting London approach, and far less rapidly than might be expected using the non-local approach. Above 10K, the ratio increases, reaching similar values of $|F_{11}/F_{10}|$ to those obtained at the lowest temperatures. As T_C is approached, where the Abrikosov approach should describe the VL, the $|F_{11}/F_{10}|$ ratio should tend towards 0.21 as $T \rightarrow T_C$. This is not observed here in YNi_2B_2C, despite the larger error bars at high temperatures, which reflect the very low intensities of the peaks approaching T_C.
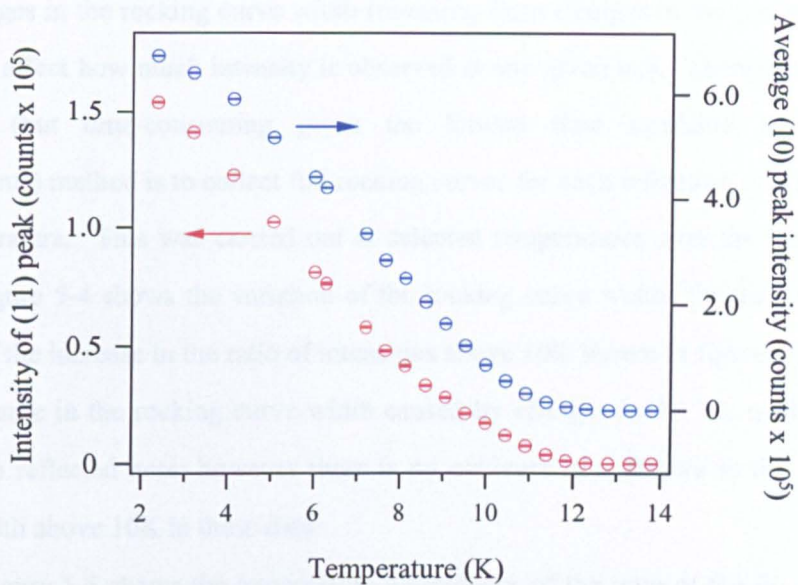
Figure 5-2: Variation of (10) and (11) spot intensity with temperature in YNi$_2$B$_2$C at 0.5T, using the box-sum method described in the text with a background collected at 16K subtracted..
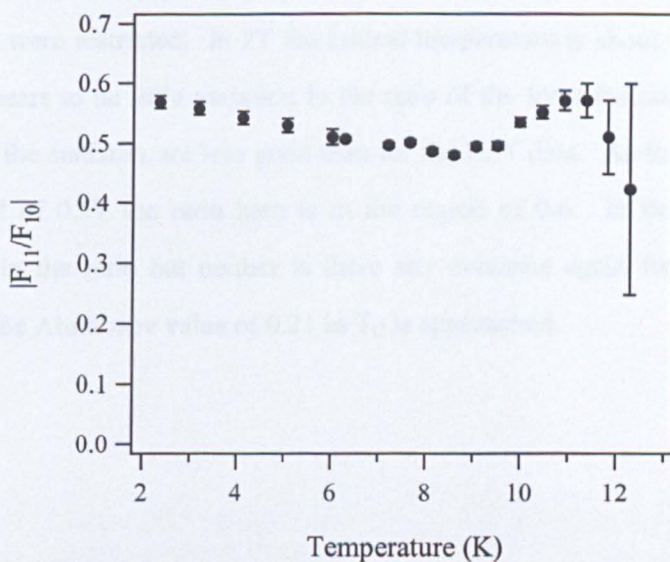
Figure 5-3: Variation of $|F_{11}/F_{10}|$ with temperature based on the intensities shown in figure 5-2 for YNi$_2$B$_2$C at 0.5T.

This approach to estimating the ratio of the form factors is not ideal, since any changes in the rocking curve width (resulting from changes in the quality of the VL) will affect how much intensity is observed at any given ω, ϕ. Therefore a more rigorous (but time-consuming given the limited time available for SANS experiments) method is to collect full rocking curves for each reflection as a function of temperature. This was carried out at selected temperatures over the range 2.7-12K. Figure 5-4 shows the variation of the rocking curve widths for the two {10} peaks. If the increase in the ratio of intensities above 10K shown in figure 5-3 is due to a decrease in the rocking curve width caused by changes in the VL quality, this should be reflected here; however there is no evidence of a feature in the rocking curve width above 10K in these data.

Figure 5-5 shows the temperature dependence of the ratio of the F_{11} and F_{10} form factors obtained using the same method as above but in a much stronger applied magnetic field of 2T. This data was obtained using the same method as for 0.5T above. Unfortunately, at 2T the stray field from the magnet caused unwanted problems on the neighbouring instrument at ILL, and as a result counting times at this field were restricted. In 2T the critical temperature is about 10K. In this field, there appears to be little variation in the ratio of the form factors with temperature, although the statistics are less good than for the 0.5T data. As for low temperatures in a field of 0.5T the ratio here is in the region of 0.6. In this case there is no increase in the ratio but neither is there any evidence again for the ratio tending towards the Abrikosov value of 0.21 as T_C is approached.
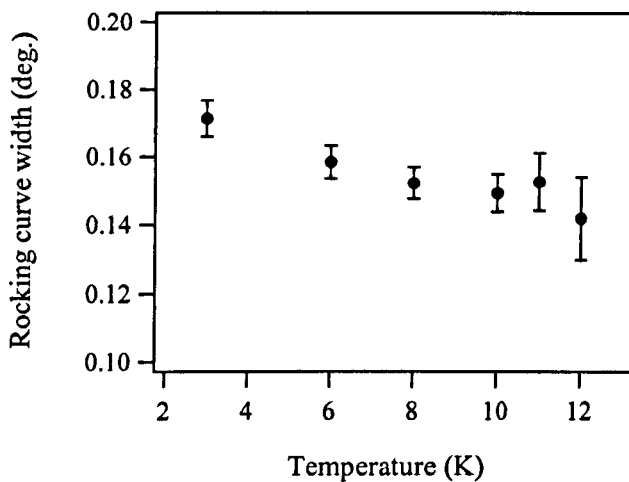
Figure 5-4: Variation of average rocking curve width of the (10) diffraction peaks with temperature at 0.5T in YNi_2B_2C. Rocking curves are collected by measuring the intensity of the peak as a function of ω or ϕ.
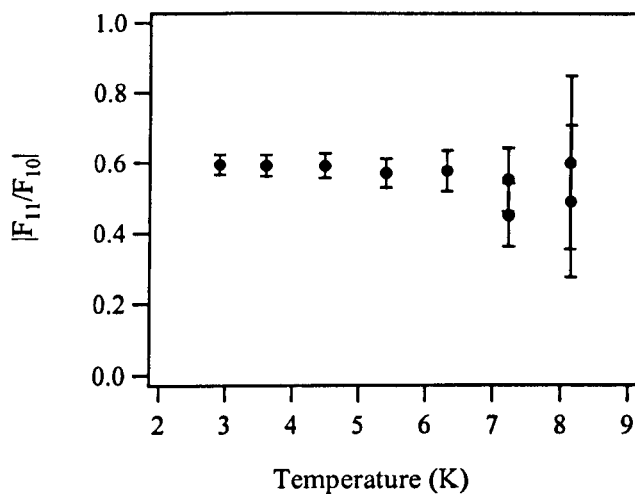
Figure 5-5: Variation of $|F_{11}/F_{10}|$ with temperature in YNi_2B_2C in an applied field of 2T.

5.2.2 LuNi$_2$B$_2$C

The LuNi$_2$B$_2$C crystal was mounted within the cryomagnet, again with B // [0 0 1]. Both ω- and ϕ 'rocks' were carried out at 2.7K and the resulting diffraction pattern (a composite of all datasets collected) is shown in figure 5-6. Again, background data collected at T > T$_C$ have been subtracted. The VL symmetry is clearly square, as expected from previous work on this material[6]. Several higher orders, up to the {21} peaks, are clearly observable using this much larger crystal.

The temperature dependences of a (11) and two (10) peaks were measured, again using the method described above. The ratio |F$_{11}$/F$_{10}$| was calculated and the results are shown in figure 5-7. The small error bars reflect the much improved statistics obtained from having a greater sample volume. At 2.7K, a ratio of 0.60(1) is obtained, which again is larger than the value of 0.50 expected from the London model and much larger than the value of 0.12 that the non-local approach suggests. As the temperature is increased the ratio falls smoothly with a similar gradient to that observed in the Y- compound up to 10K. In this case, however, there is no increase in the ratio at higher temperatures, but rather the smooth decrease continues uninterrupted. Despite this, the ratio still does not tend to the Abrikosov value of 0.21 close to T$_C$, which is about 14K in this field. Instead, at 13K, the highest temperature at which the VL could be clearly detected, the ratio is twice the expected value.

Full rocking curves were collected at different temperatures for this sample. The variation of rocking curve widths of all the {10} peaks are shown in figure 5-8. Overall, there is a slight decrease in these widths as the temperature is increased, indicating a gradual increase in the quality of the vortex lattice as individual vortices are more able to move away from pinning sites. However, as was the case for the Y- material, there is no dramatic change.
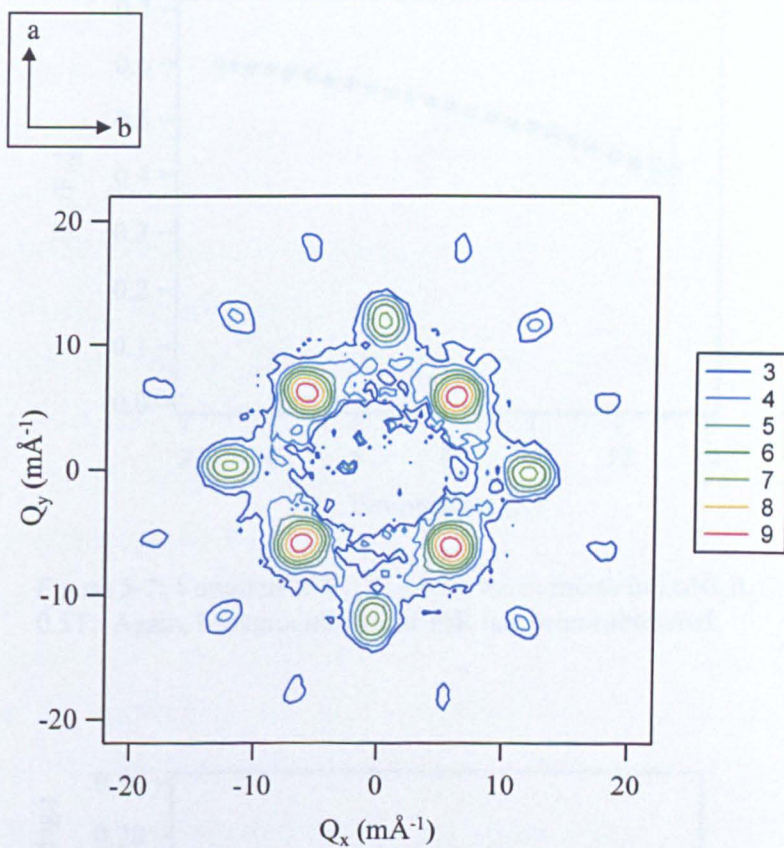
Figure 5-6: SANS image obtained from $LuNi_2B_2C$ in an applied field of 0.5T, at a temperature of 2.7K. Background data collected at 16K has been subtracted. The intensity scale is logarithmic.
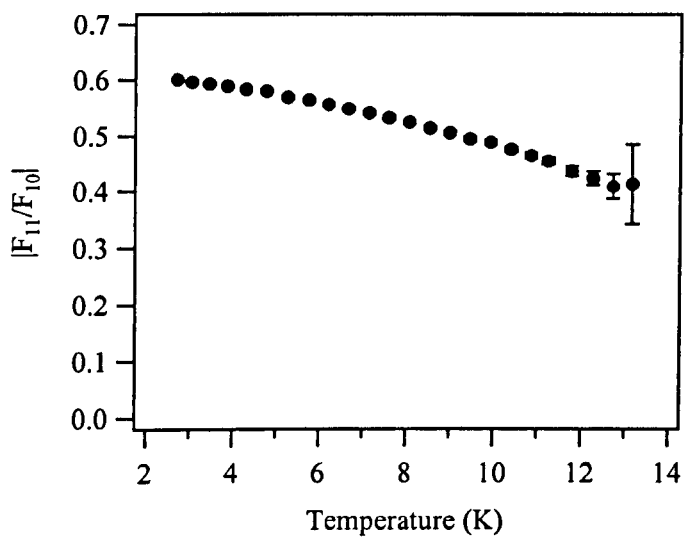
Figure 5-7: Variation of $|F_{11}/F_{10}|$ with temperature in $LuNi_2B_2C$ in 0.5T. Again, background data at 16K has been subtracted.
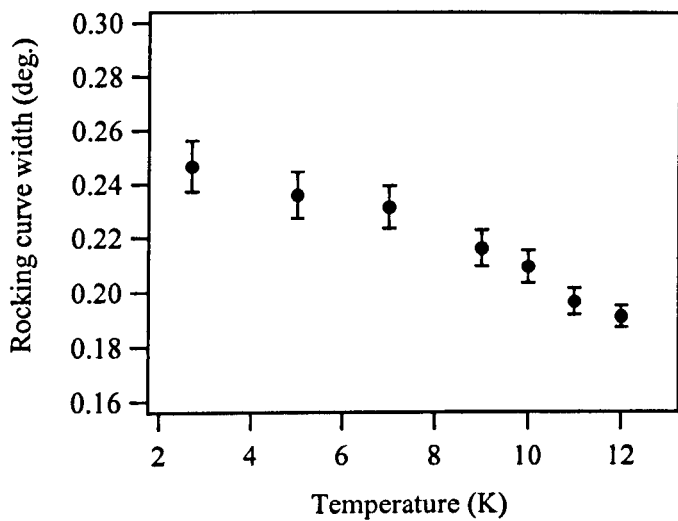
Figure 5-8: Variation of rocking curve width with temperature for $LuNi_2B_2C$ in an applied field of 0.5T.

5.3 Discussion

Small angle neutron scattering has been used to investigate the behaviour of the form factors for the vortex lattices of both Y- and $LuNi_2B_2C$, two non-magnetic members of the borocarbide family. For both materials, in an applied magnetic field of 0.5T at temperatures well below T_C, where it might be expected that the London theory with non-local corrections developed by Kogan *et al.*[8] for the form factors should be applicable, the ratio $|F_{11}/F_{10}|$ is substantially larger than expected. In fact over much of the temperature range the ratio is larger than predicted by the standard London model, which neglects the vortex cores. As the temperature is increased the ratio decreases in both cases, but in the Y compound the ratio then increases above 10K. No such feature is observed in the Lu compound. Neither material shows the expected decrease of this ratio towards 0.21 as $T \rightarrow T_C$, as predicted by the Abrikosov model, which should be appropriate under these conditions. Similar measurements carried out with a larger field of 2.0T applied to YNi_2B_2C showed similar behaviour, with the ratio F_{11}/F_{10} remaining well above the anticipated value approaching T_C.

The ratio F_{11}/F_{10} of both materials, far from B_{C2}, suggests that the field distribution around vortices falls off more steeply than is anticipated from the non-local model, and shows that the non-local model does not provide a good quantitative description of the field variation. In fact, the real space VL appears to be much better described using the standard London approach that cannot account for the VL symmetry transitions observed in these materials. In addition, as the temperature is increased so that the effects of non-locality are reduced, neither compound conforms to the expected Abrikosov-like behaviour. Since the anisotropy of the Fermi surface (via the Fermi averages) is part of the non-local extension to the London model, this suggests that there may be a further source of anisotropy, that remains as T_C is approached, such as an anisotropic superconducting gap Δ. In the non-local theory an isotropic gap is assumed; however, some researchers[5,11-13] have previously

suggested that an anisotropic gap might exist in the borocarbides. Clearly, further theoretical work is needed to determine whether the high values of F_{11}/F_{10} as $T \rightarrow T_C$ are caused by an additional source of anisotropy or by some other mechanism.

An investigation into the internal field distribution (via form factors) has been carried out recently[14] for Sr_2RuO_4, a material of great interest since it is believed that the superconductivity is unconventional. For Sr_2RuO_4, measurement of the form factors of higher order VL diffraction peaks provided further evidence of this unconventional behaviour since the results could not be explained using the standard theories. It is interesting to compare those data with the results obtained from the borocarbides here.

In Sr_2RuO_4 the ratio $|F_{11}/F_{10}|$ showed a similar increase at high temperatures to that seen in the Y compound (B = 0.5T) here. In that work it is suggested that the method used to measure the ratio may result in an overestimation of the intensity of the {11} peaks when intensities become low as the temperature increases. The method used there and here, where data is collected only at the 'rocked-on' position, does of course make no allowance for any changes in lattice quality which would cause adjustments in the intensity observed at any particular point on the peak. However, in this work there is no evidence for a concomitant change in rocking curve width in the Y- material, although there was not sufficient time to collect a high density of points, which implies that changes in vortex lattice quality are not the origin of the increase of the ratio in YNi_2B_2C. Curiously, a more pronounced decrease in rocking curve width is observed in the Lu compound, in which no increase in the ratio is seen. Since the two materials are reported to have very similar structural and electronic properties, and no difference in the strength of vortex pinning between the two has been reported, there is no obvious reason for this discrepancy. The most obvious suggestion is that it relates to the large difference in sample volume (and therefore the scattered intensity for a fixed counting time). The data obtained from the large $LuNi_2B_2C$ crystal has far better statistics. It would be

interesting, if a larger crystal of the Y material could be used, or much greater counting times were available, to see whether the ratio increase is a genuine feature or merely an artefact of the experimental method employed.

It is known that in small fields the VL symmetry in the borocarbides is rhombic, and that increasing the field results in a transition to the square lattice shown here[4-7]. Recently, it has been suggested that, for $LuNi_2B_2C$, as B_{C2} is approached this process occurs in reverse, so that a further increase in field would bring the rhombic lattice back[15]; no square lattice would ever be formed near to B_{C2}. In a field of 0.5T the onset of the transition to the rhombic lattice was observed at a temperature of approximately 8K. The vortex lattice transitions are described in more detail in chapter 7 of this thesis, but crucially the square-to-rhombic transition is characterised by a broadening of the Bragg peak (from a square lattice) in the azimuthal direction (but not the radial direction), and the spot splits into two as the rhombic lattice is formed. The crystal used in that work was the same crystal used here; however, in this work no splitting or change in the shape of the spots on the detector was observed as the temperature was increased in direct contradiction of those results. Additionally, a detailed study carried out recently on YNi_2B_2C also revealed no evidence for the reversed transitions, showing that at fields of about 0.5T and above the square lattice is formed over the full temperature range[9]. These data suggest that no such behaviour occurs in either material investigated in this chapter.

The ultimate aim of these investigations is to reconstruct the real space VL of the non-magnetic borocarbides. The signs of the form factors can be obtained using the technique of muon spin rotation. μSR provides the probability distribution of fields present within the mixed state and as such is sensitive to the signs of the individual form factors. Combined with information about magnitudes of the form factors of higher order terms such as F_{20} from SANS data, a reconstruction of the real space field variation should be possible. This approach was used to obtain the real

space VL[14] in Sr_2RuO_4. Such μSR data have been collected for $LuNi_2B_2C$ on instrument GPS at PSI, Switzerland; analysis of the results is ongoing.

In this chapter the VL of the non-magnetic borocarbides has been examined through the Fourier components or form factor that governs the intensity of Bragg peaks in SANS experiments. For T«T_C, the estimation of the ratio of the first two components, $|F_{11}/F_{10}|$, in Y- and $LuNi_2B_2C$ produced results that do not agree with the predictions made by the current theoretical approach[3] of incorporating non-local extensions within the London model. The higher experimental value for this ratio implies a sharper fall-off of the magnetic field around a vortex than expected. Disagreement with theory was also obtained at temperatures approaching T_C, where the Abrikosov solution for the VL should be appropriate. The anisotropy of the Fermi surface is embedded within the non-local extensions, so that this behaviour of $|F_{11}/F_{10}|$ may be due to another source of anisotropy such as an anisotropic superconducting gap. Clearly, although the current theory predicts the VL symmetry transitions observed in these materials, further work is required to gain an accurate description of the field distribution in the mixed state.

References

[1]   M. Tinkham, *Introduction to Superconductivity* (McGraw-Hill 1975)

[2]   A.A. Abrikosov, Sov. Phys. JETP **5** p1174 (1957) [English translation of Zh. Eksp. Teor. Fiz **32** p1422 (1957)]

[3]   V.G. Kogan *et al.*, Phys. Rev. B **55** No. 14 pR8693 (1997)

[4]   M.R. Eskildsen *et al.*, Phys. Rev. Letts **78** No. 10 p1968 (1997)

[5]   D.McK. Paul *et al.*, Phys. Rev. Letts. **80** No. 7 p1517 (1998)

[6]   P.L. Gammel *et al.*, Phys. Rev. Letts **82** No. 20 p4082 (1999)

[7]   M.R. Eskilsden *et al.*, Nature **393** p242 (1998)

[8]   V.G. Kogan *et al.*, in *The Superconducting State in Magnetic Fields* p127

(World Scientific 1998)

[9]   S.J. Levett *et al.*, to be published

[10]   K.D.D. Rathnayaka *et al.*, Phys. Rev. B **55** No. 13 p8506 (1997)

[11]   T. Terashima *et al.*, Phys. Rev. B **56** No. 9 p5120 (1997)

[12]   I.S. Yang *et al.*, Phys. Rev. B **62** No. 2 p1291 (2000)

[13]   T. Yokoya *et al.*, Phys. Rev. Letts. **85** No. 23 p4952 (2000)

[14]   P.G. Kealey *et al.*, Phys. Rev. Letts. **84** No. 26 p6094 (2000)

[15]   M.R. Eskildsen *et al.*, Phys. Rev. Letts. **86** No. 22 p5148 (2001)

Chapter 6

Magnetic Structures in ErNi$_2$B$_2$C

6.1 Introduction

The rare earth nickel borocarbides exhibit a variety of magnetic structures in zero applied field and also undergo a series of metamagnetic transitions when a field is applied. In ErNi$_2$B$_2$C, superconductivity coexists with antiferromagnetism[1-5] below T$_N$ ~ 5.8K, and it has been proposed[6] that a weak ferromagnetic component develops at low temperatures, without destroying superconductivity. In this chapter both the ferromagnetic component and metamagnetic phases of ErNi$_2$B$_2$C are investigated.

The zero field magnetic structure of ErNi$_2$B$_2$C is a transversely polarised, incommensurate spin density wave (SDW) below T$_N$[1,2]. The magnetic transition is accompanied by a small orthorhombic distortion of the crystal lattice[3]. High resolution magnetic x-ray scattering[4] has indicated that the modulation wave-vector is along the slightly longer a-direction, so that the moments point along b. In that work a modulation wave-vector of (0.5537,0,0) was obtained at 4.2K. Previous work has shown that as the temperature is lowered, higher order satellites are observed as the modulation of the moments 'squares up'[1,2,5].

The possibility that superconductivity could coexist with some sort of weak ferromagnetism at low temperatures in ErNi$_2$B$_2$C was first suggested by Canfield et $al.$[6] Magnetisation measurements showed that a small ferromagnetic component developed below a temperature of 2.3K for magnetic fields applied within the ab plane. Cho et $al.$[7] had also observed a change in slope at around 2.3K in the heat capacity of an ErNi$_2$B$_2$C crystal. This proposed weak ferromagnetism, observed for

applied fields well below the upper critical field B_{C2} (approximately 1.3T at 2K for **B** // ab[6]), coexists with superconductivity – a highly unusual situation among magnetic superconductors, and unique within the borocarbide family. The calculated average internal field induced by the ferromagnetic moment (the magnetisation measurements indicated a magnitude of $0.33\mu_B$ per Er site) was of a similar magnitude to the estimated lower critical field - $B_{C1} \approx 50mT$ [6]. The only other borocarbide in which a ferromagnetic component has been observed is the non-superconducting compound $TbNi_2B_2C$[8,9,10]. In that material a ferromagnetic component develops at about 8K; the ferromagnetic moment is larger than that suggested for $ErNi_2B_2C$ and induces an average internal field comparable to the estimated thermodynamic critical field B_C of the superconducting borocarbides (typical estimates for B_C in $ErNi_2B_2C$ are $250mT$[6] and $120mT$[7]). It is thought that this might be the cause of the absence of superconductivity in the Tb material, while the smaller moment observed in $ErNi_2B_2C$ allows superconductivity to coexist with the weak ferromagnetism[6].

Further experiments carried out on $ErNi_2B_2C$ by Gammel *et al.*[11] investigated the impact of this low temperature phase on the superconductivity. Magnetisation loops showed larger hysteresis in low fields (below 0.4T) below 2.3K than at higher temperatures, suggesting that the pinning forces acting on vortices are increased in the ferromagnetic phase. The effect was strongest when the magnetic field was applied along the crystal [1 1 0] direction, but was also observed for fields applied along other directions within the ab plane, and along c. This was reinforced by transport data that showed a definite increase in the de-pinning critical current at low temperatures. The enhanced pinning forces were attributed to increased pair-breaking in the ferromagnetic phase.

The first reported neutron scattering measurements looking at the new ferromagnetic phase were carried out by Kawano *et al.*[12]. The crystal used in that work was very large and had $T_C(0) \sim 8.7K$ rather than the usual 10.5K, indicating

that the quality of the crystal was lower than usual. A small increase in the intensity of some nuclear Bragg peaks was observed below 2.5K and attributed to the ferromagnetic component. Subsequent work, using polarized neutrons[13], eliminated the possibility that this extra intensity was due to structural changes rather than a magnetic transition. Further, in zero field and at 1.4K a new set of peaks was observed in addition to those expected from the SDW. These new peaks were not observed at 4K and were also ascribed to the ferromagnetic component.

Magnetisation measurements have shown that ErNi$_2$B$_2$C undergoes several metamagnetic transitions when magnetic fields are applied perpendicular to c below T_N[14,15]. Some of these occur in the vicinity of the superconducting upper critical field B_{C2} at low temperatures. The number and location of these transitions varies with the relative orientation of the crystal to the applied field as well as with temperature. The critical fields occur at their lowest values when the magnetic field is applied along [1 0 0], the magnetic easy axis for this material, and increase as the angle between the field and [1 0 0] is increased to a maximum when the field is along [1 1 0][15]. Previous neutron scattering experiments[16,17] investigating the metamagnetic transitions focussed on the behaviour of the fundamental magnetic peak and a nuclear peak as a function of field applied along [1 0 0] and [1 1 0]. For both orientations, two transitions involving changes in the magnitude of the modulation wave-vector were observed below T_N, followed by a transition to a saturated paramagnetic state where all spins are held parallel (as in a ferromagnet) by the applied magnetic field.

In this work neutron diffraction has been used to investigate the magnetic structures that exist in ErNi$_2$B$_2$C both with and without an applied magnetic field. An investigation into the ferromagnetic component formed at low temperatures in zero field was carried out on the diffractometer D10 (ILL). SANS measurements (D22,ILL) have revealed diffuse scattering along the principal axes both in zero field and co-existing with the vortex lattice (VL). Experiments examining the

metamagnetic transitions for fields applied along [2 1 0], intermediate between the directions previously studied[16,17], and the subsequent additional investigations with fields applied along [1 0 0] and [1 1 0] were carried out on D23, also at ILL.

6.2 Sample Characterisation

The ErNi$_2$B$_2$C crystal used in the neutron diffraction studies has been characterised in our laboratory to accompany the neutron diffraction work. The characterisation measurements also enable comparison with the results published on this material by others. This crystal, of mass 15.3mg, was grown by the high temperature flux method described in chapter 3 for this work and was also used for the vortex lattice experiments presented in chapter 7.

Figure 6-1 shows the heat capacity of the ErNi$_2$B$_2$C crystal. No magnetic field has been applied. The data is dominated by the strong peak at 5.8K, the antiferromagnetic ordering temperature. There is also a small, broad feature at lower temperatures that is reported to arise due to the formation of the weak ferromagnetic state below ~2.3K[6]; this feature is observed more clearly in the derivative (inset to figure 6-1).

Magnetisation was measured as a function of temperature for different applied fields. M-T measurements were carried out with fields applied along three directions within the *ab* plane, namely [1 0 0], [1 1 0] and [2 1 0]. Representative data for B // [1 1 0] is presented in figure 6-2 and shows the temperature dependence of the magnetisation when warming the crystal in an applied field of 100mT after cooling to 1.7K in zero field. As well as features at the superconducting transition T$_C$ (which is a little lower than 10.5K as would be expected on applying a small field) and antiferromagnetic ordering temperature T$_N$ there is an increase in magnetisation at lower temperatures with a broad maximum at around 2.4K. Similar behaviour was observed for all three orientations of the crystal relative to the applied
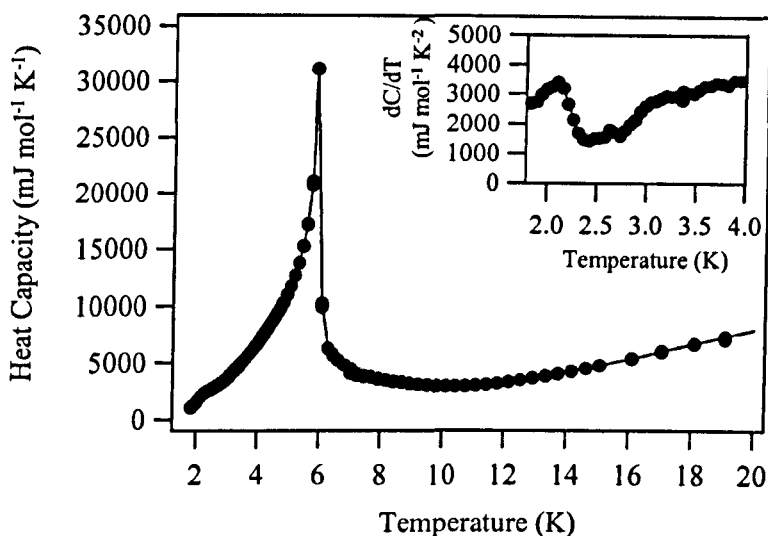
Figure 6-1: Heat capacity of single crystal $ErNi_2B_2C$, measured in a Quantum Design calorimeter by Dr M.R. Lees. The magnetic transition is clearly shown at 5.8K; the feature at low temperatures is emphasised in the derivative (inset).
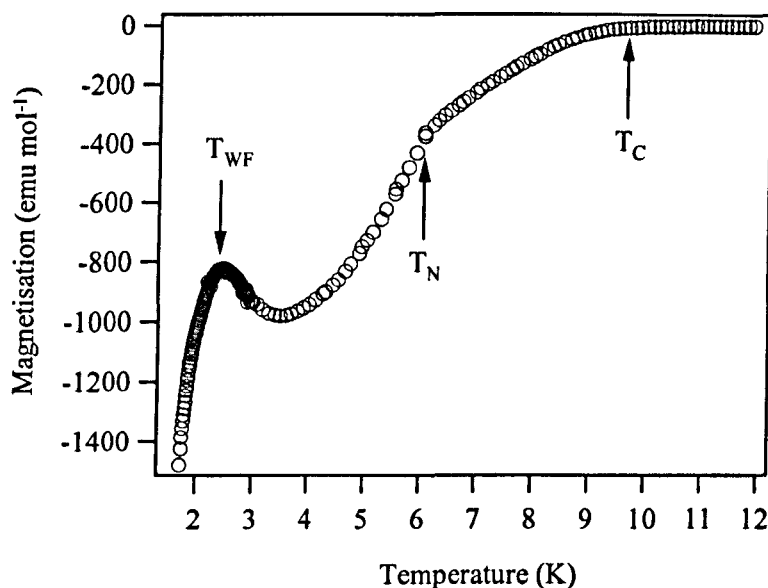
Figure 6-2: Magnetisation of $ErNi_2B_2C$ warming in a field of 100mT applied along [1 1 0] after cooling to 1.6K in zero field. The superconducting (T_C) and antiferromagnetic (T_N) transitions are indicated, as is the suggested T_{WF}.

field. It has been suggested that the increase in magnetisation at low temperatures is caused by the development of the ferromagnetic component[6].

Detailed magnetisation vs applied field loops in low applied fields (maximum ± 0.3T) were performed over a range of temperatures for the three different crystal orientations. For each loop, the difference between the magnetisation in increasing and decreasing applied fields ΔM was calculated, not including the virgin curve. The hysteresis is directly proportional to the pinning force. The data for B // [1 1 0] is shown in figure 6-3. Data were collected at many temperatures but a relevant selection at steps of 0.2K are shown for clarity. There is a clear increase in the hysteresis as the temperature is decreased; similar behaviour was observed for the other orientations. A shoulder also develops at around 120mT; Gammel *et al.*[11] attributed this effect to a low field metamagnetic transition. Figure 6-4 shows the difference in magnetisation ΔM at zero field as a function of temperature for this orientation. This data includes data points from every measured temperature and shows the increase in ΔM at low temperatures very clearly, emphasising the increase in hysteresis below about 2.3K.

In addition to the detailed low field measurements, magnetisation data were collected up to higher applied fields to accompany the neutron diffraction investigations of the metamagnetic transitions presented in the second half of this chapter. Figure 6-5 shows data collected at 2K in increasing field for all three orientations. The data show several transitions for each orientation and illustrate the effect of varying the relative orientation of the crystal and the applied magnetic field.

All of these results are in good agreement with the published works[6-11,14,15], indicating that this ErNi₂B₂C crystal, used in all of the neutron diffraction experiments described in this thesis, has very similar magnetic properties to those used elsewhere.
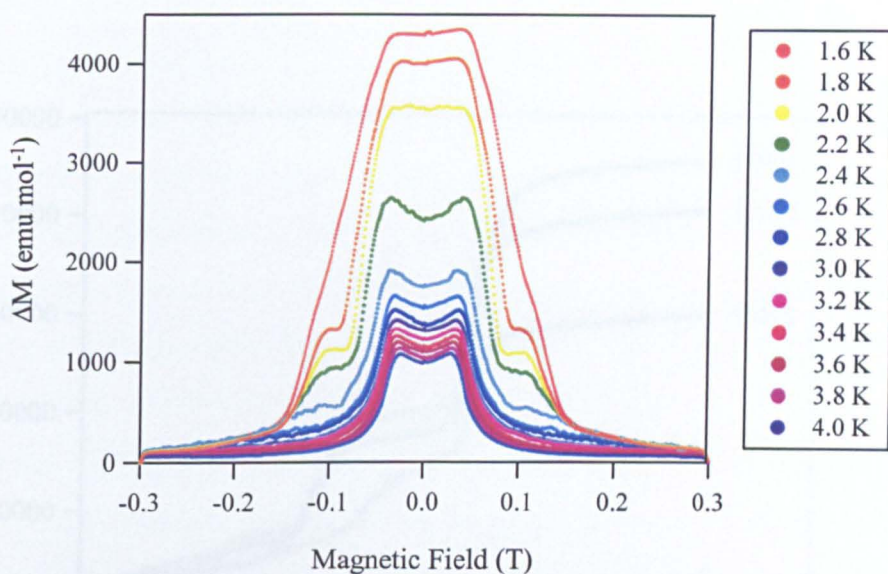
Figure 6-3: Hysteresis in the magnetisation of $ErNi_2B_2C$ with a field applied along [1 1 0] at different temperatures. The virgin curve is not included.
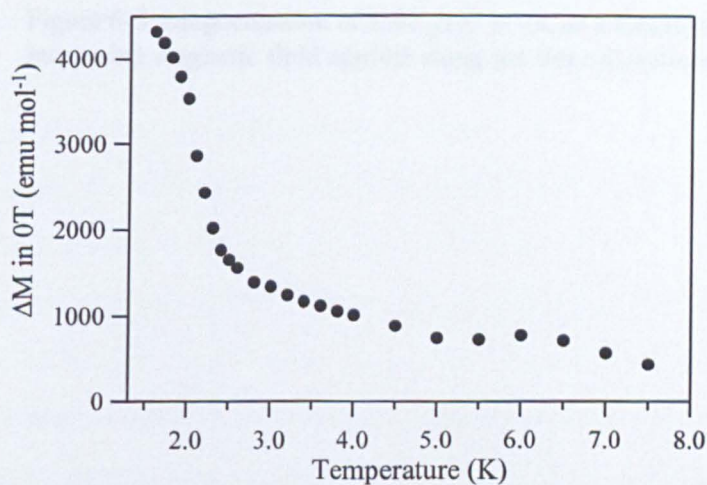
Figure 6-4: Hysteresis at zero field as a function of temperature extracted from data represented in figure 6-3; again the field is along [1 1 0].
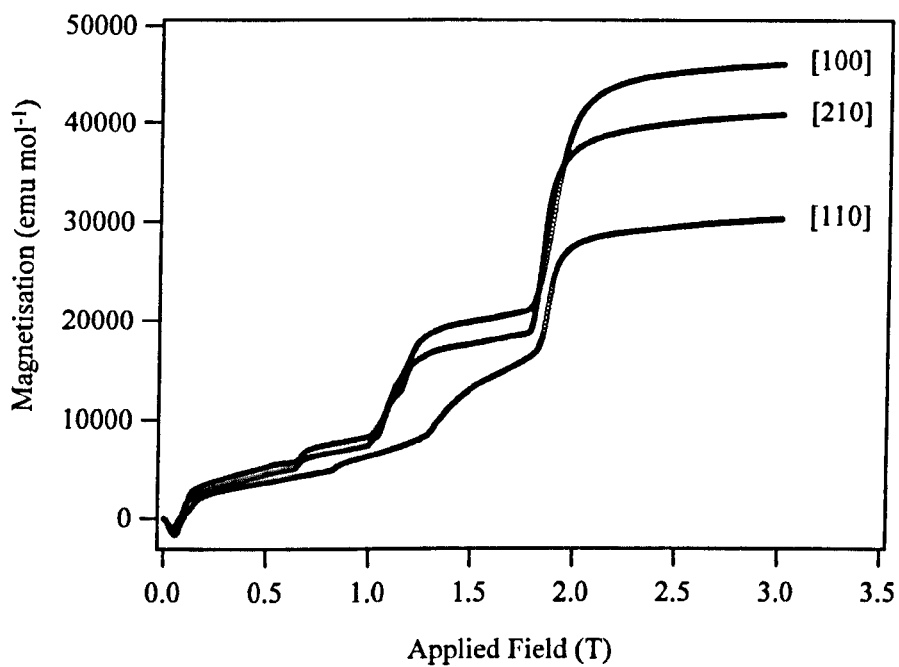
Figure 6-5: Magnetisation of $ErNi_2B_2C$ at 2K as a function of increasing magnetic field applied along the three directions indicated.

6.3 The Ferromagnetic Component in ErNi$_2$B$_2$C

6.3.1 Low Temperature Magnetic Structure in Zero Field

Elastic neutron diffraction was carried out on the diffractometer D10 at ILL. The instrument was set up in two-axis, four circle mode with a cryostat providing access to temperatures down to 150mK. The neutron wavelength used was 2.36Å, from a pyrolytic graphite (PG) (0 0 2) monochromator; neutrons were detected by means of a 32 x 32 pixel (80 x 80mm) area multi-detector. The crystal was mounted with the crystal [0 1 0] direction perpendicular to the scattering plane.

After cooling, the crystal alignment was checked and diffraction profiles collected at various temperatures. Figure 6-6 shows data obtained at 2.6K, above the proposed transition to a weak ferromagnetic state. A nuclear peak is observed at (1 0 $\bar{1}$) as expected for a body centred tetragonal crystal structure which produces peaks only at h + k + l = 2m for integer m. The orthorhombic distortion is too small to be resolved in this experiment. An antiferromagnetic SDW along the a-axis should produce magnetic peaks at (h ± nq k l), again for h + k + l = 2m where n is an odd integer and q is the modulation wave vector of the SDW. The strong fundamental (n = 1) magnetic peak from the SDW is clearly observed at approximately (0.45 0 $\bar{1}$). Fitting this peak with a Gaussian function yields a modulation wave vector at this temperature of q = 0.5508(1)a*. In real space this corresponds to a slightly longer modulation (repeating over ~71Å, or 19.7 crystal unit cells) than that of 0.5526a* (~67Å) quoted by Lynn et al.[10] at higher temperatures, and 0.5537a* observed by Detlefs et al.[4] at 4.2K. In addition to the fundamental peak, a third order satellite is present at approximately (0.65 0 $\bar{1}$), and there is evidence of the much weaker seventh order satellite at around (h + 7q 0 $\bar{1}$). The position of the fifth order (n = 5) satellite is outside the scope of this scan but the presence of the very weak seventh order peak implies that it would be observed if a more extensive scan had been performed. These higher order satellites correspond to higher order Fourier

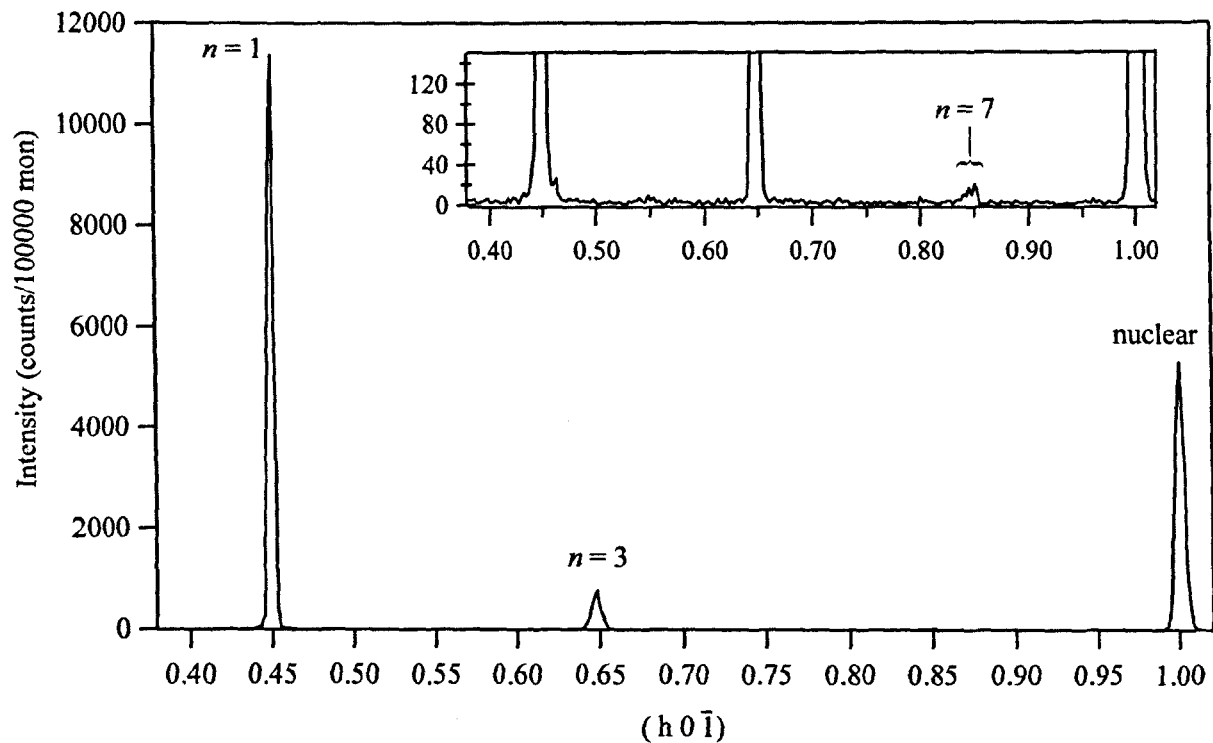Figure 6-6: Diffraction pattern obtained from $ErNi_2B_2C$ in zero field at 2.6K. The order of the magnetic peaks are indicated and the nuclear peak identified. The inset shows an expanded scale that reveals the 7th order magnetic harmonic.

components of the real space distribution of moments and indicate how 'squared up' the moment distribution is at this temperature. For a square wave the structure factor of an nth order satellite should be $1/n$ of the fundamental peak. The ratio of the structure factors of the fundamental and third order peaks were calculated and a value for $F_{hkl}(n = 3) / F_{hkl}(n = 1)$ of 0.32(2) obtained. This agrees well with the result of Lynn et al.[10] who followed the intensity of both peaks with temperature and obtained a similar value at around 2K. At 2.6K therefore the diffraction pattern corresponds to a reasonably square SDW with the modulation along the a-axis, as expected.

Closer examination of the higher order satellites indicates that the situation is more complicated than suggested above. The 7th order satellite is split into a number of very weak peaks, implying that there are in fact several modulations present. This suggests that different regions exist within the sample that have different modulation lengths. This could be related to the different domains of crystal orientation that develop as the orthorhombic distortion occurs below T_N, or other crystal defects that force the magnetic structure to assume slightly different modulations. Since these modulations are very similar in magnitude this is not immediately evident if only the fundamental peak is considered, but is only observable at higher orders. In fact, the Gaussian fit of the third order satellite gives a width close to twice the value obtained from the fundamental peak, providing further evidence of the presence of multiple modulations. Unfortunately, with such weak peaks at the $n = 7$ position, and without resolvable splitting of lower order peaks in this data, it is impossible to accurately determine the precise number and length of the different modulations. For this, better statistics and/or resolution are needed. Analysis of only the fundamental peak therefore provides an inadequate indication of the magnetic behaviour of this crystal.

The same scan carried out at 1.9K, below the suggested T_{WF} at 2.3K, is shown in figure 6-7. As well as the fundamental magnetic peak and the higher order satellites observed at 2.6K, peaks are present at all observable positions of $(h \pm nq \; 0 \; \bar{1})$
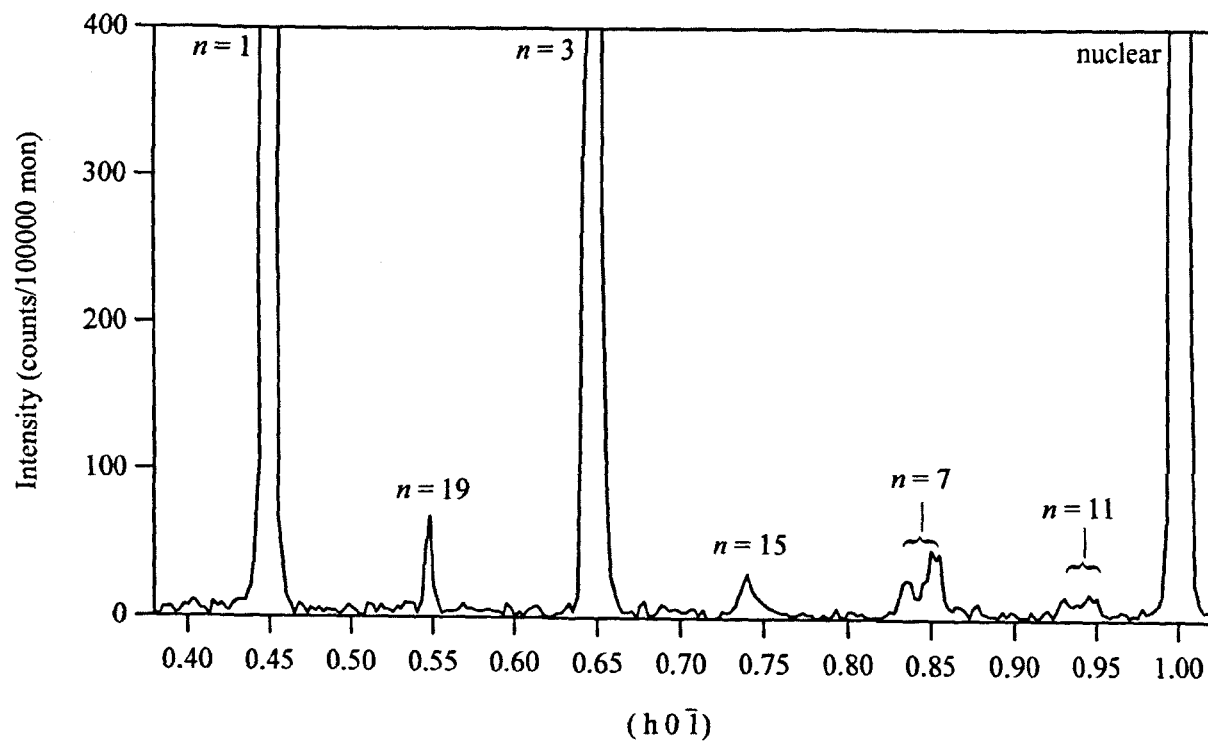
Figure 6-7: Diffraction pattern obtained from $ErNi_2B_2C$ in zero field at 1.9K, showing extra peaks of apparently high order. The order of each satellite is indicated.

with n-odd. Again, there is distinct splitting of many of the higher order satellites, indicating that there are still several different modulations present at this temperature. Of the new peaks, that at $n = 19$ is strongest, and it is in fact visibly stronger than even the 7th order peak(s). This is incompatible with the simple Fourier analysis of a square wave described above, since a 19th order peak should obviously be weaker than all peaks of lower order. The $n = 15$ peak is also stronger than expected. In addition, unlike many of the lower order peaks, there is no splitting of the 19th order satellite, which corresponds to a modulation of 0.5502(1)a*.

Figure 6-8 shows the same scan carried out at 0.15K, well below the proposed transition at 2.3K. At this temperature, peaks occur at approximately ($h \pm nq$ 0 $\bar{1}$) for *all* integer n, even and odd. Under the antiferromagnetic SDW scenario, even-ordered peaks are not expected. All of the peaks observed at 1.9K and 2.6K are still present, so the structure must still be based on the SDW. Higher odd-ordered satellites show that the structure consists of more than one modulation, which is consistent with the results at higher temperatures.

The even-ordered satellites, in contrast to most of the odd-order satellites such as the 7th, do not show the prominent splitting caused by multiple modulations. These even ordered peaks (such as the $n = 12$ peak close to 0.4 0 $\bar{1}$) consist of a strong peak, in some cases accompanied by a much weaker one at a slightly different modulation. Analysis of the 12th order peak yields a modulation of 0.5500(2)a*, which is in fact a commensurate modulation repeating over 20 crystal unit cells or approximately 72Å. Analysis of the other strong even-ordered satellites yields similar values in every case. The results are listed in table 6-1. This result implies that a single modulation, one that is commensurate with the underlying crystal lattice, is primarily responsible for the appearance of these new peaks while any other modulations that are present are either not involved or make only a very small contribution.
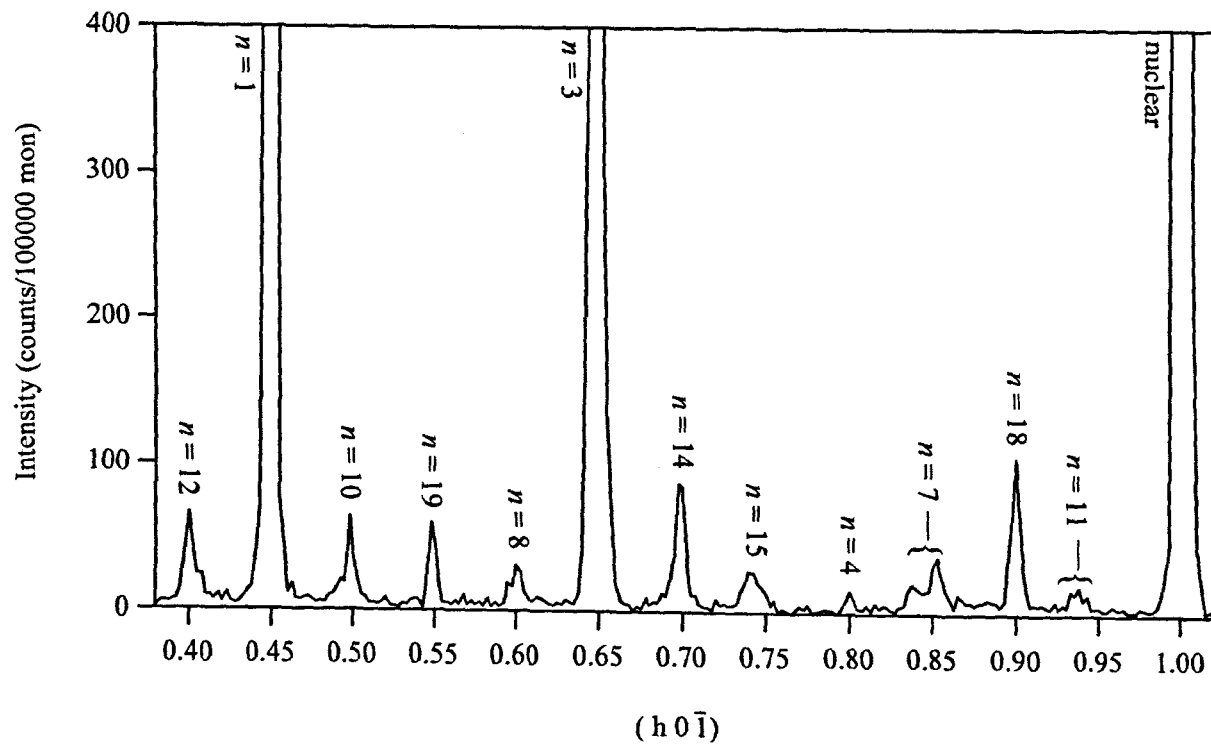
Figure 6-8: Diffraction pattern obtained from $ErNi_2B_2C$ in zero field at 0.15K, showing odd and even order peaks.

n	q (a*)
4	0.5500(3)
8	0.5499(2)
10	0.5498(2)
12	0.5500(2)
14	0.5499(1)
18	0.5500(1)

Table 6-1: Modulations calculated for even-ordered satellites at 0.15K.

This scan was repeated at temperature intervals of 0.1K from 1.6K up to 2.6K, providing information about the temperature dependences of the different reflections. A selection of peaks were also scanned at lower temperatures (T < 1.6K) to check that no other changes in the magnetic structure occur. Because of the splitting observed for several of the peaks, the temperature dependence of each peak or group of peaks with the same n were obtained by summing the number of counts within an appropriate and consistent section of the scan containing the peak(s) under consideration. Although attempts were made to follow the temperature dependences of individual modulations, unfortunately those peaks that show the largest splitting are also the weakest, and it has proved difficult to extract reliable information through fitting methods.

Figure 6-9 shows the temperature dependence of the n-odd peak centred on (0.55 0 $\bar{1}$). This peak has $n = 19$. However, the temperature dependence does not resemble that of a higher order harmonic (such as the $n = 7$ peak below), and has a convex shape. This sort of temperature dependence is observed at phase transitions. The onset of the apparent transition is just below 2.3K, a temperature similar to the transition temperature of the weak ferromagnetic phase estimated from the magnetisation measurements and heat capacity. The intensity of this peak reaches saturation below about 1.7K and then remains essentially constant. The intensity of the n-odd peak at approximately (0.75 0 $\bar{1}$) ($n = 15$) showed similar behaviour, with an onset at around 2.4K. From this evidence, it appears that the high n-odd peaks are

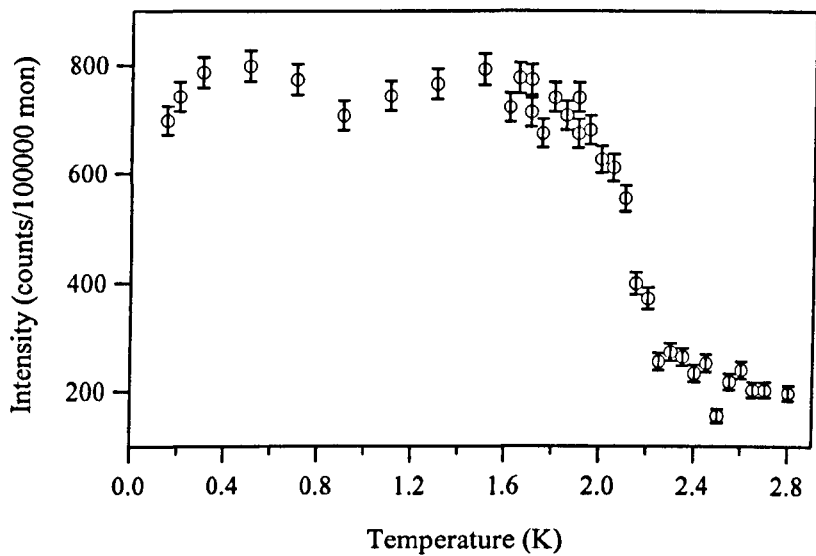Figure 6-9: Temperature dependence of n = 19 peak in $ErNi_2B_2C$, using the sum of counts in scan section method.

not higher order harmonics of the SDW but instead are caused by a change in the magnetic structure.

The measured temperature dependences of the n-even peaks again show the convex shape but this time at a different temperature. Figure 6-10 shows the temperature dependence of the n-even peak at (0.4 0 $\bar{1}$) (n = 12). Again the summation method has been used to obtain the temperature dependence. In contrast to the n-odd peaks, the intensity of this peak increases suddenly below 1.8K, reaching a maximum by about 1.5K and falling very slightly as the temperature is further decreased. All of the n-even peaks contained in the scan show this sudden increase at 1.8K. There is also some intensity above 1.8K, persisting to about 2.3K. For this peak the temperature dependence was also measured by calculating the integrated intensity using a Gaussian fit. Using that method the intensity above 1.8K is no longer observed; this intensity appears to derive from the background rather than from the peak itself.

Figure 6-11 shows the temperature dependence of the group of peaks at ~ (0.85 0 $\bar{1}$), which have n = 7. This group first appears below around 3.5K as would be expected when the SDW squares up with decreasing temperature. The concave shape of this temperature dependence is what would be expected from a harmonic in contrast to the n = 19 and n = 12 peaks shown above. There is no apparent feature at the suggested T_{WF} at around 2.3K; however, the intensity *decreases* at lower temperatures after reaching a maximum at 1.8K. Comparison with the complete scan carried out at 0.15K (figure 6-8) combined with the information obtained about the low temperature behaviour of other peaks (above) suggests that the intensity of this peak will probably remain effectively constant after this initial decrease. Similar behaviour was observed for the 5th and 11th order satellites. No decrease in the intensities of either the fundamental SDW peak or the third order satellite was observed over the range of temperatures studied. The decrease in the intensities of the higher odd-order satellites coincides with the emergence of the n-even peaks
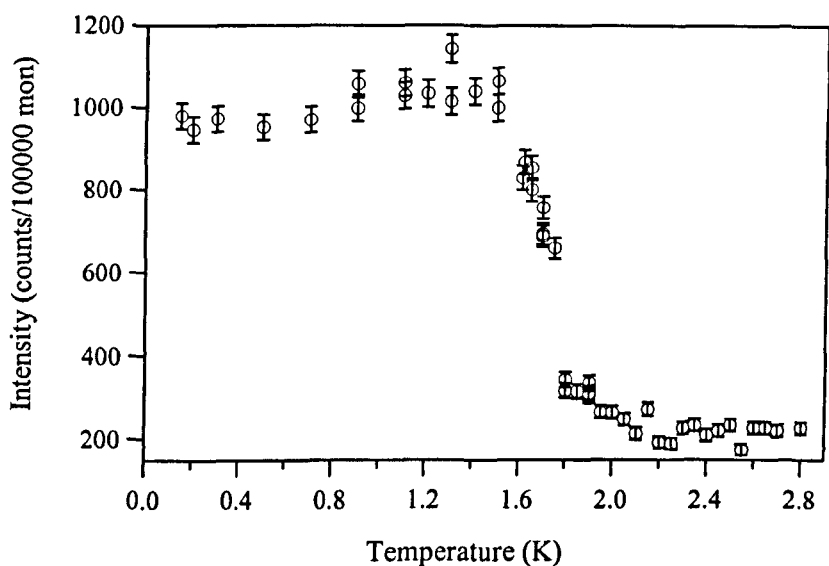
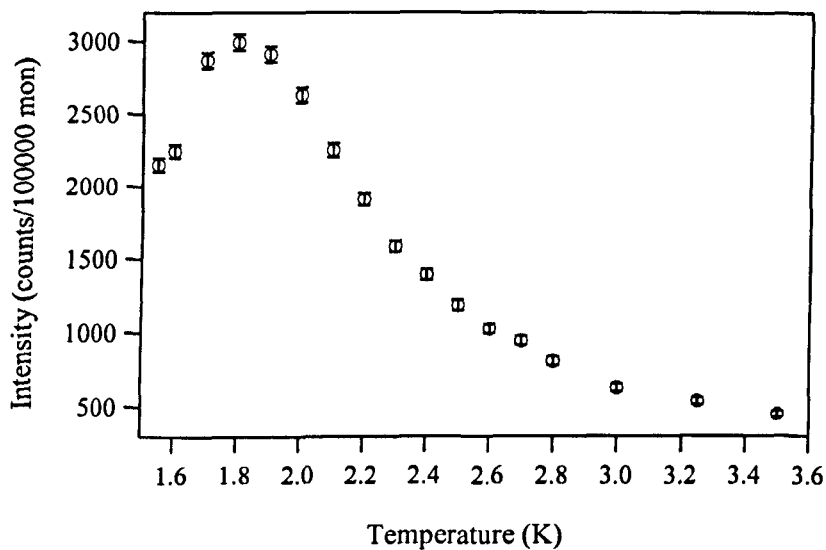Figure 6-10: Temperature dependence of $n = 12$ peak in $ErNi_2B_2C$ (summation method).

Figure 6-11: Temperature dependence of $n = 7$ peaks (summation method)

below 1.8K, implying that an adjustment in distribution of moments in the SDW occurs when the n-even peaks emerge.

In combination these data suggest that more than one change in the distribution of magnetic moments takes place as the temperature is lowered. The SDW formed below T_N begins to square up with decreasing temperature, as expected; this is indicated by the emergence of higher order satellites such as the 7th at around 3.5K. Below 2.3K, which corresponds to the weak ferromagnetic ordering temperature suggested by magnetisation and heat capacity results, peaks emerge at all (h $\pm$ nq 0 $\bar{1}$) for odd integer n; their temperature dependences indicate that these peaks are due to some sort of phase transition. Finally, a second phase transition causes the sudden appearance of peaks with even n below 1.8K. No further changes are detected down to 0.15K.

Figure 6-12 shows the variation in the integrated intensity of the nuclear (0 0 2) peak with temperature. The peak has been fitted to a Gaussian function. In contrast to the results of Kawano et $al.$[12], no discernible features are observed at 2.3K or at any temperature over the range studied. This was also the case for other nuclear peaks studied. Clearly, in this sample, the development of the 'ferromagnetic' phase at low temperatures does not include any observable increase at the nuclear positions.

6.3.2 Small Angle Scattering Results

During small angle scattering experiments carried out to investigate the properties of the vortex lattice in ErNi$_2$B$_2$C (chapter 7) unusual and unexpected features relating to the magnetic structures in the crystal were observed. By adjusting the wavelength and sample-to-detector distance to shorter values it is possible to investigate the behaviour at larger values of scattering vector $\mathbf{Q}$ than is usually necessary when examining the vortex lattice. Figure 6-13 shows data obtained in zero applied field at 1.6K with the detector at 11.2m using a wavelength of 4.55Å. This image was produced by rotating the sample through ω and ϕ (see figure 4-6)
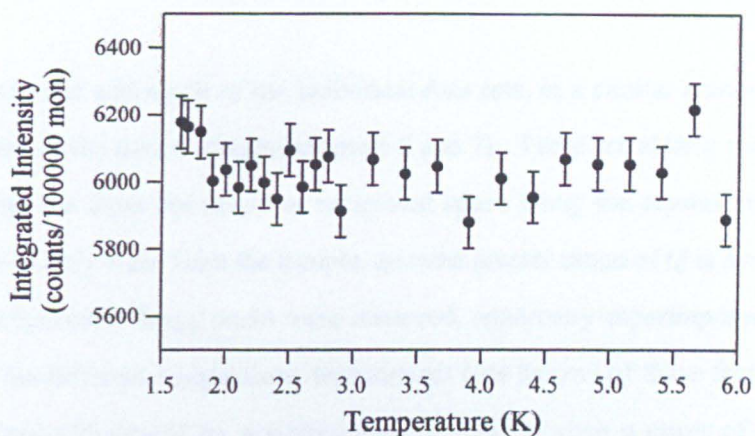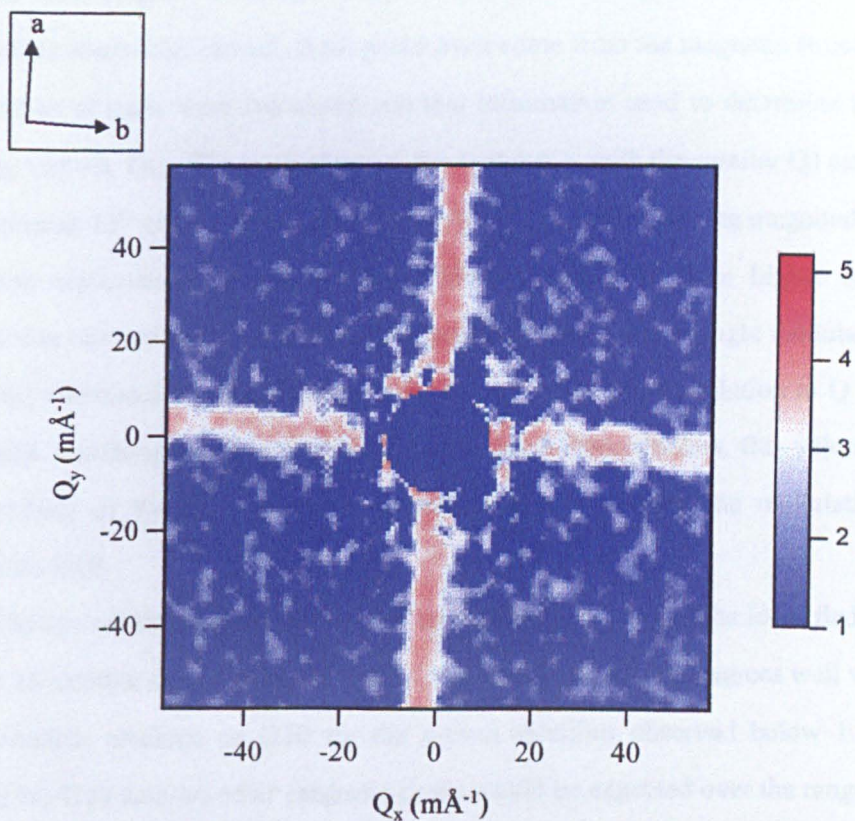
Figure 6-12: Temperature dependence of (0 0 2) peak in ErNi₂B₂C

Figure 6-13: SANS image obtained from ErNi₂B₂C at 1.6K
in zero magnetic field. The intensity scale is logarithmic.

separately and adding all of the individual data sets, in a similar manner to that used to collect vortex lattice images (chapters 5 and 7). There are clearly rods of intensity extending out from the origin of reciprocal space along the crystal axes. With the detector at only 3.2m from the sample, an even greater range of **Q** is available, and in this configuration Bragg peaks were observed, apparently superimposed on the rods. Due to the different temperature dependences (see below) of these features, they are most clearly illustrated by summing images obtained over a range of temperatures, and this is presented in figure 6-14.

From the positions of the Bragg peaks on the detector it is possible to determine their origin. Their scattering vectors are too large to be attributed to vortex lattice scattering; instead, these peaks must come from the magnetic structure. Their centres of mass were calculated and this information used to determine their scattering vectors, Q_{hk}. The peak closer to the centre (i.e. with the smaller **Q**) can be identified as an 11th order satellite from the SDW, with a corresponding magnitude of modulation wave-vector of 0.5507(2)a*. Since splitting of these higher order satellites was observed on D10 it is perhaps misleading to quote a single modulation magnitude; additionally, a SANS instrument has relatively poor resolution in **Q** due to the large wavelength spread (typically $\delta\lambda/\lambda \sim 10\%$). Nevertheless, this value for the magnitude of the modulation wave-vector agrees well with the modulations observed on D10.

The second Bragg peak, further out on the detector, can also be identified. It is an $n = 18$ satellite from a modulation of 0.5502(2)a*. Again, this agrees well with the information obtained on D10 for the n-even satellites observed below 1.8K. Based on the D10 data, no other magnetic peaks would be expected over the range of **Q** observed here, which strongly implies that the rods of intensity are genuine, rather than made up of many individual Bragg peaks.

The temperature dependences of these two Bragg peaks as well as a section of the rod were measured. For the Bragg peaks, the instrument angles were set at the
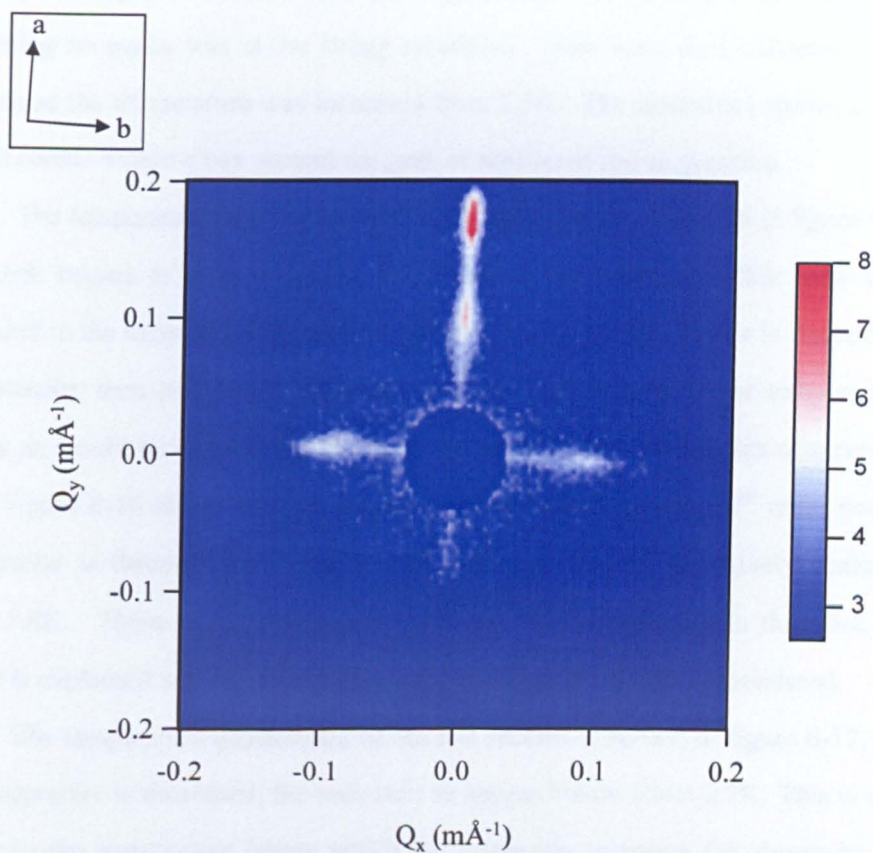
Figure 6-14: Sum of SANS images collected in zero field over a range of temperatures showing Bragg peaks superimposed on rods of intensity in $ErNi_2B_2C$.

positions of maximum intensity based on measurements of the rocking curve (i.e. intensity vs angle). For the rod, the angles were set so that a section of rod containing no peaks was at the Bragg condition. Data were then collected at that position as the temperature was increased from 1.5K. The intensities shown are the sum of counts within a box around the peak or section of rod in question.

The temperature dependence of the 11th order satellite is shown in figure 6-15. The peak begins to emerge below 3K, which is reasonable for this peak when compared to the temperature dependence of the 7th order satellite shown in figure 6-11. The intensity then peaks at 1.8K before decreasing rapidly at lower temperatures, exactly as would be expected if these are the same type of harmonics observed on D10. Figure 6-16 shows that the temperature dependence of the 18th order peak is also similar to those of the n-even peaks measured on D10, effectively vanishing above 1.8K. There is some intensity persisting up to 2.2K, but in this case this feature is explained when the temperature dependence of the rod is considered.

The temperature dependence of the rod section is shown in figure 6-17. As the temperature is decreased, the rods start to appear below about 2.2K. This is very similar to the temperature below which the hysteresis increases (as shown by the magnetisation results), a broad feature in the heat capacity is observed, and the very high order harmonics develop. Attempts to observe this diffuse scattering by standard diffraction on D10 were unsuccessful, but as the rods are so weak, the very high neutron flux on D22 compared to that available on D10 may explain this failure. Over the range of **Q** investigated, there are no discernible features or gaps along the rods, other than where magnetic Bragg peaks are clearly superimposed upon them.

As well as these zero field observations, in the SANS geometry it was possible to apply magnetic fields of up to 500mT along the crystal c-axis. Figure 6-18 shows data obtained at 1.6K in an applied field of 450mT, using a neutron wavelength of 10Å and with the detector at 10m from the sample. This data clearly shows first and second order diffraction at small **Q** resulting from the vortex lattice,
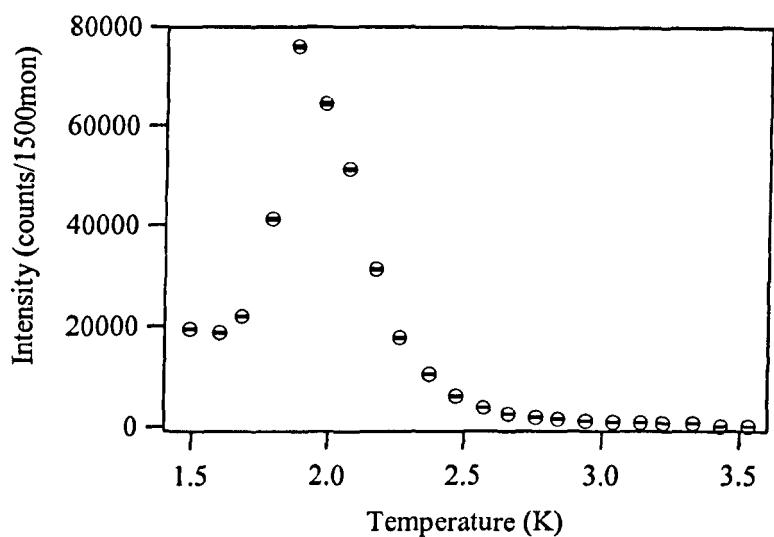
Figure 6-15: Temperature dependence of the $n = 11$ satellite from ErNi$_2$B$_2$C SANS data. A background at 3.6K has been subtracted.
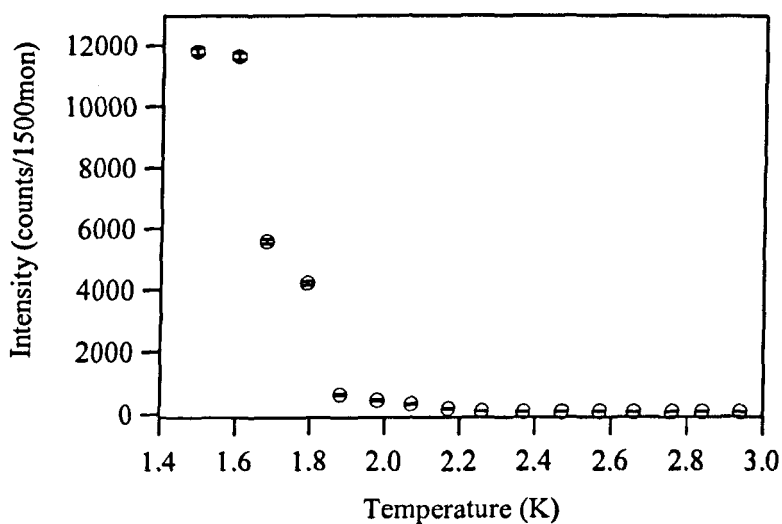
Figure 6-16: Temperature dependence at the position of the $n = 18$ satellite from SANS data. A background at 3.6K has been subtracted.

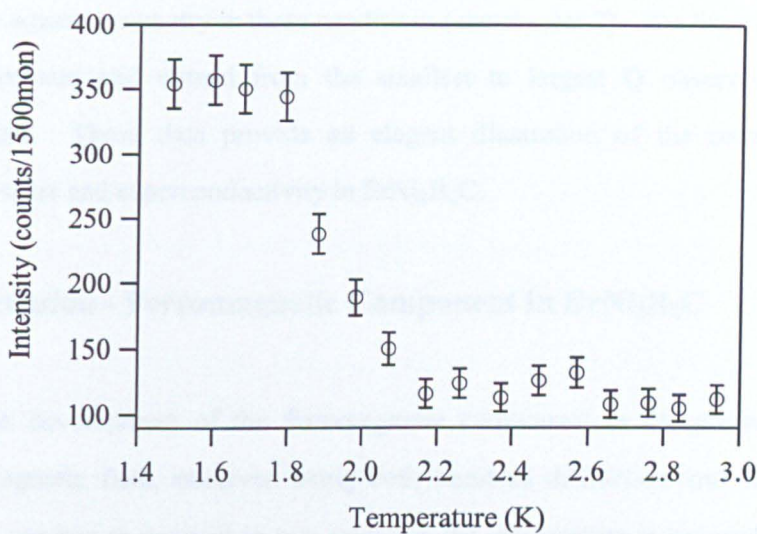Figure 6-17: Temperature dependence of rod section in $ErNi_2B_2C$. A background at 3.6K has been subtracted.
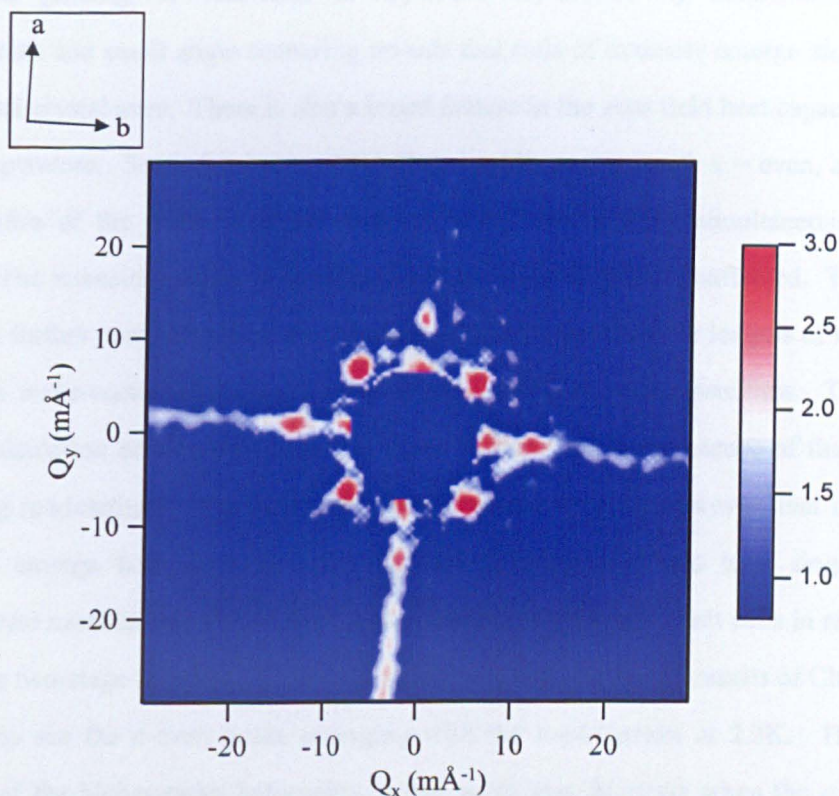

Figure 6-18: SANS image obtained at 1.6K (partial rock) in an applied field of 0.45T. A background at 12K has been subtracted. The four strongest spots are the (10) peaks from the vortex lattice. The intensity is logarithmic.

which has square symmetry in these conditions (see chapter 7). The lines of intensity are still present and extend from the smallest to largest $\mathbf{Q}$ observable in this arrangement. These data provide an elegant illustration of the coexistence of magnetic order and superconductivity in $ErNi_2B_2C$.

6.4 Discussion - Ferromagnetic Component in $ErNi_2B_2C$

The development of the ferromagnetic component in the absence of any applied magnetic field, observed using both standard diffraction and small angle scattering, appears to proceed in two stages as the temperature is lowered. First, at about 2.3K (T_{WF1}) satellites start to appear at all n = odd positions not already occupied by higher order satellites at higher temperatures. In the same temperature region, the pinning of flux-lines is enhanced as shown by magnetisation measurements and small angle scattering reveals that rods of intensity emerge along the principal crystal axes. There is also a broad feature in the zero field heat capacity at this temperature. Secondly, below 1.8K (T_{WF2}) peaks emerge with n = even, and the intensities of the SDW satellites such as n = 7 and n = 11 simultaneously decrease. The intensities of the peaks that appeared below 2.3K are unaffected. The situation is further complicated by the presence of several very similar lengths of the modulation wave-vector, as shown by the splitting of higher order satellites. The accurate calculation of structure factors is made difficult by the existence of these overlapping modulations. The data at low temperatures suggest, however, that the peaks that emerge both at 2.3K and 1.8K are principally related to a single, commensurate modulation of (0.55,0,0), corresponding to 20 crystal unit cells in real space. This two-stage development is in disagreement with the recent results of Choi et al.[18], who see the n-even peaks emerging with the n-odd peaks at 2.3K. The intensities of the higher order harmonics in that work also decrease when the n = even peaks emerge, but in that case this is below 2.3K. Since the magnetisation data

obtained on the crystal used here (§6.2) are very similar to the published results, with the increase in hysteresis occurring below 2.3K and no feature seen at 1.8K, where our n = even peaks emerge, this is a strange contradiction. The results obtained from the small angle scattering work, where again 1.8K is the temperature at which the n = even peaks emerge, proves that this is a reproducible result in this sample. The cause of these differences is not obvious.

It has been suggested that the origin of the ferromagnetic component observed in the magnetisation measurements might be due to one or more moments 'turning over', i.e. reversing their orientation[18]. Since a commensurate modulation appears to be the source of the 'even-ordered' peaks this is the obvious starting point in looking for a magnetic structure that could produce the observed results. Using equation 4.21 the structure factors for different magnetic structures have be investigated for comparison with experimental results. The structure factors F_{hkl} were calculated from the experimental data with appropriate Lorentz and form factor corrections (see §4.4); however, since many of the satellites are made up of several peaks, in some cases accurate estimation of the structure factor is difficult. A definitive solution to the magnetic structures in this compound will require the separation of the commensurate component from the other modulations.

For the commensurate structure repeating over 20 crystal unit cells (therefore incorporating 40 Er sites), peaks at all positions observed experimentally (both 'odd' and 'even' peaks) are easily obtained by reversing the orientation of two moments in each magnetic unit cell, one on the cell corner and one at the cell centre. These two moments can be selected such that an overall moment results. The intensities produced, as well as the net moment over the entire magnetic unit cell, vary greatly depending on which moments are selected. From this approach a good fit to the experimental data can be obtained which has an overall magnetic moment of 0.15μ_B/Er, which is comparable to the 0.3μ_B/Er estimated from the magnetisation measurements by Canfield et al[6]. It also reproduces the reduction in intensity of the

higher order satellites of the SDW observed experimentally, and predicts negligible intensity (smaller than those seen at the 'n-even' positions) at the nuclear site. However, it should be noted that a similar quality match to the experimental data can be obtained by turning the moments to point along the other axis (i.e. from along b to along a). More accurate data regarding the intensities from the commensurate structure are needed to achieve greater certainty about the spin configuration at low temperatures. In addition, this model does not account for the results between 1.8 and 2.3K, where no 'n-even' peaks exist. Since the features in the magnetisation and heat capacity occur at around 2.3K the magnetic structure over this temperature range is obviously important.

Recently, Jensen[19] has considered a mean field model for the ferromagnetic component in ErNi$_2$B$_2$C, and discovered that the reversal of two spins, in the manner described above, is the most stable structure at low temperatures. This mean field model was applied to the data of Choi et al.[18], who do not observe the two steps seen here. This suggests that the simulated structure described above is basically correct for the data obtained below 1.8K in this work. At this stage it is not clear why there are two stages in the development of the 'ferromagnetic component' in this sample, but only one stage in the work of Choi et al.

An interesting additional feature of the transition at $T_{WF1} \sim 2.3$K is the appearance of the rods of intensity along the principal axes, observed by small angle scattering. These rods may be caused by the existence within the magnetic structure of domains, whose boundaries are uncorrelated, resulting in this diffuse scattering. Such domain walls may also be the cause of the increased vortex pinning observed in magnetisation measurements. Although there are regions with slightly different modulations even at higher temperatures, the structural change that produces the extra diffraction peaks below 2.3K may also affect the arrangement or number of the domain walls. The structural transition at 1.8K appears not to affect either the rods or the magnetisation.

The low temperature magnetic behaviour of ErNi$_2$B$_2$C is clearly complicated, and further experimental and theoretical work will be required to unravel all of its properties.

6.5 Magnetic Structure of ErNi$_2$B$_2$C in an Applied Magnetic Field

Investigations into the metamagnetic behaviour of ErNi$_2$B$_2$C were carried out over a series of experiments using the two-axis diffractometer D23 at ILL, with the sample mounted within a cryomagnet. A neutron wavelength of 1.27Å, from a Cu (2 0 0) monochromator, was used with a single ^{3}He detector.

6.5.1 Magnetic Field Applied Parallel to [2 1 0]

Initially, the sample was mounted in the vertical cryomagnet so that the magnetic field could be applied along the crystal [2 1 0] direction. The sample was then cooled to 2K in zero magnetic field where the sample alignment was checked. Figure 6-19 shows the intensity of the (0 0 2) peak as the magnetic field was increased to 4T and back to zero at this temperature. To obtain this data, the diffractometer was set to record the number of counts *at* the (0 0 2) position for regular time intervals as the field was swept up or down at a constant rate. As the field is increased, the first clear transition is at about 1.4T, to a state with an increased ferromagnetic component as indicated by the increased intensity; a second transition occurs at about 2T. Data collected as the field decreases shows that both of these transitions are hysteretic, indicating that they are of first order. In fields below 1T there is some variation of intensity, but no distinct transitions.

The procedure was repeated at other temperatures using a similar method, with the sample cooled in zero field from 12K to the required temperature prior to beginning the field sweeps in each case. As the temperature is increased, both transitions shift to lower fields, and the first transition becomes less distinguishable.
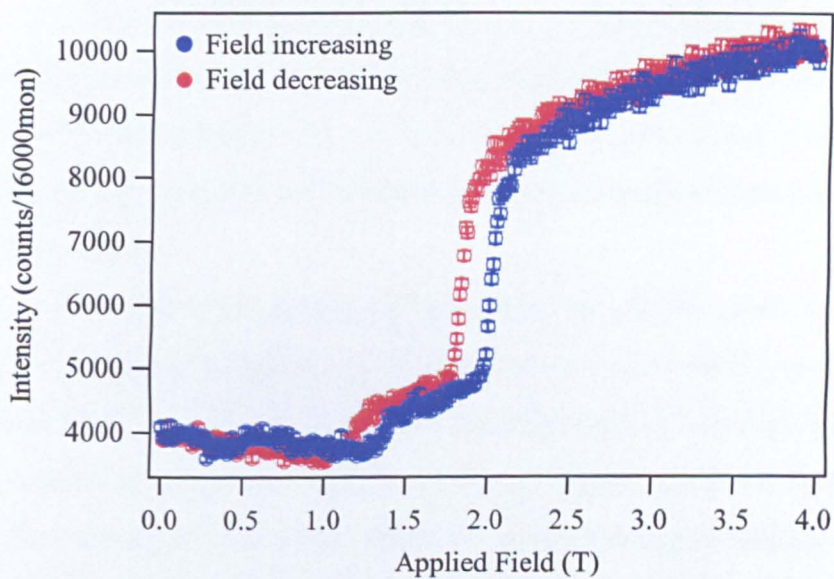
Figure 6-19: Intensity at (0 0 2) with field along [2 1 0] in $ErNi_2B_2C$ at 2K.

The second transition also broadens noticeably. This is illustrated in figure 6-20, which shows data collected at 5.5K, the highest temperature attempted (recall that $T_N = 5.8K$). The intensity is now constant below 1T, with the increase in intensity beginning above 1.2T. This behaviour of the (0 0 2) reflection is consistent with published results for fields applied along [1 0 0] and [1 1 0][16,17].

To obtain information about the behaviour of a fundamental magnetic peak in this orientation with field, again at 2K, the whole peak was scanned in numerous applied field values ranging from zero to 2.3T, above the final transition observed at (0 0 2). The data were collected sequentially in increasing applied field after cooling to 2K in zero field.

The variation of the position of the fundamental magnetic peak with applied field at 2K is shown in figure 6-21. The peak position was obtained by fitting the experimental data to a Gaussian function. In some cases, where there are two or more overlapping peaks (for example, where two phases coexist, as described in more detail below), the data were fitted to a multiple Gaussian function and the position of the *strongest* peak only is shown for clarity. In zero field the peak is very close to ($\overline{0.55}$ 0 2) as expected. Above 0.4T the peak starts to move smoothly away from that position, though this is only a small change. There is a clear transition at 0.75T, where the peak abruptly shifts to around ($\overline{0.571}$ 0 2). This is a more dramatic change, from a modulation that repeats over about 20 crystal unit cells to one repeating over only 14 unit cells. At 1.2T there is a second transition, and the modulation reaches 0.588a* at 1.25T. This modulation appears to exist only over a small field range as by 1.3T the peak has shifted back to ($\overline{0.581}$ 0 2). On further increasing the applied field the peak moves only slightly until yet another transition at 1.7T. The position of the fundamental peak, which is now very similar to its position in the lower field range of 0.75-1.1T, remains effectively constant above 1.75T.
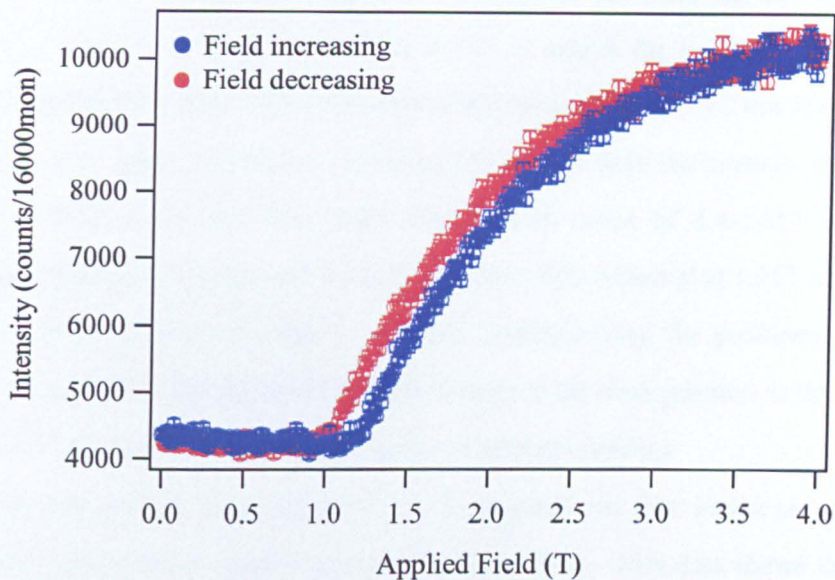
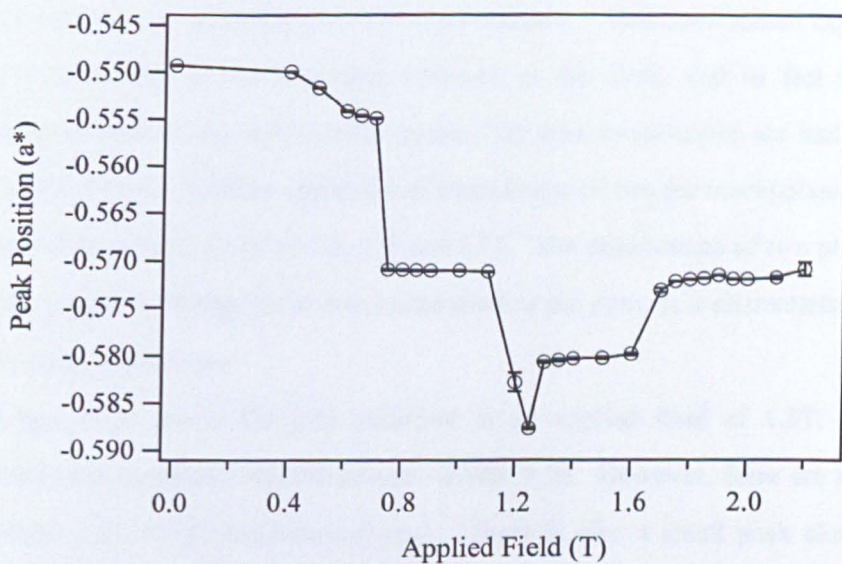Figure 6-20: Intensity at (0 0 2) with field along [2 1 0] in $ErNi_2B_2C$ at 5.5K.

Figure 6-21: Variation of fundamental magnetic peak position with applied field along [2 1 0] at 2K.

Figure 6-22 shows the integrated intensity of the peak as the field is increased. There is a dip in intensity at 0.75T, at which the peak position also changes. The intensity then remains approximately constant up to 1.1T but decreases as the peak shifts again. On further increasing the applied field the intensity reaches about two thirds of its previous values over a field range of 1.4-1.85T before decreasing smoothly to background by 2.2T. Without data collected at 1.65T it is not possible to know if there is a dip in intensity accompanying the positional shift between 1.6 and 1.7T. However, every other change in the peak position as the field is increased is accompanied by a feature in the integrated intensity.

The scan carried out in a field of 0.75T, at which the first abrupt change in fundamental peak position occurs, is shown in figure 6-23. This data shows that at this transition there is coexistence of two modulations. As well as the strong peak corresponding to the new modulation at ($\overline{0.555}$ 0 2), there is a smaller peak remaining from the lower field modulation centred at ($\overline{0.571}$ 0 2). Although the new peak was not present at all at 0.7T, it is much stronger than the old peak at 0.75T, indicating that the new modulation is already dominant. This coexistence explains the origin of the dip in the integrated intensity at this field, and in fact if the integrated intensities of the fundamental peaks from both modulations are included, the dip does not occur. Similar signatures of coexistence of two (or more) phases are also observed in applied fields of 1.2, 1.3 and 1.7T. The coexistence of two phases, rather than a smooth change from one modulation to the next, is a characteristic of first order phase transitions.

Figure 6-24 shows the data collected in an applied field of 1.5T. The fundamental peak is clearly centred around ($\overline{0.580}$ 0 2). However, there are small peak to either side of the fundamental peak. There is also a small peak close to ($\overline{0.550}$ 0 2) in the data collected in 1.25T.

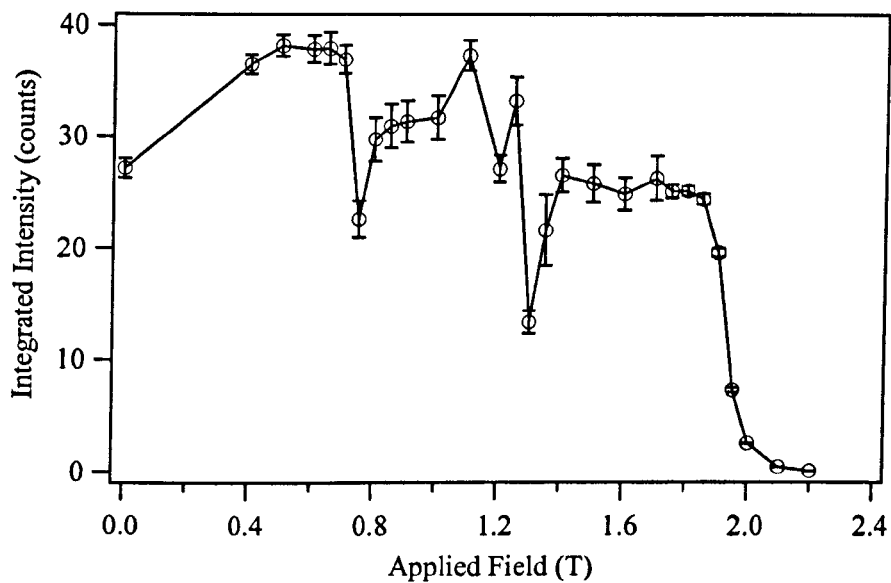The weak peaks to either side of the fundamental peak observed here in the field range 1.4-1.6T were not observed for the other orientations in the previous

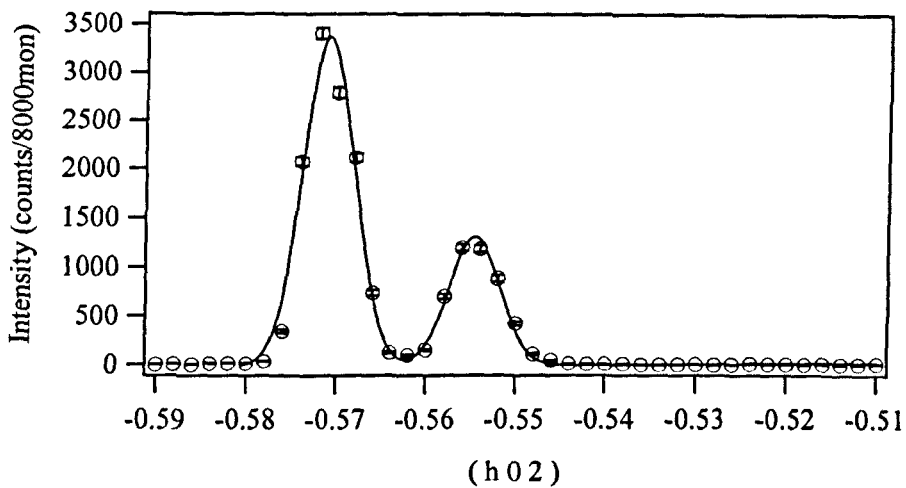Figure 6-22: Integrated intensity of fundamental magnetic peak in ErNi$_2$B$_2$C with field applied along [2 1 0].

Figure 6-23: Q-scan along (h 0 2) in $ErNi_2B_2C$ at 2K; the field of 0.75T is applied along [2 1 0].

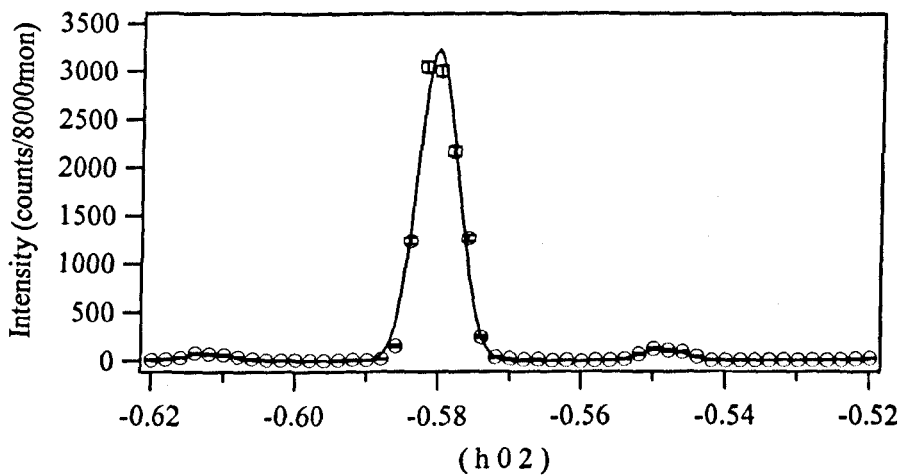Figure 6-24: Q-scan along (h 0 2) at 2K in an applied field of 1.5T.

works,[16,17] although if a narrower scan were used they may have been outside the scope of that scan. These unexpected satellites imply that there are more exotic changes in the number and location of satellites, and therefore in the modulation and 'square-ness' of the distribution of the moments than anticipated. To obtain more extensive information about the behaviour of the other satellites, much longer scans were made in this orientation at intervals of 0.2T up to 1.8T. Although there was not sufficient time to use smaller field intervals, as had been used for the scans of the fundamental peak, these data are adequate for tracing the changes in the other magnetic satellites as a function of applied magnetic field.

Figure 6-25 shows data obtained after cooling the sample to 2K in zero applied field. There is a nuclear peak at (0 0 2) and the fundamental magnetic peak at ($\overline{0.55}$ 0 2). The scale has been selected to show the weaker peaks, but for comparison the maximum of the fundamental peak in this scan is 7500 counts. As is expected in zero field from the previous experiments, there are also third, fifth and seventh order satellites at the appropriate positions. Again, there appears to be a number of modulations with very similar magnitudes (and which must therefore have similar free energies), causing detectable splitting of the higher order satellites. However, based on the data presented in section 6.3, at this temperature and in zero field there should be peaks clearly visible for all (h $\pm$ nq 0 2) where n is an odd integer and all the h are even. This is clearly not the case here, and suggests the sample temperature is actually higher than 2.0K in this experiment.

At 0.4T (figure 6-26) the positions of the peaks are almost identical to the 'zero field' data as might be expected from the detailed examination of the behaviour of the fundamental peak above. However, several new peaks at (h $\pm$ nq 0 2) with n-odd have emerged, as well as some with n-even. In many cases these high odd or even ordered satellites are split, indicating that there are still several modulations, although they must all be close to ($\overline{0.550}$ 0 2). The general arrangement of peaks is very similar to that observed at temperatures below 1.8K on D10 (section 6.3.1),
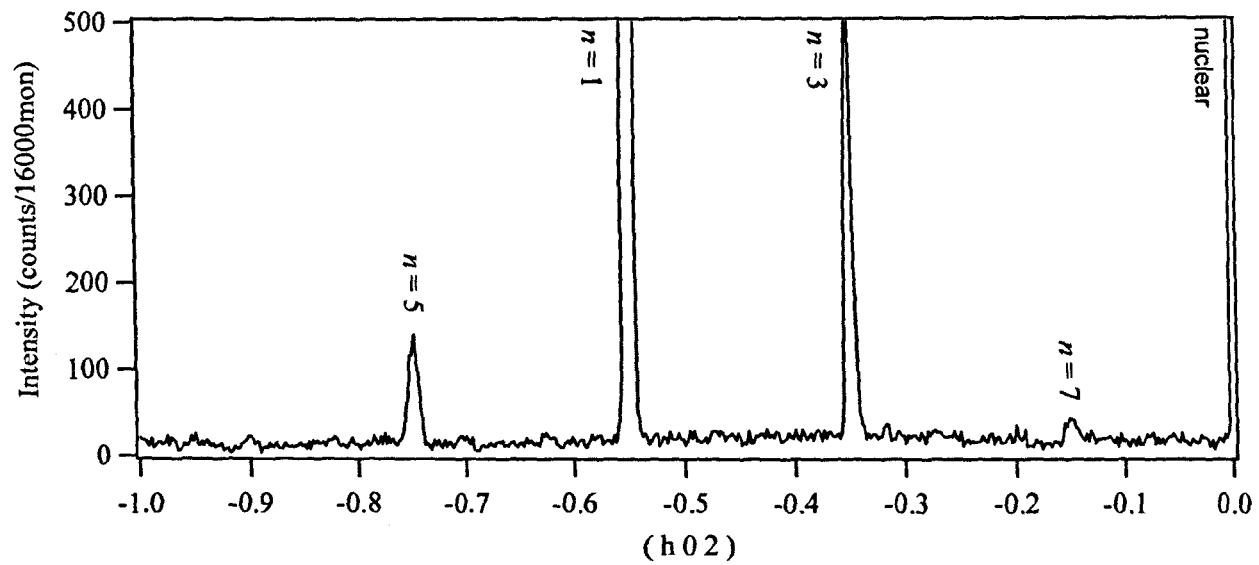
Figure 6-25: Q-scan along (h 0 2) from $ErNi_2B_2C$ at 2K, in (nominally) zero field.

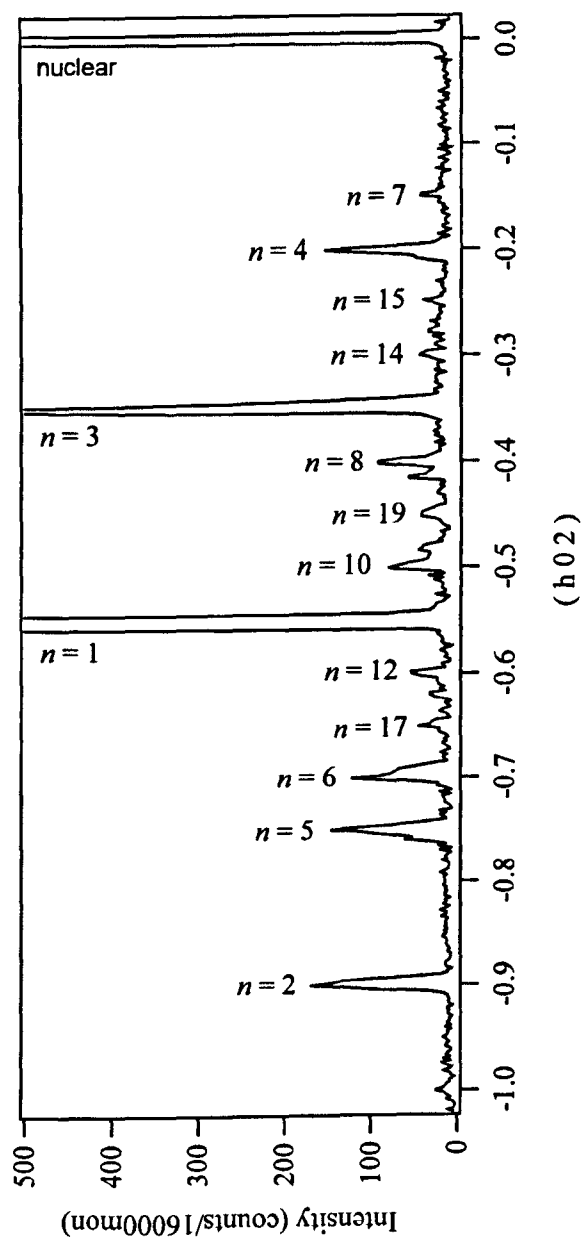Figure 6-26: Q-scan along (h 0 2) from $ErNi_2B_2C$ at 2K, in 0.4T along [2 1 0].

suggesting a broadly similar structure in which the SDWs relating to the slightly different modulations have varying degrees of 'square-ness', as revealed by the different intensities of the higher order harmonics.

The data collected in an applied field of 0.6T is shown in figure 6-27. The fundamental peak has shifted as expected based on the shorter scans, causing noticeable changes in the position of the higher order satellites as well. Again, the splitting of many of the higher order peaks indicates that there are contributions from slightly different modulations. For example, the $n = 5$ peak is split into two; the smaller peak corresponds to the modulation suggested by the fundamental peak, whereas the stronger peak is from a slightly different modulation. However, the small overall change in modulation has also caused a structural change, since the satellites with n-even observed in lower fields have vanished. This would seem reasonable if, as suggested above (section 6.3.1), the n-even satellites relate to a commensurate modulation of 0.550a*. The change in modulation caused by applying 0.6T to the sample removes that commensurate structure, and the n-even peaks are no longer observed.

Data collected in applied fields of 0.8T and 1.0T (not shown) confirm that a first order transition to a new modulation occurs in this field range. Figure 6-23 showed coexistence of two phases involved at 0.75T. The scan of the fundamental peak collected at 0.9T (also not shown) shows a very weak remnant of the lower field phase, indicating that the coexistence of these two phases extends over at least 0.25T. At 0.8T, the longer scan shows that all of the higher order satellites observed at 0.6T remain but have much reduced intensity at 0.8T; the diffraction pattern is dominated by the new modulation of approximately 0.571a*. It has third and fifth order satellites at about ($\overline{0.285}$ 0 2) and ($\overline{0.857}$ 0 2) respectively. At 1.0T only the new modulation exists. The new modulation differs from those observed at lower fields with respect to the higher order satellites: *only* the third and fifth order satellites are observed, where previously several higher orders were detected,
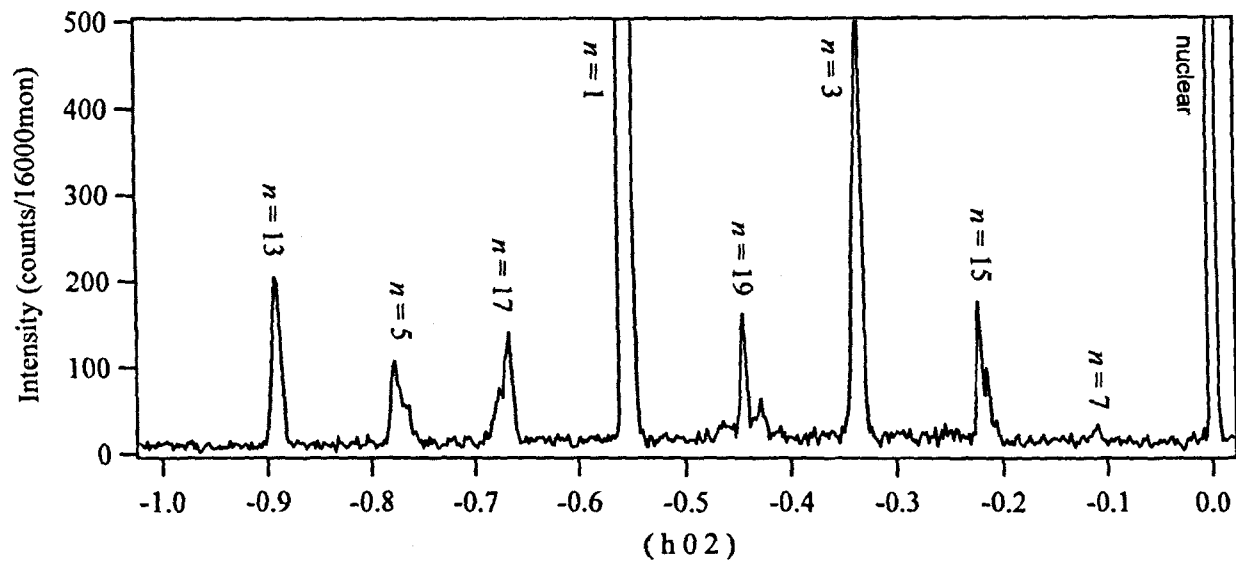
Figure 6-27: Q-scan along (h 0 2) from ErNi$_2$B$_2$C at 2K, in 0.6T applied along [2 1 0].

suggesting a slightly less square modulation in this field. The absence of the very high order satellites makes it difficult to say whether there is truly only one modulation in this phase, since no splitting of peaks is observed for the lower order peaks.

Figure 6-28 shows data collected in an applied field of 1.2T, in which the shorter scans of the fundamental peak revealed extra peaks to either side. This modulation exists only over a small field range of less than 0.1T as shown earlier in figure 6-21. There are very weak remnants of the modulation formed at 1.0T, but also several new peaks such as those at ($\overline{0.12}$ 0 2). The weak peaks at ($\overline{0.24}$ 0 2) and ($\overline{0.94}$ 0 2) are the third and fifth order satellites respectively of a modulation of approximately 0.587a*, for which the fundamental peak provides the data at this field in figure 6-21. The fundamental peaks are surrounded by what appears to be an indistinct group of satellites, as is the strong peak at ($\overline{0.82}$ 0 2); a third modulation must be responsible for these and the other remaining unidentified satellites.

Data obtained at 1.4T is shown in figure 6-29. This is another field in which extra peaks were observed to either side of the fundamental peak in the shorter scans. This data shows three groups, each consisting of a central peak with its own set of clearly resolved satellites surrounding it. This kind of diffraction pattern is similar to that observed from 'superlattice' structures[20], perhaps composed of alternating blocks of two different structures. Looking back at the data collected at 1.2T, the groups of peaks surrounding the strongest satellites are not dissimilar, though much less clear. It is possible that the further increase of the applied field eliminates all other remaining modulations, and allows the superlattice-like structure to become stable and fully formed at 1.4T. Analysis of the peak positions shows that the central peaks of each group do not match with the positions expected for third or fifth order satellites based on the position of the strongest peak at ($\overline{0.579}$ 0 2). This suggests that they are not harmonics, but rather Bragg peaks corresponding to the different magnetic structure that has now developed. For superlattice structures the separation
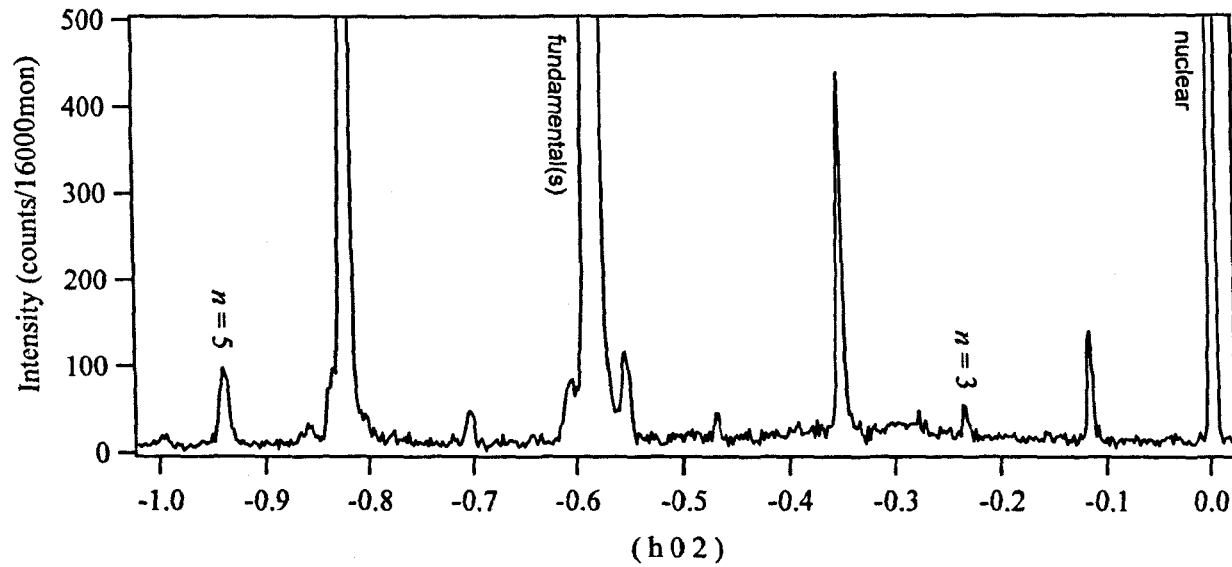
Figure 6-28: Q-scan along (h 0 2) from $ErNi_2B_2C$ at 2K, in 1.2T applied along [2 1 0]

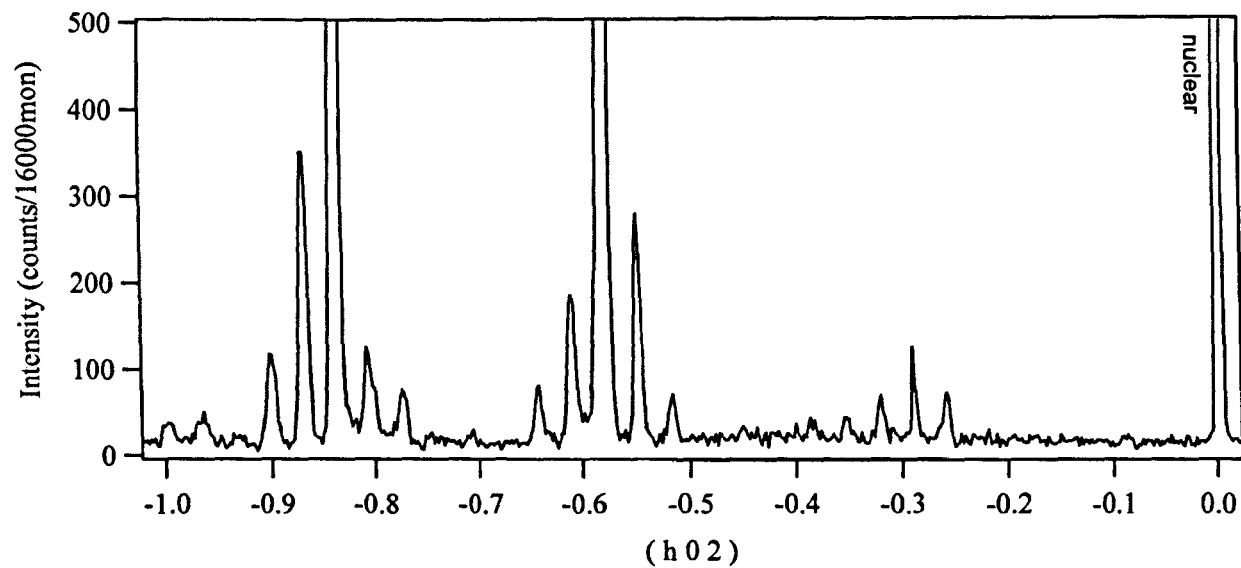The 3rd and 5th order satellites belonging to the strongest fundamental peak are indicated.

Figure 6-29: Q-scan along (h 0 2) from ErNi$_2$B$_2$C at 2K, in 1.4T applied along [2 1 0].

of the superlattice peaks is related to the bilayer repeat length L via[20] $\Delta Q = 2\pi/L$. Analysis of the peak positions for the three groups at observed at 1.4T suggests such repeat lengths of 924(2)Å, 1102(12)Å and 1745(5)Å.

At 1.6T, the situation is very similar to 1.4T, but a peak has re-emerged at the position of the fifth order peak from 1.0T. This suggests that there may be an appropriate fundamental peak for that modulation also present, and indeed there is a shoulder on the principal 'superlattice' peak at the correct position. Therefore it appears that, while the 'superlattice' structure is the sole structure at 1.4T, by 1.6T a second modulation has begun to develop.

As noted previously, the magnitude of the modulation wave-vector at 1.8T (not shown) is effectively the same as it had been at 1.0T. This is borne out in the longer scan carried out in this field, which also shows the 'superlattice' type peaks have almost entirely vanished. In fact the diffraction pattern is very similar to that observed at 1.0T, if the remnants of the previous structure are ignored, except that the relative intensities of the 'third' and 'fifth' order satellites are reversed from what is expected. Although their positions are close to those expected based on the strongest peak, it appears likely that these are not higher order satellites but are caused by different structures as already suggested at 1.4T. On further increasing the applied field, it has been shown (above) that the strongest magnetic peak gradually reduces in intensity as the (0 0 2) peak shows a large increase in intensity signalling the development of the saturated paramagnetic phase, and although no data regarding the remaining magnetic peaks were collected they should also die out by around 2T.

All of the long scans collected in this orientation at 2K are summarised in the contour plot shown in figure 6-30, showing clearly the movement of the fundamental peak as well as the changes in the positions and number of satellites as the magnetic field is increased.

The work described in this section, carried out with the magnetic field applied along the [2 1 0] direction, has revealed a richer and more complicated sequence of
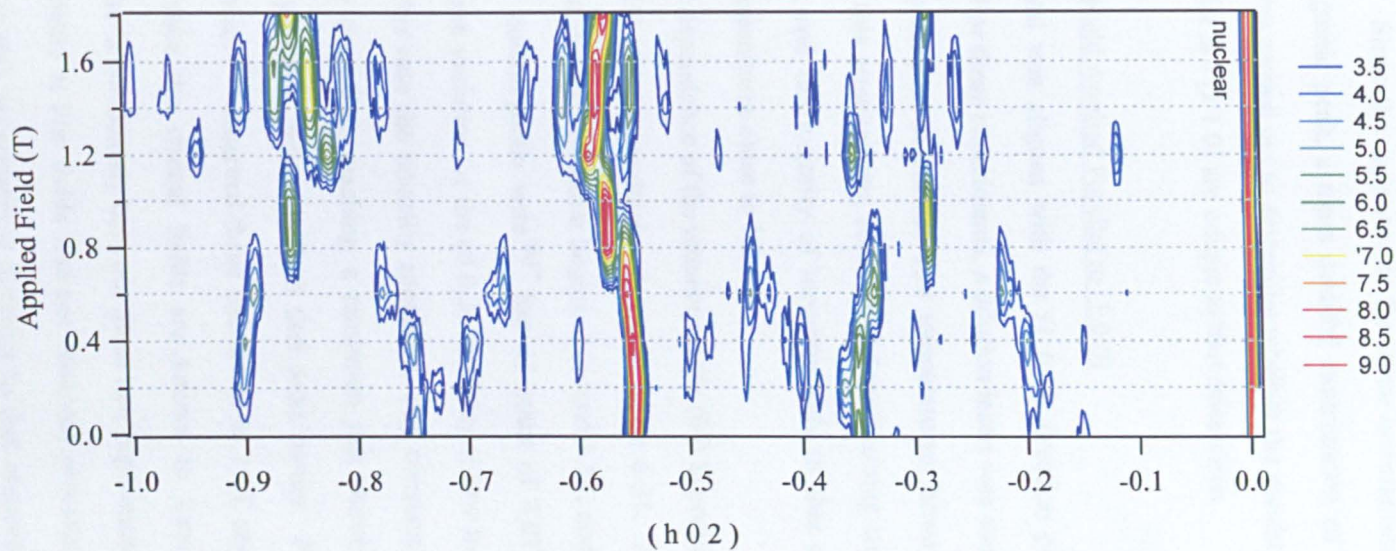
Figure 6-30: Contour plot showing all Q-scans collected from $ErNi_2B_2C$ as a function of applied field along [2 1 0]. The intensity scale is logarithmic. The dotted horizontal lines indicate fields at which data were collected.

transitions in response to the field than was reported for fields applied along [1 0 0] and [1 1 0][16,17]. Since the experiments for those orientations concentrated on the fundamental magnetic peak, a more detailed examination of the behaviour of the other satellites was carried out to determine whether the number and character of the transitions seen for B // [2 1 0] are unique to that orientation.

6.5.2 Magnetic Field Applied Parallel to [1 0 0]

The crystal was aligned with the [1 0 0] direction parallel to the applied magnetic field. For these experiments, a dilution insert was used in conjunction with the standard cryomagnet to provide low temperatures; however, due to technical difficulties with this arrangement, reaching and maintaining any chosen temperature was impossible, and the majority of measurements in this orientation had to be carried out at temperatures close to 1K.

The field dependence of the intensity at the (0 0 2) position was measured at a temperature of 1K and the results are shown in figure 6-31. As the applied field is increased the first distinct transition begins at around 1.3T, and the second transition to the saturated paramagnetic state[16,17] has an onset of 2.0T in these conditions. There is also some variation of the (0 0 2) intensity at low fields, as there was for B // [2 1 0]; in this case the intensity appears to stay constant to about 0.3T, above which it slowly decreases, reaching a minimum just above 1.0T. All of these features show hysteresis, indicating their first order nature. For this orientation, at 2K, Campbell et al.[16,17] observed these transitions at 1.1T and 1.9T for a different nuclear peak; since the critical fields are known to increase with decreasing temperature, there is consistency between these two experiments in this regard. The variation of intensity at low fields was not observed previously. Finally, the high field behaviour in this experiment is different to that observed either for the other orientations investigated for this sample, and the previous work. In every other case the intensity continues to increase to the highest fields investigated; the

magnetisation, as shown in figure 6-4. In this orientation, the intensity ... this orientation, in this orientation, the intensity of the (0 0 2) peak ... after reaching a maximum at around 2.0-2.4T. The measurement was therefore also carried out here at 1.7K, with similar results. On decreasing the applied field, the behaviour is similar to that observed in the other orientations ...
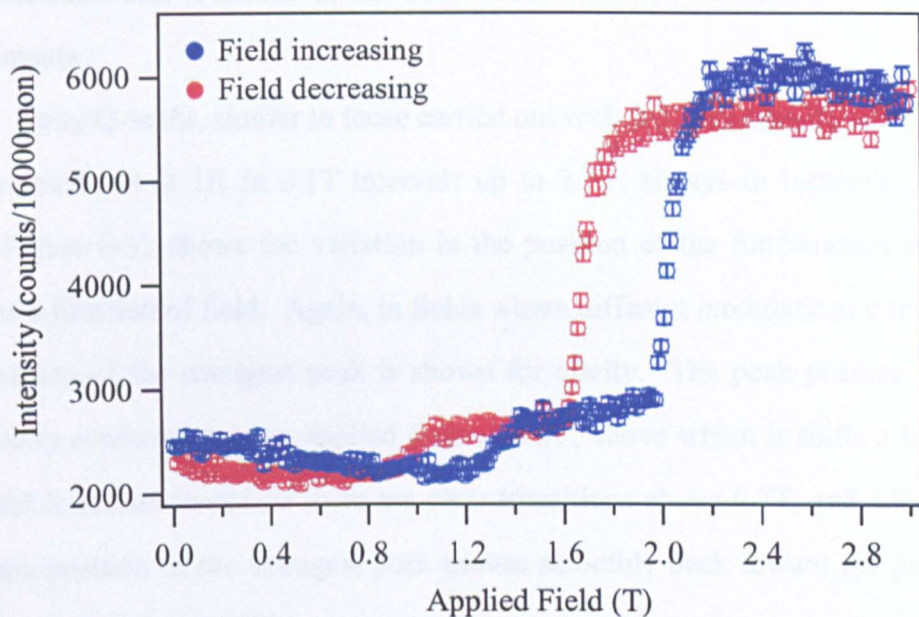

Figure 6-31: Intensity at (0 0 2) in $ErNi_2B_2C$ at 1K, with the field applied along [1 0 0].

magnetisation, as shown in figure 6-5, is also increasing in this range. However, for this orientation, in this experiment, the intensity of the (0 0 2) peak decreases slightly after reaching a maximum at around 2.3-2.4T. The measurement was repeated at 1K, and also carried out later at 1.7K, with similar results. On decreasing the applied field, the behaviour is similar to that observed in the other orientations and previous experiments.

Long Q-scans, similar to those carried out with the field applied along [2 1 0], were carried out at 1K in 0.1T intervals up to 2.1T, always in increasing applied field. Figure 6-32 shows the variation in the position of the fundamental magnetic peak as a function of field. Again, in fields where different modulations coexist only the position of the strongest peak is shown for clarity. The peak position remains essentially constant up to an applied field of 0.5T, above which it shifts a little. As the field is further increased there are clear transitions above 0.7T, and 1.0T; above 1.3T the position of the strongest peak moves smoothly back toward the position it had between 0.8T and 1.0T.

The integrated intensities of these peaks are shown in figure 6-33. There is a dip in intensity at 0.8T where the first major shift in peak position takes place. On further increasing the applied field the intensity drops sharply above 1.0T, corresponding to the second transition suggested by the change in peak position shown in figure 6-32. At 1.3T it recovers slightly, before falling smoothly as the field is increased to 1.6T. Above 1.6T the intensity increases again before finally falling away to zero above 1.8T when the saturated paramagnetic state develops.

In small applied fields, up to 0.4T, the diffraction profiles in this orientation are similar to those obtained with B // [2 1 0]. As the field is increased, the high n-odd satellites and n-even satellites increase in intensity. At 0.4T the data is very similar to figure 6-26, where the same field is applied along [2 1 0], and again the higher order satellites show splitting indicating that in fact there are several modulations very close to each other in magnitude.
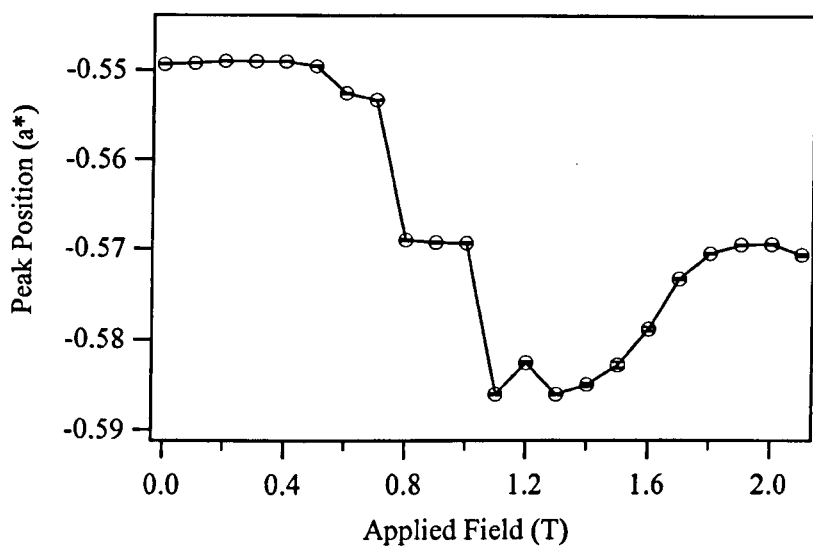
Figure 6-32: Variation of position of strongest fundamental magnetic peak with applied field along [1 0 0] in ErNi$_2$B$_2$C.
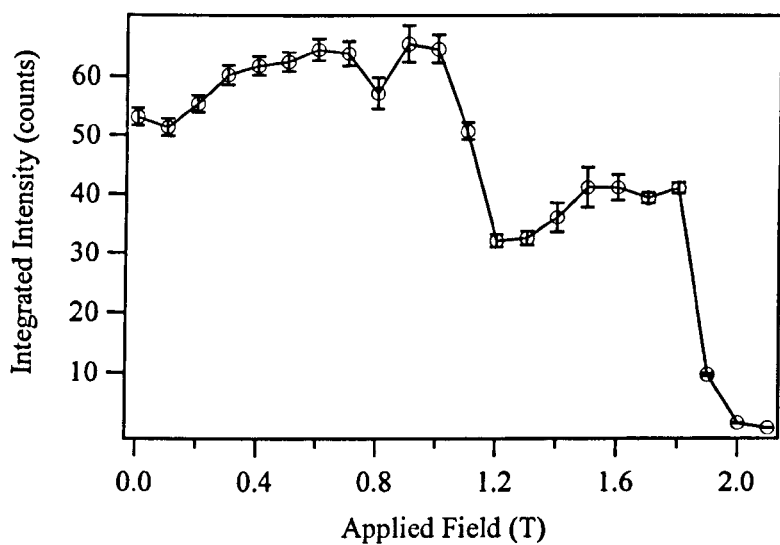

Figure 6-33: Integrated intensity of strongest fundamental magnetic peak with applied field along [1 0 0].

Figure 6-34 shows data collected in an applied field of 0.6T. At this field the first, relatively small, change in the magnitude of the modulation occurs (figure 6-32), but in fact there is still some remnant of the previous modulations which in this figure is most clearly demonstrated by the shoulder on the third order satellite. By 0.7T (not shown) these remnants have disappeared, leaving only the new modulation. With the new modulation, only n-odd satellites are formed, and this is very similar to the structure observed between 0.4T and 0.7T with B // [2 1 0].

At 0.8T the new modulation with q ~ 0.57a* is dominant, though there are still weak peaks from the structure observed at 0.7T. This new structure shows only first, third and fifth order satellites; again, this structure was observed in the previous orientation in fields of 0.8-1.1T.

In fields of 1.1T and 1.2T there are again two modulations. One of these is the modulation from 1.0T in both cases. At 1.1T, the new modulation is dominant, but at 1.2T (figure 6-35) the fundamental peak of this modulation shifts slightly, and in this field the intensities of the peaks from the two modulations are comparable, with the new modulation only slightly stronger. The 3rd and 5th order satellites from the lower field modulation are indicated, but the other weak peaks do not correspond to the new modulation and must have a different origin.

By 1.3T (figure 6-36) the modulation that had persisted from 0.8T eventually disappears and now a structure akin to the 'superlattice'-type observed in the previous orientation is formed. Two principal peaks are accompanied by side-bands, though in this orientation there are only two of these, whereas for B // [2 1 0] there were four. Since the envelope determining the intensities of the side-bands is related to the structure factor of the individual bilayer[20], this suggests that slightly different structures are formed in the two different orientations. In this case the positions of the side-bands suggest bilayer repeat lengths of 938(2)Å and 805(2)Å. As the field is further increased, other peaks appear superimposed on this structure, and the "superlattice" peaks become weaker. Finally, at 1.9T only three peaks remain, and just as for B // [2 1 0], their locations are similar to those observed at lower fields (0.9

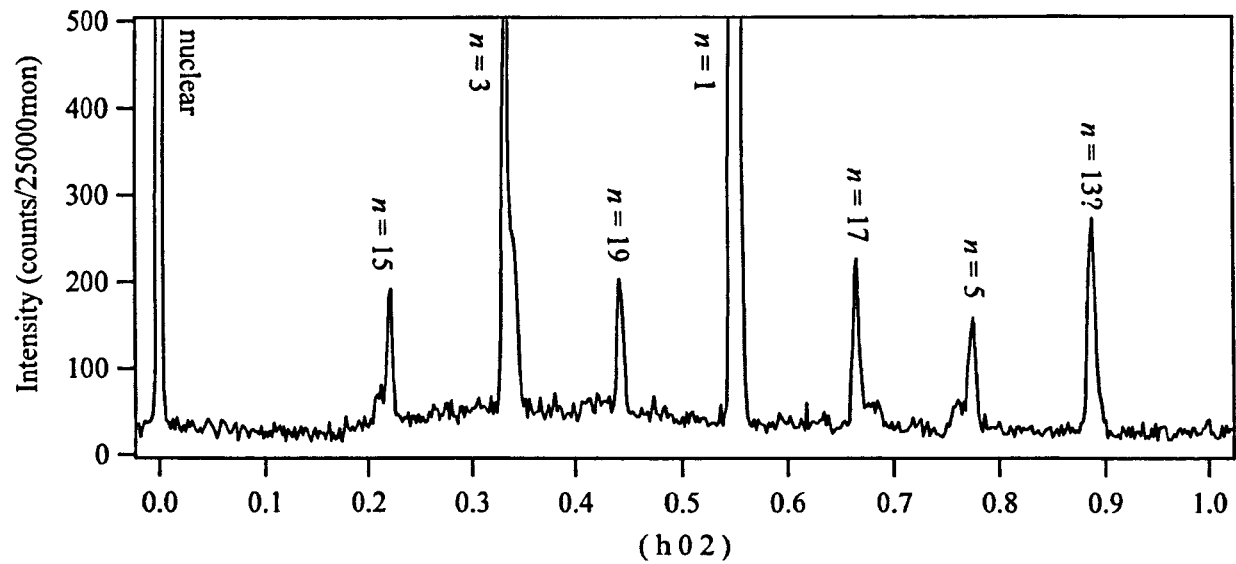Figure 6-34: Q-scan along (h 0 2) from $ErNi_2B_2C$ at 1K, in 0.6T applied along [1 0 0].

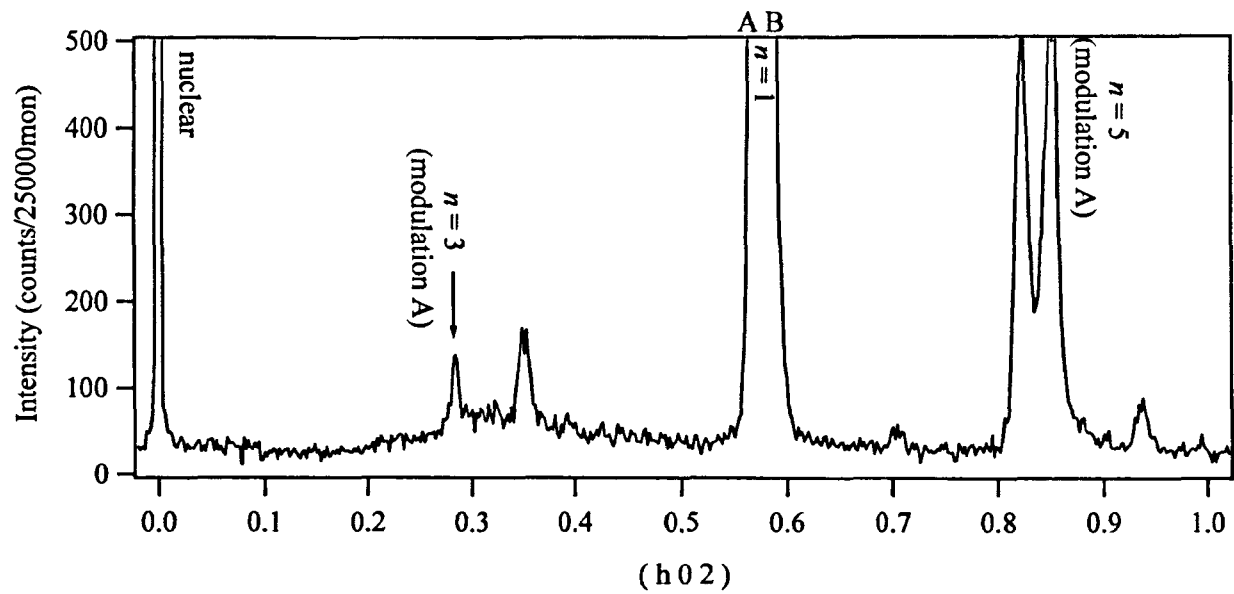Figure 6-35: Q-scan along (h 0 2) from ErNi$_2$B$_2$C at 1K, in 1.2T applied along [1 0 0].
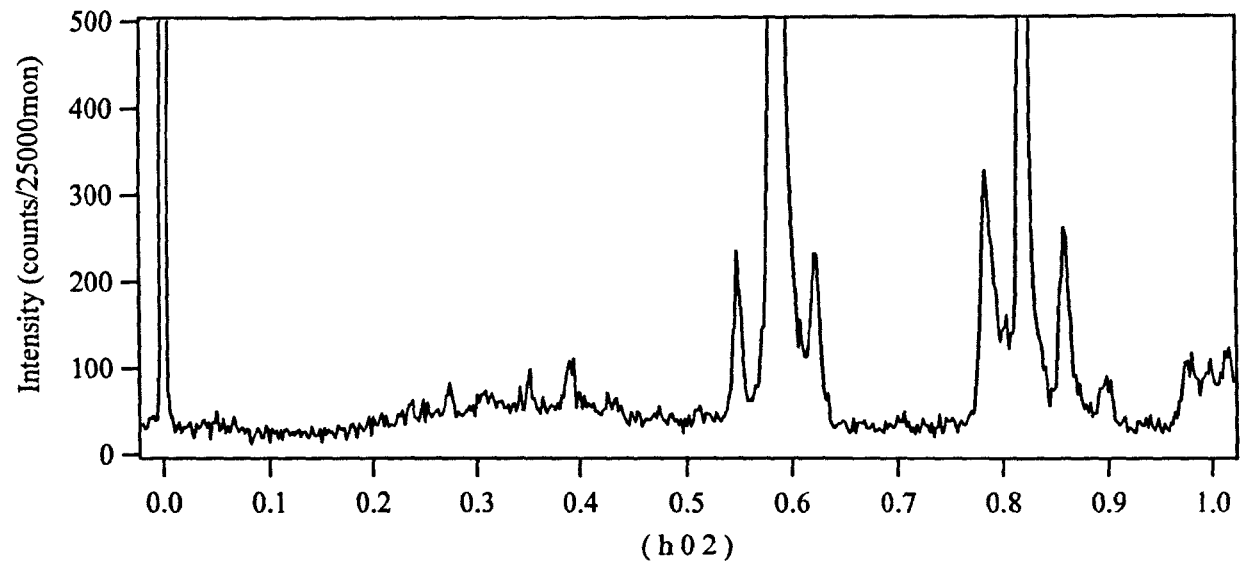
Figure 6-36: Q-scan along (h 0 2) from ErNi$_2$B$_2$C at 1K, in 1.3T applied along [1 0 0].

- 1.0T in this case) but the relative intensities of the 'third' and 'fifth' order satellites are reversed from what is expected, so they may not be harmonics but derive instead from a structural change. These peaks grow weaker as the field continues to increase, finally disappearing as the saturated paramagnetic state is approached.

The data obtained with B // [1 0 0] are summarised in the contour plot shown in figure 6-37. In form, the behaviour in this orientation at 1K is very similar to that observed when B // [2 1 0] at 2K, with variations in the details of exactly where the critical fields lie as would be expected for different orientations and temperatures. It was possible to carry out a few measurements at 1.7K, much closer in temperature to the data obtained with fields applied along [2 1 0]. Although there was only time to carry out a few Q-scans, at those fields investigated the structures were the same as above, including the superlattice-like structure that was observed in 1.4T and 1.6T at 1.7K.

6.5.3 Magnetic Field Applied Parallel to [1 1 0]

Finally, the crystal was aligned so that the [1 1 0] direction was parallel to the applied field. Initially, the intensity at the (0 0 2) nuclear peak position was measured at about 200mK in increasing and decreasing applied fields as before. Figure 6-38 shows that in this orientation there are two distinct transitions which begin at 1.7T and 2T in increasing field. Both transitions are hysteretic as expected based on the behaviour observed in the other two orientations.

Extended Q-scans were carried out in the same manner as for the other two orientations. For these measurements the temperature was around 130mK. Figure 6-39 shows the position of the fundamental magnetic peak as the magnetic field is increased. There is a single transition between 1.0 and 1.2T where the position of the strongest fundamental peak changes. The integrated intensity of this fundamental peak is shown in figure 6-40. The change in peak position between 1.0 and 1.2T is accompanied by a decrease in intensity. There is then another decrease above 1.5T, which is not accompanied by a change in modulation based on the information in

Figure 6-37: Contour plot showing all Q-scans collected from ErNi$_2$B$_2$C as a function of applied field along [1 0 0]. The intensity scale is logarithmic. In this case the dotted horizontal lines emphasise the number and locations of magnetic transitions.
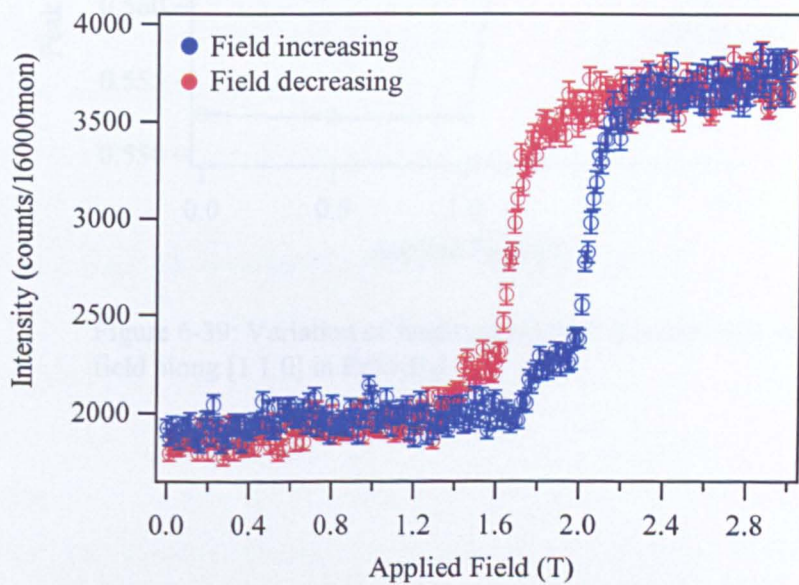
Figure 6-38: Intensity at (0 0 2) in $ErNi_2B_2C$ at 130mK, with the field applied along [1 1 0].
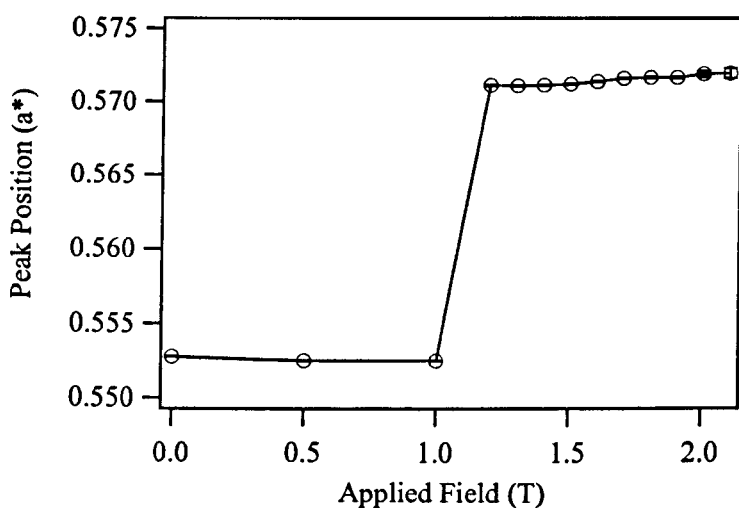
Figure 6-39: Variation of fundamental peak position with applied field along [1 1 0] in $ErNi_2B_2C$
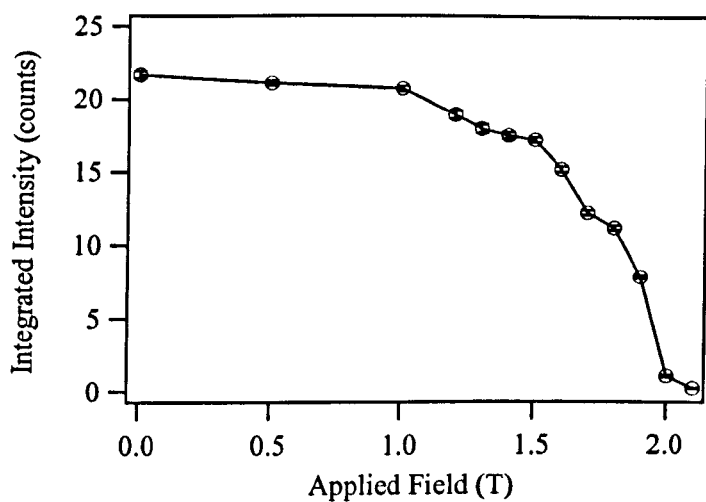
Figure 6-40: Integrated intensity of fundamental magnetic peak with field applied along [1 1 0].

figure 6-39, and a third above 1.8T as the transition to the saturated paramagnetic state begins.

The data collected in this orientation are summarised in the contour plot shown in figure 6-41. It is clear that the behaviour for the field along [1 1 0] is far simpler than for the other two orientations. In low fields, the data are very similar to both of the other orientations, consisting of first, third...etc order harmonics, and some higher order odd-order and even-order peaks that gain in intensity as the field is increased. The change in position of the fundamental magnetic peak is accompanied by changes in the positions of the third and fifth order satellites as would be expected. At fields of 1.2T and above there are no peaks except for the 1st, 3rd and 5th order magnetic satellites, in contrast to the data collected in similar fields in the other orientations. There is no evidence of any superlattice-type structure in this case.

One feature unique to this orientation is a peak at (1 0 2) which emerges in high fields. The integrated intensity of this peak as the field is applied is shown in figure 6-42. The intensity of this peak increases sharply above 1.8T. No peak at this position was observed for fields applied along [1 0 0]; such a high field was not reached for fields along [2 1 0]. The intensity of the peak is far too large to be due to $\lambda/2$ contamination from the (2 0 4) peak, which can be shown from the instrument specification and data collected on all nuclear peaks for structure refinement purposes during previous experiments to be a very weak reflection. Therefore this peak appears to be magnetic in origin. The magnetisation measurements of Canfield et al.[15] suggested that in this orientation there is a transition at about 3T, a considerably higher field than that at which the saturated paramagnetic state is formed in the other two directions; if this peak at (1 0 2) is related to an intermediate magnetic state further data at higher fields will be needed to establish if it disappears above 3T leaving the saturated paramagnetic state only in this orientation. No
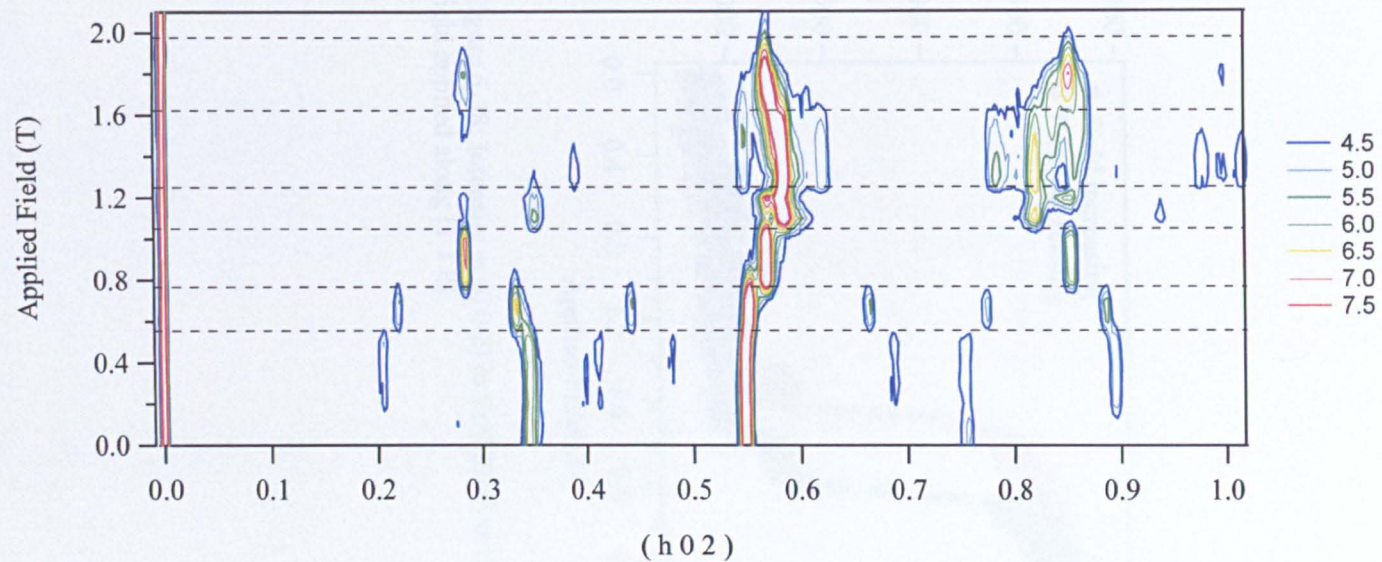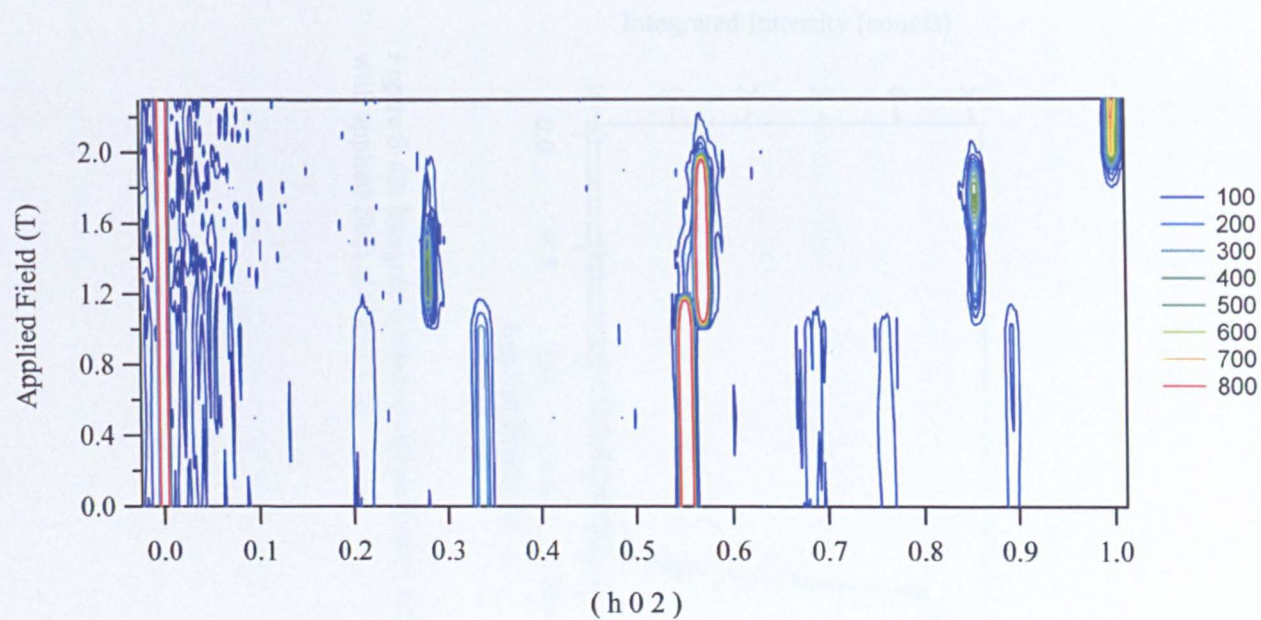
Figure 6-41: Contour plot showing all Q-scans collected from ErNi$_2$B$_2$C as a function of applied field along [1 1 0]. The intensity scale is linear. The apparent intensity around the nuclear peak (0 0 2) is due to a high background in this part of the scan.

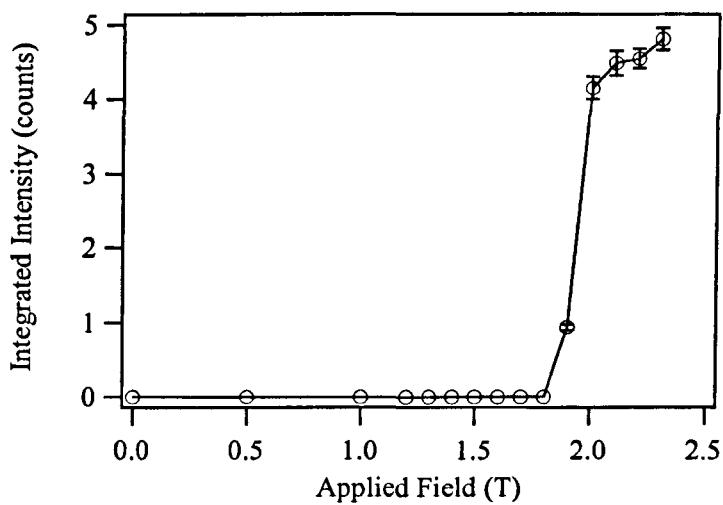Figure 6-42: Integrated intensity of peak at (1 0 2) in $ErNi_2B_2C$ with applied field along [1 1 0]

evidence for this state or an additional transition was observed in the previous neutron scattering experiments[16,17].

A characteristic that this orientation does have in common with the other two is the reversal of the relative intensities of the 'third' and 'fifth' order satellites at high fields. Since this orientation is much simpler than the previous two it is easy to follow the behaviour of these peaks. The integrated intensities of these satellites as a function of applied field are shown in figure 6-43. Both peaks show a slight decrease in intensity initially until the change in modulation occurs above 1.0T. At this transition both satellites become much stronger indicating that the modulation is squarer than was the case in low fields. Above 1.5T, where there is a decrease in the intensity of the fundamental peak, the intensity of the 'third order' satellite decreases rapidly while that of the 'fifth order' satellite increases so that their relative intensities are reversed. Above 1.8T the intensities of both peaks decrease as expected at the final transition. Since there is a transition observed at 1.7T in the intensity of the nuclear (0 0 2) peak, the reversal of these intensities may be related to the same structural change that causes the increase in the intensity of the (0 0 2) reflection.

6.6 Discussion - Transitions and Structures in a Magnetic Field

These experiments have shown that the magnetic phase diagram of ErNi$_2$B$_2$C is far more complicated than previously known. Given the complexity observed in some orientations it is helpful to summarise the results obtained in this section.

Originally, only the completion of the orientational phase diagram was envisaged, for which relatively simple investigations with B // [2 1 0] should have been required. However, by examining not just the fundamental magnetic peak but also the satellites this work has shown that the magnetic behaviour of this material is more intricate than previously thought. The magnetic properties of ErNi$_2$B$_2$C in a magnetic field applied along either [1 0 0] or [1 1 0] were investigated in more detail
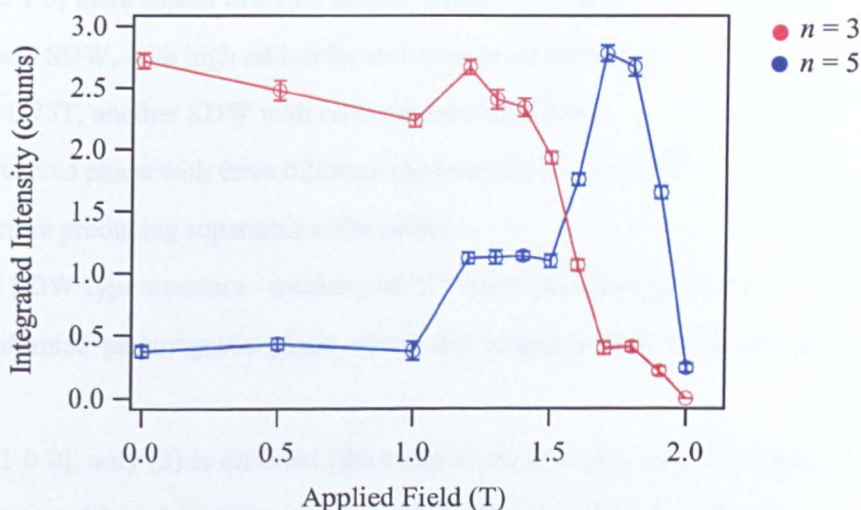
Figure 6-43: Integrated intensities of the 3rd and 5th order satellites with applied field along [1 1 0].

than in prior experiments[16,17] in response to the unexpectedly complicated structures revealed when B // [2 1 0], particularly in the region 1.0-1.5T where the superconducting upper critical field B$_{C2}$(T) occurs.

For both B // [2 1 0] and [1 0 0] there are more transitions than had been estimated from previous neutron scattering experiments and magnetisation results. For B // [2 1 0] there appear to be six distinct phases; these are

1. Low field SDW, with high odd-order and even-order satellites;

2. Above 0.75T, another SDW with no even-order satellites;

3. A short-lived phase with three different modulations at 1.2-1.25T;

4. A structure producing superlattice-like peaks;

5. A final SDW-type structure - intensity of '5th' order peak stronger than '3rd';

6. The saturated paramagnetic phase where the magnetic field holds all moments parallel.

For B // [1 0 0], only (3) is different (the exact fields at which transitions occur also vary as expected based on magnetisation measurements), though as the structure is changing rapidly with field, and there was not time to collect data at smaller intervals, it is impossible to be certain. The broad similarity between these two orientations is not surprising considering their magnetisations are also similar (figure 6-5). The magnetisation for B // [1 1 0] is noticeably different, and the neutron data presented here shows that in fact this orientation is much less rich. For all orientations, each transition was of first order as shown by either hysteresis or coexistence of phases (depending on the type of measurement). The gradual increase of a new phase at the expense of the previous one suggests some sort of seeding of the new phase, and since it has been shown that there are generally several very similar modulations present, presumably in the form of domains, the transition may also be affected by the presence of the domain boundaries.

For all orientations, the low field behaviour is similar. In zero field there are fewer obvious high-order satellites than the zero-field data presented in §6.3.1. In

that experiment strong peaks had appeared for all n-odd by 2K. For B $//$ [1 0 0] and [1 1 0] all of the n-even peaks should be observed in zero field since the temperature is well below 1.8K, the temperature at which these peaks emerged on D10. Since the experiments on D23 used a cryomagnet, this suggests that the magnetic response of the sample in 'zero field' is very sensitive to any remanent magnetic field that may have been trapped in the superconducting magnet used here. It is also interesting that in §6.3.2, the n-even satellite is observed using the SANS instrument, and it has the same temperature dependence as seen on D10; in that case the magnetic field was provided by an electromagnet, and could only be applied along [0 0 1]. If the remanent field on D23 is responsible for the suppression of these peaks, then in the SANS experiment either any remanent field was too weak to affect the magnetic properties, or such a field applied out of the plane has no impact. Originally, one of the aims of these experiments was to examine the behaviour of the ferromagnetic component, examined in true zero field on D10 above, when a magnetic field is applied. These results clearly suggest that a great deal more work is required to understand the low field magnetic behaviour in a material whose properties appear to be highly sensitive to the preparation of the magnetic state.

The most complicated behaviour occurs over the 1.0-1.5T range for B $//$ [1 0 0] and [2 1 0]. Both orientations show satellites reminiscent of those observed from superlattices. The structure appears to be more stable when B $//$ [2 1 0], since the structure exists alone over a range of fields. When B $//$ [1 0 0] the peaks are less clear, and a new structure emerges to coexist with the superlattice structure with only a small further increase in field. It is important to understand the magnetic properties in this region as the superconducting upper critical field is also in the vicinity at these temperatures; for example, Bud'ko et $al.$[21] report $B_{C2} \sim 1.4$T for B $//$ [1 0 0], and 1.5T for B $//$ [1 1 0] at 2K. However, since no superlattice-like structure is observed for B $//$ [1 1 0], it does not appear to reduce B_{C2}.

The development of a superlattice-like structure is not the only feature in this field range. In all orientations, above a certain field, the 'fifth' order satellite becomes much stronger than the 'third' order satellite. For B // [1 0 0] and [2 1 0] this first occurs at fields just below the formation of the superlattice structure. In all three orientations it is followed at slightly higher fields by the first transition observed in the intensity of the (0 0 2) nuclear peak, signifying the formation of a state with an increased ferromagnetic component. These states are formed, for each orientation, at fields just below where B$_{C2}$ is expected. This suggests that there may be a correlation between the formation of the state with increased ferromagnetic component, which is accompanied by the reversal of the third and fifth order satellite intensities, and the destruction of superconductivity. Whether or not this is the case, it is impossible at this stage to say whether the superlattice-type structures have any impact, although in a layered structure, where numerous domain boundaries will exist, it is possible that vortex pinning will be affected.

One unexpected feature of the data is the apparent *decrease* in intensity in high (but increasing) fields at the (0 0 2) position observed for B // [1 0 0]. This has not been observed either in previous magnetisation or neutron experiments or here in the other orientations. It may be due to some sort of shift in the crystal position, in which case if the whole peak were scanned as a function of field this odd behaviour would not be observed.

The previous work, with fields applied along [1 0 0] and [1 1 0][16,17] was able to trace the general shape of the phase diagram with respect to the different different structures. This involved following the position and intensity of the fundamental magnetic peak, and the intensity of a nuclear peak. This work has shown that these two on their own do not provide an adequate description of the magnetic behaviour of ErNi$_2$B$_2$C, particularly for B // [1 0 0] and [2 1 0]. It would be a very time-consuming process to attempt to follow the critical fields of so many transitions as the temperature is increased, but this would be interesting especially for the

complicated behaviour that occurs in the vicinity of B$_{C2}$ at the temperatures investigated here. If the critical fields of the relevant magnetic transitions follow the behaviour of B$_{C2}$ with temperature then a link between the two might more confidently be made, as their coincidence at only one temperature (though admittedly for all three orientations) provides no more than conjecture at this point.

It is unfortunate that problems with the equipment during these experiments meant that complete sets of data could not be obtained at the same temperature for all three orientations. This would have at least provided a complete picture of the effect of orientation at, say, 2K for a detailed comparison with upper critical field data. However, since all available evidence shows that the critical fields have fairly slow temperature dependences at low temperatures, it is unlikely that there is a great deal of difference between 1K and 2K, and this would only be detectable if data were collected at much smaller field intervals than time allowed in these experiments.

It should be noted that no transitions were detected in the region of 100mT for any orientation. Such a transition was suggested to be responsible for the shoulder in the hysteresis[6] shown in figure 6-3. If there is no magnetic transition in this field range the source of the increased pinning remains unsolved. As will be shown in §7.3, no increase in disorder of the vortex lattice is observed at low temperatures in this sample for fields applied along *c*; it may be that a similar examination of the VL for fields applied within the *ab* plane will provide further information.

A complete understanding of the magnetic behaviour of this material is required if the relationship between the magnetism and superconductivity is to be fully resolved. This work has shown that, at low temperatures at least, this magnetic behaviour is very complicated, and since no theoretical explanation for the features observed here, particularly for B // [1 0 0] or [2 1 0], exists at this time, a better theoretical understanding is certainly needed.

In this chapter the magnetic properties of ErNi$_2$B$_2$C have been investigated both with and without the application of a magnetic field. In zero field, changes in the magnetic structure have been observed at both 2.3K, where increased vortex pinning associated with the development of a ferromagnetic component begins, and at 1.8K. This two-step process has not been observed elsewhere. Although a model for the structure observed below 1.8K has been suggested, this does not yet account for the behaviour seen here between 1.8 and 2.3K. The metamagnetic behaviour, in response to an applied field, has proved to be far more complex than previously believed, as shown by the number of transitions and variety of magnetic structures indicated by the changes in the modulation wave-vector of the SDW and of the number and intensity of satellites. The behaviour is most intriguing for fields applied along [1 0 0] and [2 1 0]; in these directions the structures include one of a super-lattice-like nature. The behaviour for fields along [1 1 0] is far simpler, and does not include the superlattice structure.

References

[1]   S.K. Sinha *et al.*, Phys. Rev. B **51** No. 1 p681 (1995)

[2]   J. Zarestky *et al.*, Phys. Rev. B **51** No. 1 p678 (1995)

[3]   C. Detlefs *et al.*, Phys. Rev. B **56** No. 13 p7843 (1997)

[4]   C. Detlefs *et al.*, Europhysics Letts. **47** No. 3 p352 (1999)

[5]   J.W. Lynn *et al.*, Phys. Rev. B **55** No. 10 p6584 (1997)

[6]   P.C. Canfield *et al.*, Physica C **262** p249 (1996)

[7]   B.K. Cho *et al.*, Phys. Rev. B **52** No 5 p3684 (1995)

[8]   P. Dervenegas *et al.*, Phys. Rev. B **53** No 13 p8506 (1996)

[9]   B.K. Cho *et al.*, Phys. Rev. B **53** No 13 p8499 (1996)

[10]   J.W. Lynn *et al.*, Phys. Rev. B **55** No 10 p6584 (1997)

[11]   P.L. Gammel *et al.*, Phys. Rev. Letts. **84** No 11 p2497 (2000)

[12]   H. Kawano *et al.*, J. Phys. Chem. Solids **60** p1053 (1999)

[13]   H. Kawano-Furukawa in *Rare Earth Transition Metal Borocarbides (Nitrides) – Superconducting, Magnetic and Normal State Properties* p223 (Kluwer Academic Publishers 2001)

[14]   R. Szymczak *et al.*, Physica C **254** p124 (1995)

[15]   P.C. Canfield *et al.*, J. Alloys Compd. **262/263** p169 (1997)

[16]   A.J. Campbell, PhD Thesis (1999)

[17]   A.J. Campbell *et al.*, S.S.Comms **115** p213 (2000)

[18]   S.M. Choi *et al.*, Phys. Rev. Letts. **87** No 10 Art. 107001 (2001)

[19]   J. Jensen, Phys. Rev. B **65** No. 14 Art 140514R (2002)

[20]   D.A. Jehan *et al.*, Phys. Rev. B **48** No. 8 p5594 (1993)

[21]   S.L. Bud'ko & P.C. Canfield, Phys. Rev. B **61** No. 22 p14932 (2000)

Chapter 7

The Vortex Lattice in ErNi$_2$B$_2$C

7.1 Introduction

ErNi$_2$B$_2$C is a superconductor below 10.5K and orders magnetically below T_N = 5.8K. Previous work on the vortex lattice (VL) in this material[1,2] revealed a rhombic (distorted hexagonal) lattice in low magnetic fields with a field driven transition to a lattice with square symmetry. The square VL was aligned along the crystal [1 1 0] direction, whereas the rhombic VL consisted of two domains aligned along [1 0 0] and [0 1 0]. In addition, data taken at low temperatures[1] (T < 2.5K) indicated an increased disorder of the VL, and rotation of the vortices away from the applied field direction. The suggested cause of these effects was the development of the ferromagnetic component formed in this material below about 2.3K[3].

Since the initial studies on the VL in ErNi$_2$B$_2$C, a great deal of work has been carried out on the non-magnetic analogues Y- and LuNi$_2$B$_2$C[4-8] enabling a separation of those VL properties displayed in general in the borocarbides from those relating to the influence of magnetism. Work on YNi$_2$B$_2$C[6] revealed that the rhombic lattice also underwent a 45° reorientation at low fields. In addition, theoretical work by Kogan[9] and co-workers has successfully described the two vortex lattice transitions observed in the non-magnetic borocarbides as discussed in chapter 2 of this thesis. Since T_N is well below T_C in ErNi$_2$B$_2$C but both temperatures are easily accessible experimentally, the compound is ideal for investigating how the VL reacts to the development of magnetic order. The results described in this chapter are an investigation into the shape of the VL phase diagram in ErNi$_2$B$_2$C.

The experiments described in this chapter were carried out on the SANS instrument D22 at ILL which is arranged as described in chapter 4. An electromagnet was used to apply fields of up to 0.5T along the crystal c-direction. Each vortex lattice was grown by cooling the sample from above T_C in the required magnetic field. The sample was the same 15mg single crystal of $ErNi_2{}^{11}B_2C$ used in the magnetic structure experiments described in chapter 6 of this thesis.

7.2 Vortex Lattice Structures in $ErNi_2B_2C$

SANS data obtained in an applied magnetic field of 450mT are shown in figure 7-1; the sample temperature is 2K. The data shown is a sum of many images collected over full ω and ϕ 'rocks' (see figure 4-7). The axes have been converted from detector pixels to show intensity as a function of scattering vector $\mathbf{Q}$ using the sample-to-detector distance and neutron wavelength. The number and locations of the Bragg peaks clearly show that the VL symmetry is square under these conditions: there are four strong first order (10) and four much weaker second order (11) peaks; the sides of the square are aligned along the crystal [1 1 0] directions.

Figure 7-2a shows data collected in an intermediate field of 200mT (5.6K). This image has been constructed from a single dataset reflected about vertical and horizontal axes; it shows how the complete pattern would appear if a full rocking curve had been collected and illustrates the difference in symmetry compared to figure 7-1. This data shows the upper rhombic phase. There are two domains, oriented at 90° to each other, each providing six first order spots on the detector to give a total of twelve. For a hexagonal lattice with no distortion, all of these first order spots would lie on a circle, with 30° between each, as the magnitude of the scattering vector would be the same for each spot. The two domains are illustrated schematically in figure 7-2b for clarity. The rhombus diagonals are along the crystal [1 0 0] and [0 1 0] directions, in agreement with the theoretical prediction[9].

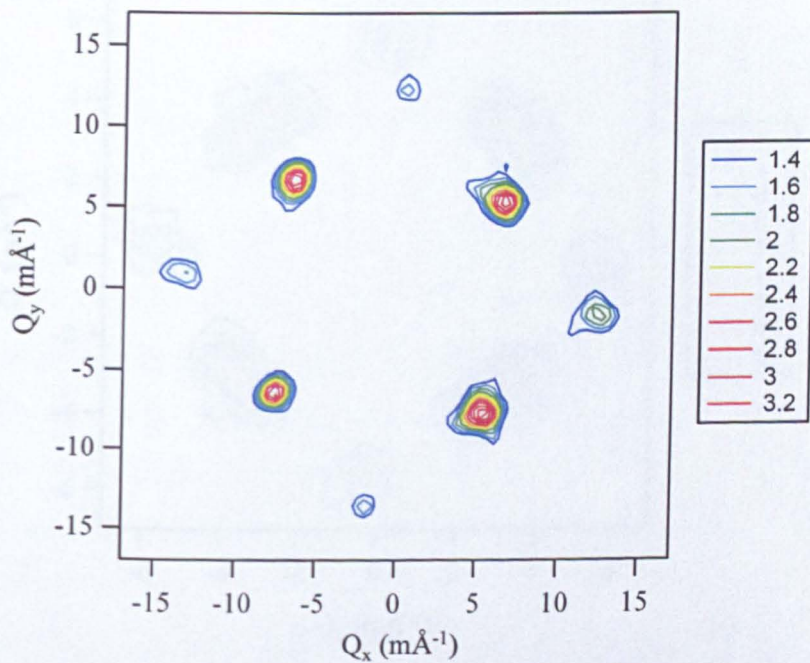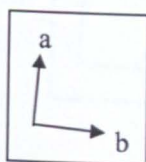Figure 7-1: SANS diffraction pattern obtained at 2K in a field of 450mT. The intensity is logarithmic in order that the weaker {11} spots are visible. The symmetry is clearly that of a square vortex lattice.

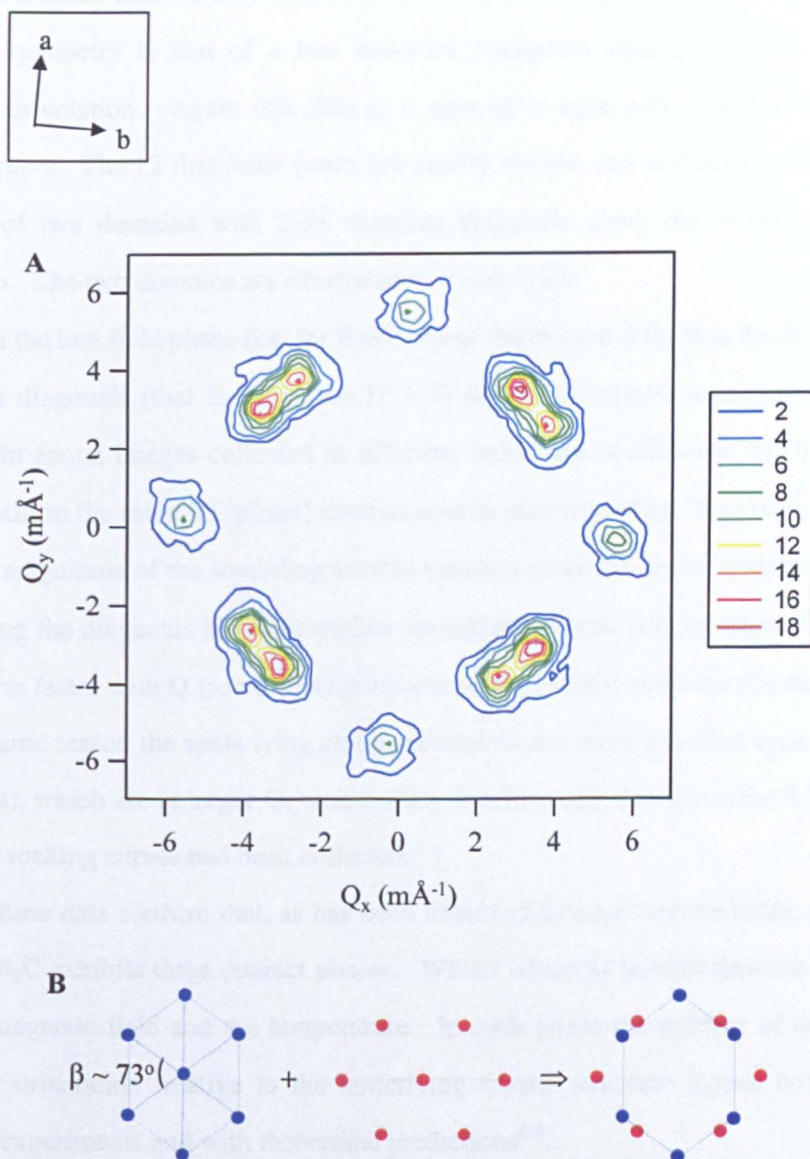Figure 7-2: a) Diffraction pattern obtained from $ErNi_2B_2C$ at 5.6K, 200mT. It consists of two domains of rhombic (distorted hexagonal) vortex lattices oriented at 90° as illustrated in b).

In a small field of only 20mT, in this case at a temperature of 4K (figure 7-3a), the symmetry is that of a less distorted hexagonal lattice, but now with a different orientation. Again this data is a sum of images collected over the full rocking curve. The 12 first order peaks are clearly visible, and in this case the image consists of two domains with their rhombus diagonals along the crystal [1 1 0] directions. The two domains are illustrated in figure 7-3b.

In the low field phase (i.e. for fields below the critical field H$_1$), the four spots along the diagonals (that is, along the [1 1 0] directions) appear stronger than the other eight spots; images collected in different fields and at different temperatures (though still in the same VL phase) showed similar characteristics. This is due to the different magnitude of the scattering vectors resulting from the lattice distortion. The spots along the diagonals have the smaller scattering vectors, and the rapid decrease of the form factor with Q (see §4.5.4) gives rise to this visible variation of intensities. For the same reason the spots lying along the axes in the more distorted upper phase (figure 2a), which are at larger Q, would show less intensity than the other 8 spots if complete rocking curves had been collected.

These data confirm that, as has been observed in other borocarbides, the VL in ErNi$_2$B$_2$C exhibits three distinct phases. Which lattice is formed depends on the applied magnetic field and the temperature. In each phase the number of domains and their orientation relative to the underlying crystal structure agrees both with previous experiments and with theoretical predictions[4-9].
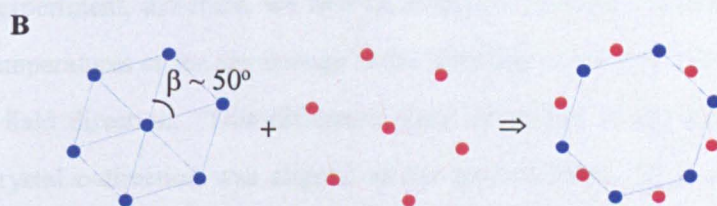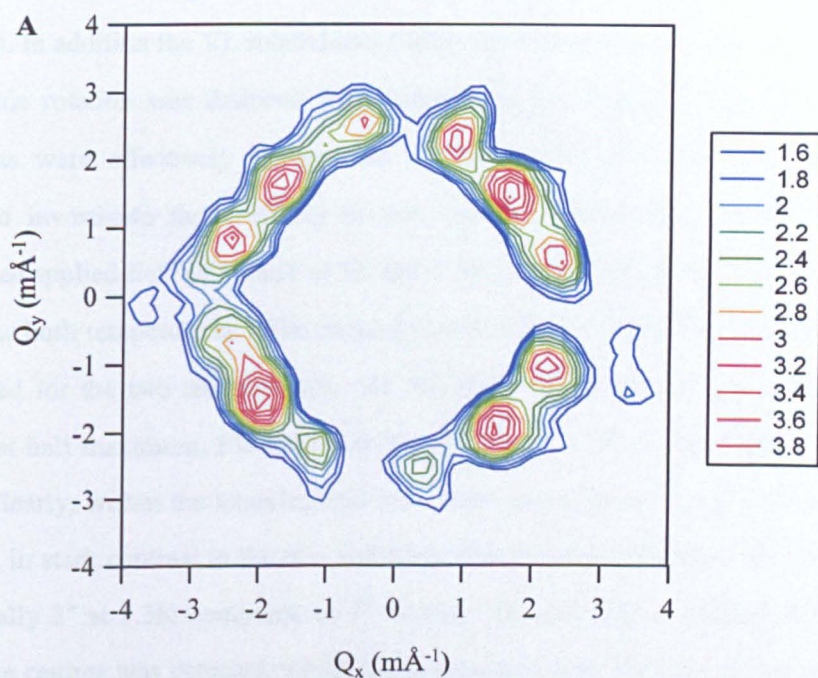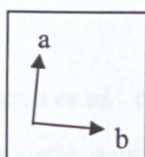
Figure 7-3: a) SANS diffraction obtained from $ErNi_2B_2C$ in a field of 20mT at 4K. The two domains, indicated in b), have diagonals aligned along the crystal [110] directions.

7.3 Properties of the Vortex Lattice at Low Temperatures

Yaron et al.[1] reported that at temperatures below approximately 2.3K, where a ferromagnetic component to the magnetisation develops (see §6.2), the VL in ErNi$_2$B$_2$C disorders, causing an increase in the rocking curve widths of at least a factor of two. In addition the VL rotated away from the direction in which the field is applied. This rotation was deduced from changes in the rocking curve centres. These effects were effectively independent of the applied field over the range studied. To investigate those effects in this sample, full rocking curves were collected in an applied field of 500mT at 3K and 1.5K; at this field the VL has square symmetry for both temperatures. The rocking curve width of every first order spot was measured for the two temperatures. At 3K, the average rocking curve width (half width at half maximum, FWHM) is 0.7($\pm$0.2)$^{\circ}$ and at 1.5K it was found to be 0.8(0.2)$^{\circ}$. Clearly, within the experimental error there is no increase in the rocking curve width, in stark contrast to the two and three-fold increases observed by Yaron et al. (typically 3° at 1.5K compared to 1° at 3K). In addition, no change in the rocking curve centres was detected, which again disagrees with the data of Yaron et al. In this experiment, therefore, we find no evidence for either disordering of the VL at low temperatures or for any change in the direction of the flux lines relative to the applied field direction. This difference may be related to the accuracy with which the crystal c-direction was aligned to the applied field. If, in the work of Yaron et al., there was an offset between c and B, the flux-lines may have been aligned along B or have taken some compromise direction at higher temperatures, and then been forced to align themselves along c once the ferromagnetic component was formed. In this case, with good alignment, the orientation of the vortices would be unaffected by the development of the ferromagnetic state below 2.3K.

7.4 The Square to Rhombic Symmetry Transition at H$_2$

During the experiments VL images were collected at different temperatures and fields in order to examine the transitions and to gain an indication of the shape of the VL phase diagram. Of particular interest is the transition from rhombic to square symmetry at the field denoted H$_2$, which from theory is predicted to increase with temperature. This transition, which is of second order, has been studied extensively in the non-magnetic Y and Lu compounds. As the applied field is reduced from above H$_2$, where the lattice is square, in reciprocal space each Bragg spot from the square VL smoothly splits into two at the transition to rhombic symmetry.

At various temperatures, data were collected in magnetic fields ranging from 100mT up to 500mT. Due to time constraints, the full rocking curve was not collected at every field but instead the conditions were set so that the (10) peak from the square lattice was 'rocked on', i.e. at the mean Bragg condition. This method provides ample information to determine both the lattice morphology and its orientation relative to the underlying crystal axes at any point. The large changes with field of the lattice spacing, d_{hk}, and resultant scattering vector Q_{hk}, would normally require substantial alterations of the sample to detector distance to observe the VL at constant wavelength, giving different instrumental resolution at each field. To avoid this complication, the wavelength was altered for each different applied field to keep 2θ and hence Q constant. Each spot on the detector was fitted with a two-dimensional Gaussian function (written by D.McK.Paul), assuming an elliptical spot with the radial and azimuthal widths being the major axes, to obtain its position on the detector (and thus its Q), its radial and azimuthal widths and an indication of the relative intensities as conditions are changed; a true measure of the integrated intensities would have required full rocking curves for each point. This analysis is carried out after subtracting a background run taken at 12K, well above T$_C$, in the appropriate applied field. The origin of reciprocal space on the detector is

determined by calculating the centre of mass of the straight through beam without the beam-stop; for this measurement an attenuator is placed in the beam to protect the detector. Since the square to hexagonal transition is of second order (i.e. continuous), one analytical approach is to start from high fields where the square lattice is formed, considering a single peak and observing its behaviour as the field is reduced. The transition should be detectable by examining the changes in scattering vector, resulting from the different VL spacings d_{hk} of the square and rhombic symmetries, and via an increase in the azimuthal width as the spot splits into two. The location of the transition field H$_2$ may be estimated using this method.

Data were collected in fields of 100-500mT at a temperature of 5.6K, a little below T$_N$. Figure 7-4 shows the radial and azimuthal widths of the observed peaks at this temperature obtained from a single 2-D Gaussian fit as described above. Both widths are affected by input collimation, which is the same for all fields, and by the mosaic spread of the VL; in addition, the radial width has a contribution from the wavelength spread, $\delta\lambda/\lambda$ (typically ~10%). As a result, a single Bragg peak on the detector should have comparable radial and azimuthal widths, and if the quality of the VL is affected by changing conditions, this will be revealed in these spot widths. In figure 7-6, the two widths are similar for fields above 300mT, where the VL is square. As the field is lowered below 300mT the azimuthal width of the peak increases. The radial width, however, is unaffected, suggesting that the VL quality is not noticeably changed and that the increase in azimuthal width is due to the splitting of the Bragg peak as the transition from square to rhombic symmetry occurs. The larger error bars at low fields indicate the difficulty of persisting with a single spot fit as the peaks get further apart, since as the field is decreased the two spots eventually become completely separate.

Figure 7-5 shows the variation of the VL spacing, d_{hk}, with applied field at 5.6K as calculated from the scattering vector **Q** given by the fit. Also shown are curves corresponding to ideal square and triangular lattices. Above 300mT the

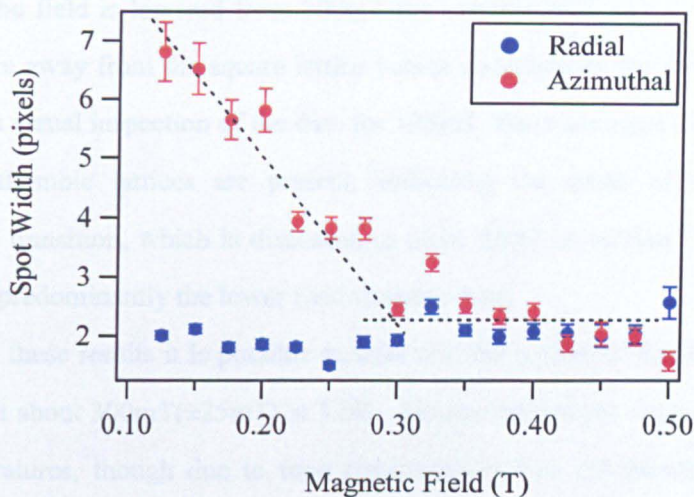Figure 7-4: Variation of radial and azimuthal widths of VL Bragg peaks from $ErNi_2B_2C$ with applied field at 5.6K.
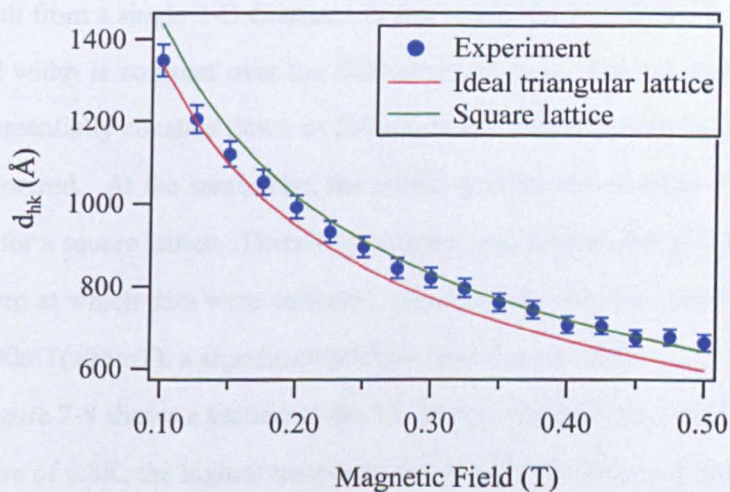

Figure 7-5: Variation of vortex lattice spacing, d_{hk}, with applied magnetic field at a temperature of 5.6K.

experimental values agree well with those expected for a square lattice for those fields. As the field is lowered from 300mT the experimental values for the lattice spacing move away from the square lattice values and towards the triangular lattice line. From a visual inspection of the data for 125mT, there are signs that both upper and lower rhombic lattices are present, indicating the onset of the 1st order reorientation transition, which is discussed in more detail in section 7.6; at 100mT the lattice is predominantly the lower field rhombic type.

From these results it is possible to infer that the square to rhombic transition takes place at about 300mT($\pm$25mT) at 5.6K. Similar field scans were carried out at other temperatures, though due to time constraints it was not possible to collect information over such a large field range at every temperature. Nevertheless, sufficient data were collected to provide an initial indication of the variation of H$_2$ with temperature.

Figures 7-6 and 7-7 show the variation of the radial and azimuthal spot widths and the calculated lattice spacing for data obtained at 1.5K; like the 5.6K data, these result from a single 2-D Gaussian fit starting at the highest fields. As expected the radial width is constant over the field range studied. The azimuthal width also remains essentially constant down to 200mT, below which it starts to increase as the field is lowered. At the same time, the lattice spacing moves away from the value expected for a square lattice. These two observations suggest that at 1.5K, the lowest temperature at which data were collected, the square to rhombic transition occurs at around 200mT($\pm$25mT), a significantly lower field than at 5.6K.

Figure 7-8 shows a section of the VL image obtained in a field of 300mT at a temperature of 6.8K, the highest temperature at which data were collected. Although at high temperatures the spot intensities become very weak, this data shows two almost separate spots (towards the centre of the image), indicating that H$_2$ is substantially higher than 300mT at this temperature. Data collected at 400mT gives an azimuthal width of 3.9($\pm$0.4) pixels compared to a radial width of 2.4($\pm$0.3)
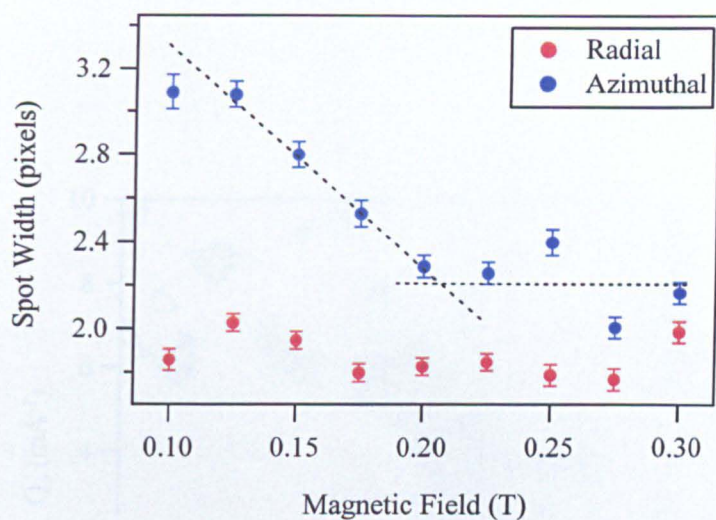
Figure 7-6: Variation of radial and azimuthal spot width with magnetic *field in ErNi₂B₂C at 1.5K*
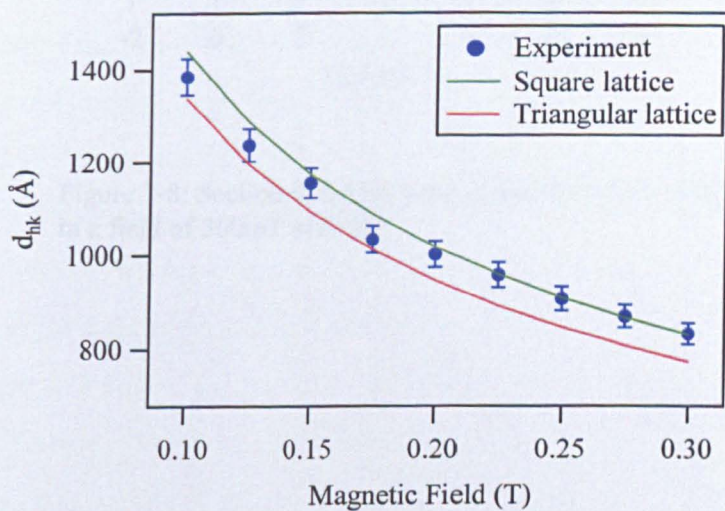

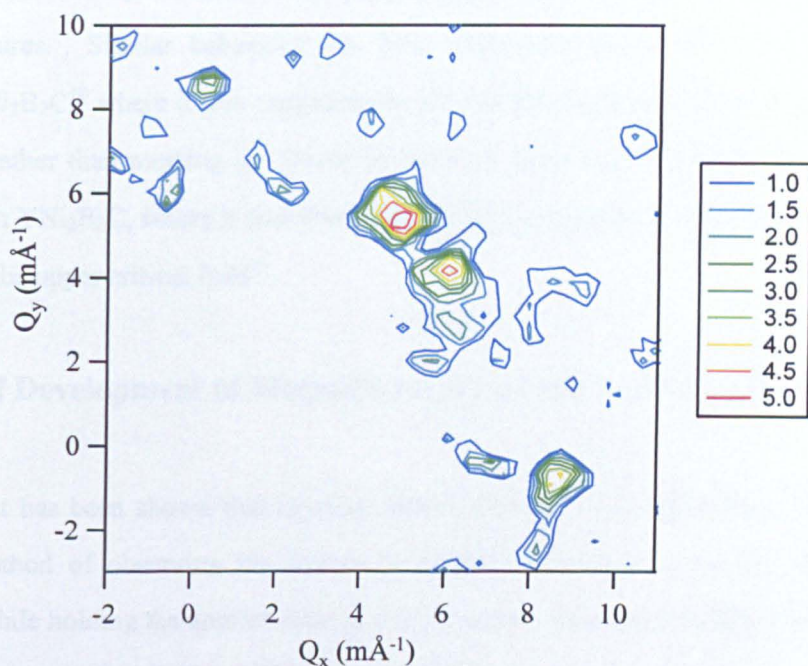Figure 7-7: Variation of lattice spacing with field at 1.5K.

Figure 7-8: Section of SANS image obtained from $ErNi_2B_2C$ in a field of 300mT at 6.8K.

pixels. Comparison with the behaviour of the azimuthal widths at 1.5K and 5.6K suggests that H_2 is considerably higher than 400mT at this temperature. Since the estimated value of H_2 only increased by 100mT over a temperature range of 1.5 to 5.6K, this implies that H_2 increases much more rapidly at higher temperatures than at low temperatures. Similar behaviour has been reported recently for the non-magnetic $LuNi_2B_2C$[10] where it was suggested the H_2 line bends away from the upper critical field rather than meeting it. However, no such behaviour was observed in recent work on YNi_2B_2C, where it was observed that H_2 does indeed extrapolate to a meeting with the upper critical field[11].

7.5 Effect of Development of Magnetic Order on the Vortex Lattice

Since it has been shown that H_2 does indeed increase with temperature, an alternative method of observing the square to rhombic transition is to vary the temperature while holding the applied field at a fixed value. Such temperature scans were carried out in applied fields of 200, 300 and 400mT.

Figure 7-9 shows the variation in the radial and azimuthal widths of a single spot with temperature in an applied field of 200mT. Again, the increase in azimuthal width while the radial width remains constant indicates that the spot is splitting at the square to rhombic transition. It has already been seen that at 1.5K, H_2 is around 200mT so that both widths are similar at the lowest temperatures. The azimuthal width increases slowly at first, then with larger gradient as the temperature increases, always smoothly to just above 5.5K. In a narrow temperature range around T_N the azimuthal width is dramatically suppressed. The minimum is at 5.8K, which from laboratory experiments and magnetic structure measurements (chapter 6) is T_N. Above 6.5K this width recovers and continues to increase almost as if the dip at T_N had not occurred. Throughout, the radial width remains constant at around two pixels. Figure 7-10 shows VL images collected just below, just above, and at T_N.

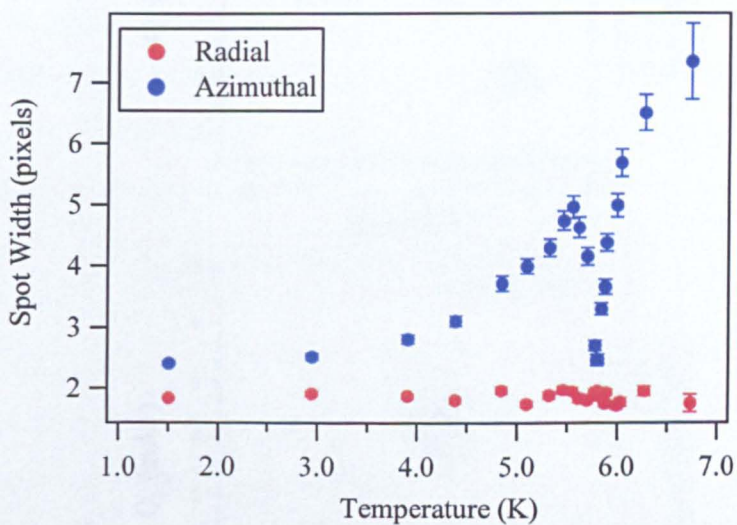Figure 7-9: Variation of radial and azimuthal spot widths with temperature in ErNi$_2$B$_2$C with an applied magnetic field of 200mT.
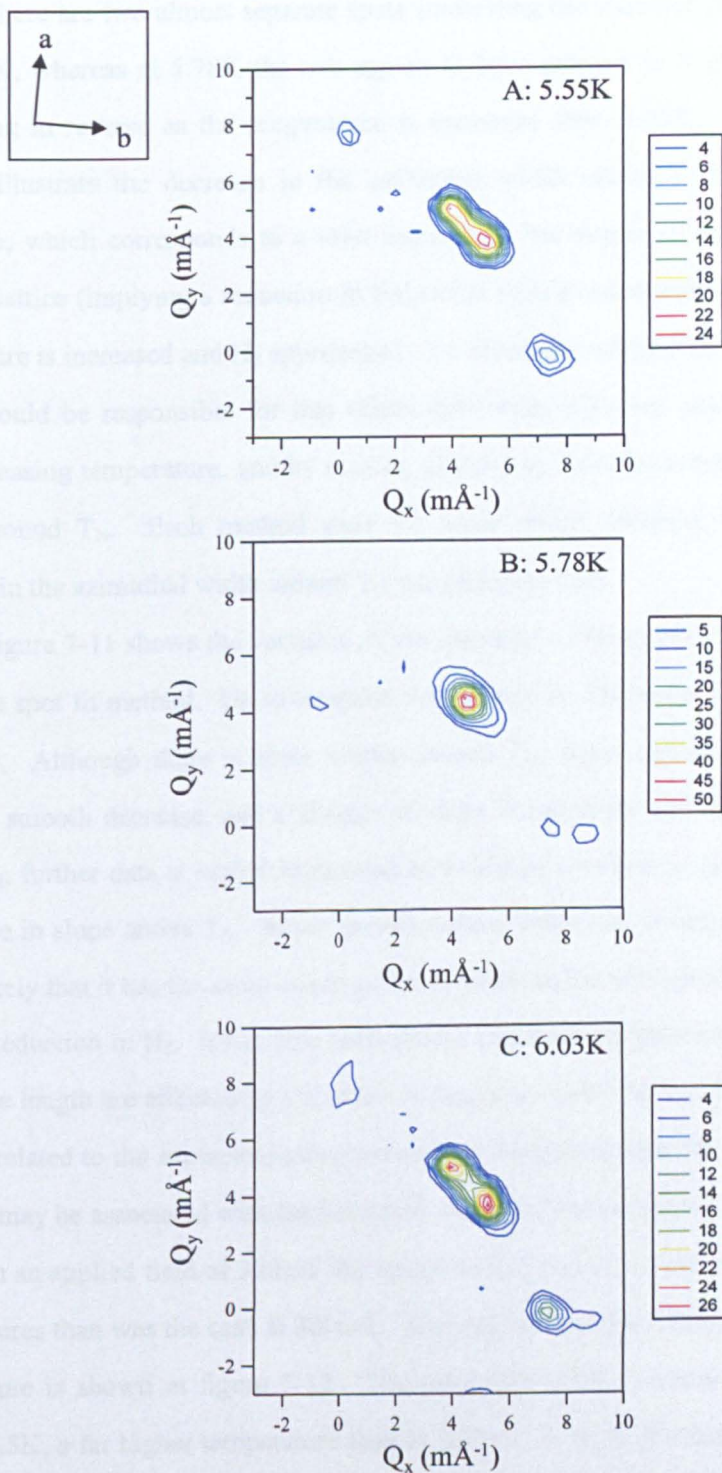
Figure 7-10: Sections of SANS images obtained from ErNi$_2$B$_2$C at different temperatures in an applied field of 200mT

Clearly, there are two almost separate spots (indicating the rhombic phase) at 5.55K and 6.03K, whereas at 5.78K the two appear to have merged as if the transition is proceeding in reverse as the temperature is increased from 5.55K. These images visually illustrate the decrease in the azimuthal width obtained from the fitting procedure, which corresponds to a brief increase in the degree of distortion of the rhombic lattice (implying a reduction in H$_2$) rather than a monotonic decrease as the temperature is increased and H$_2$ approached. To determine whether the history of the sample could be responsible for this effect, data were collected both sequentially, with increasing temperature, and by cooling directly to different temperatures in the region around T$_N$. Each method gave the same result, showing that the sharp decrease in the azimuthal width around T$_N$ is a genuine effect.

Figure 7-11 shows the variation of the intensity of the spot(s), obtained using the single spot fit method. Up to temperatures near to T$_N$ the intensity is decreasing smoothly. Although there is some scatter around T$_N$, there appears to be a break from the smooth decrease, and a change of slope between the data below and that above T$_N$; further data at higher temperatures would be required to be certain of the difference in slope above T$_N$. Since the anomalous behaviour is very close to T$_N$ it seems likely that it has the same origin as the decrease in the azimuthal width and the implied reduction in H$_2$. It has also been shown that both the penetration depth and coherence length are affected by the onset of magnetic order[12] at T$_N$; the non-locality range is related to the superconducting parameters suggesting that the variations in λ and/or ξ may be associated with the behaviour observed here close to T$_N$.

In an applied field of 300mT the square lattice should remain stable to higher temperatures than was the case at 200mT. The variation of the azimuthal width with temperature is shown in figure 7-12. The azimuthal width remains constant until around 4.5K, a far higher temperature than at 200mT, as would be expected. At this field there is also a dip in the azimuthal width at T$_N$, when compared to the data points at 4.8 and 6.8K which clearly show increased azimuthal width corresponding
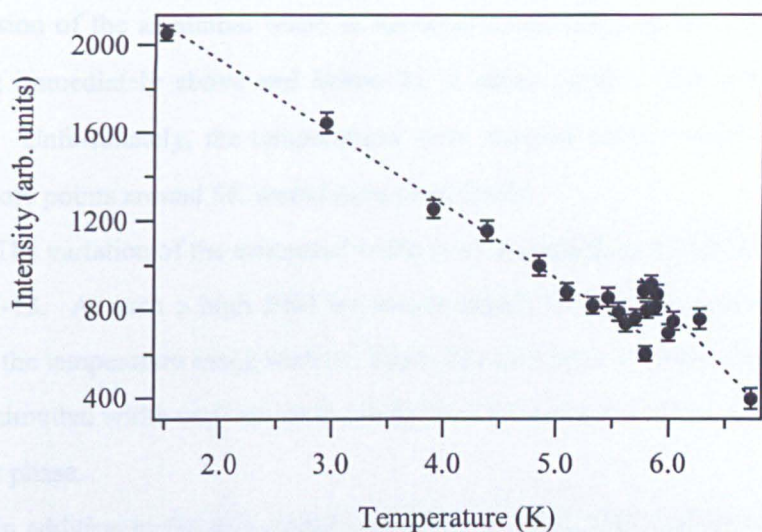
Figure 7-11: Variation of intensity of Bragg peaks with temperature in ErNi$_2$B$_2$C in an applied field of 200mT. The intensity has been obtained using the 2-D Gaussian fit described in the text.
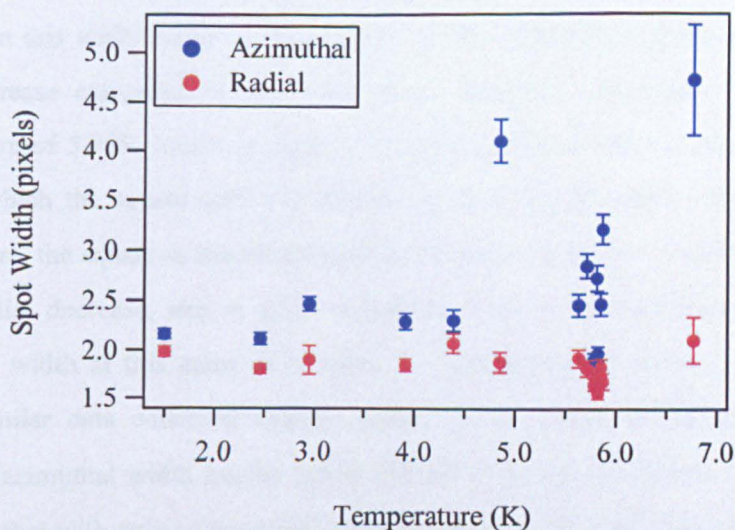

Figure 7-12: Variation of radial and azimuthal widths with temperature in an applied field of 300mT

to a small splitting of the spots as the square to rhombic transition occurs. The suppression of the azimuthal width is not as dramatic since at this higher field the splitting immediately above and below T$_N$ is much smaller than was the case at 200mT. Unfortunately, the temperatures were selected based on the 200mT data, when more points around 5K would have been useful.

The variation of the azimuthal width in an applied field of 400mT is shown in figure 7-13. At such a high field we would expect to find the square lattice over most of the temperature range studied. From this data there is essentially no increase in the azimuthal width until above T$_N$; only the 6.8K point shows the signature of the rhombic phase.

In addition to the data already presented at 1.5K, 5.6K and 7K (section 7.4), data were collected as a function of applied field at several other temperatures near T$_N$ to investigate whether the dramatic increase in distortion causes an observable reduction in H$_2$, the location of the square to rhombic transition. The transition appears to occur at 300mT(±25mT) at 5.6K. Figure 7-14 shows the variation of the azimuthal width with applied field at a temperature of 5.71K. The onset of the increase in this width occurs below 325mT at this temperature, showing perhaps a small increase compared to the 5.6K data. However, the data collected at a temperature of 5.78K shown in figure 7-15 does appear to show a decrease on the field at which the square lattice is formed again using the same criteria. At this temperature, the square to rhombic transition seems to be as low as 200mT(±25mT), a substantial decrease, and in good agreement with the severe depression in the azimuthal width at this same field when the temperature is varied. Figure 7-16 shows similar data collected slightly above T$_N$, this time at 5.84K. Here the enhanced azimuthal width begins below 325mT as it did just below T$_N$ at 5.71K, indicating that with only a very small temperature rise (0.06K) H$_2$ has recovered to a field value similar to that seen just below T$_N$. Figure 7-17 shows data obtained at the slightly higher temperature of 5.88K, which continues the apparent upward trend in H$_2$ to 325-350mT. These data suggest a suppression of H$_2$ over a temperature range
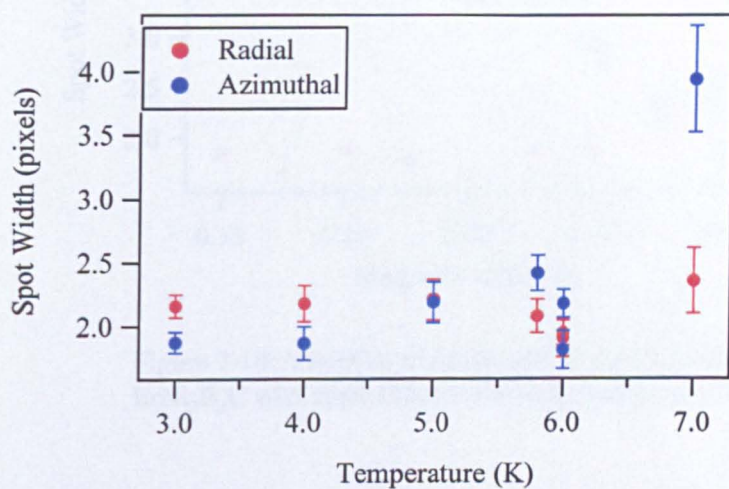
Figure 7-13: Variation of radial and azimuthal widths with temperature in $ErNi_2B_2C$ with an applied field of 400mT

Figure 7-14: Variation of radial and azimuthal widths in ErNi$_2$B$_2$C with applied field at a temperature of 5.71K.

Figure 7-15: Variation of radial and azimuthal widths with applied field at a temperature of 5.78K.
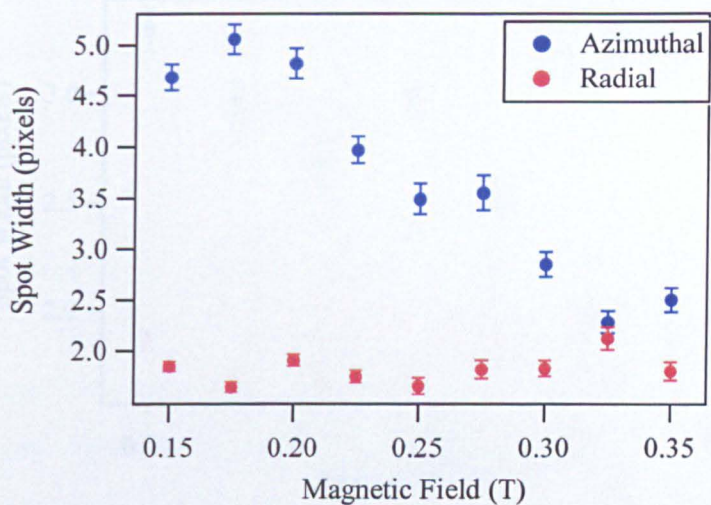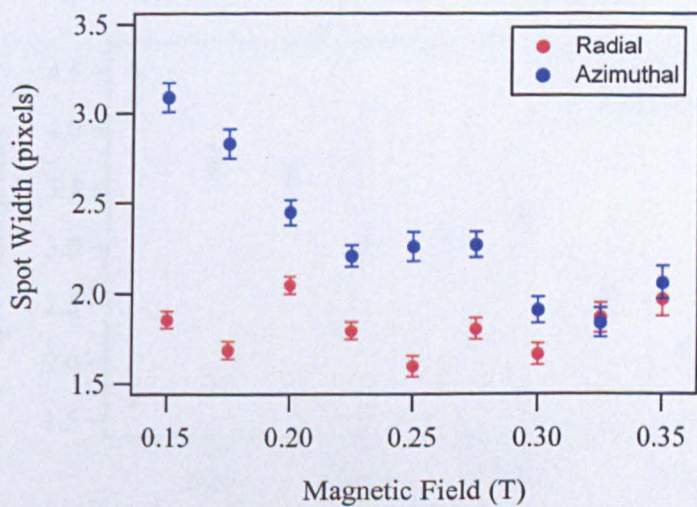
Figure 7-16: Variation of radial and azimuthal widths in ErNi$_2$B$_2$C with applied field at a temperature of 5.84K.

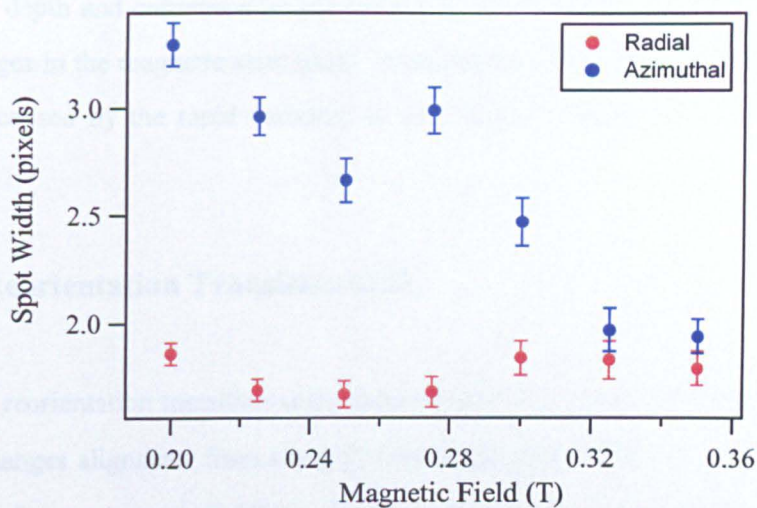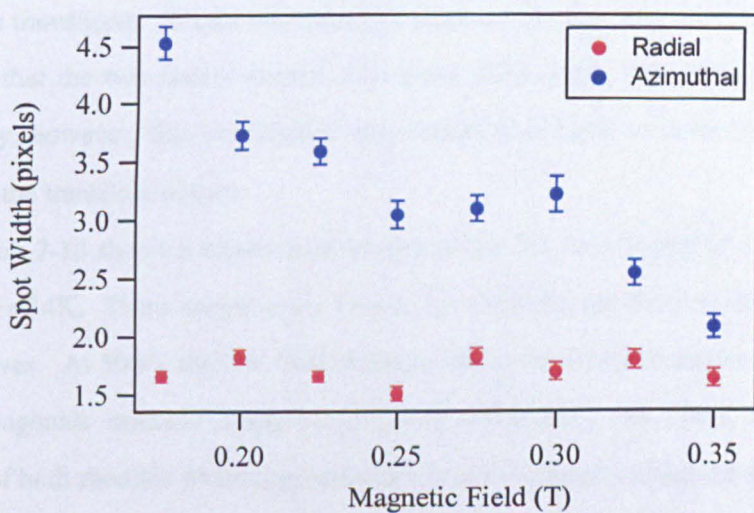Figure 7-17: Variation of radial and azimuthal widths with applied field at a temperature of 5.88K.

of less than 0.15K very close to T_N. This suppression coincides with changes in the penetration depth and coherence length around T_N as observed elsewhere[12], as well as the changes in the magnetic state itself. It seems likely that the suppression of H_2 is directly caused by the rapid variation in the magnetic susceptibility on passing through T_N.

7.6 The Reorientation Transition at H_1

The reorientation transition at the field denoted H_1, where the diagonal of the rhombus changes alignment from along [1 0 0] (high field side) to [1 1 0] has been the subject of some theoretical debate. In the work by Kogan[9], this was described as a 1st order phase transition, because no smooth method of adjusting the rhombus angles exists to get from one orientation to the other. This is in contrast to the square-to-rhombic transition at H_2, which can be achieved by 'stretching' the square along the [1 0 0] or [0 1 0] directions. However, Knigavko et al.[13] have more recently suggested that the reorientation is in fact made up of two successive 2nd order phase transitions. Recent experimental work on the non-magnetic YNi_2B_2C[14] has shown that the two phases coexist over some field range, supporting the first-order theory; however, this coexistence also makes it difficult to define exactly at which field the transition occurs.

Figure 7-18 shows a selection of images of the VL in low applied fields at a temperature of 4K. These images were formed by summing the datasets from full ω rocking curves. At 50mT the low field rhombic lattice is clearly observed, with the rhombus diagonals oriented along the [1 1 0] directions. At 75mT there are signatures of both rhombic phases, as now there is extra intensity along the diagonals and also intensity along the crystal a and b axes, as would be observed from the high field rhombic lattice. At 100mT it appears that the intensity from the low field phase has effectively disappeared leaving only the upper rhombic phase, whose two
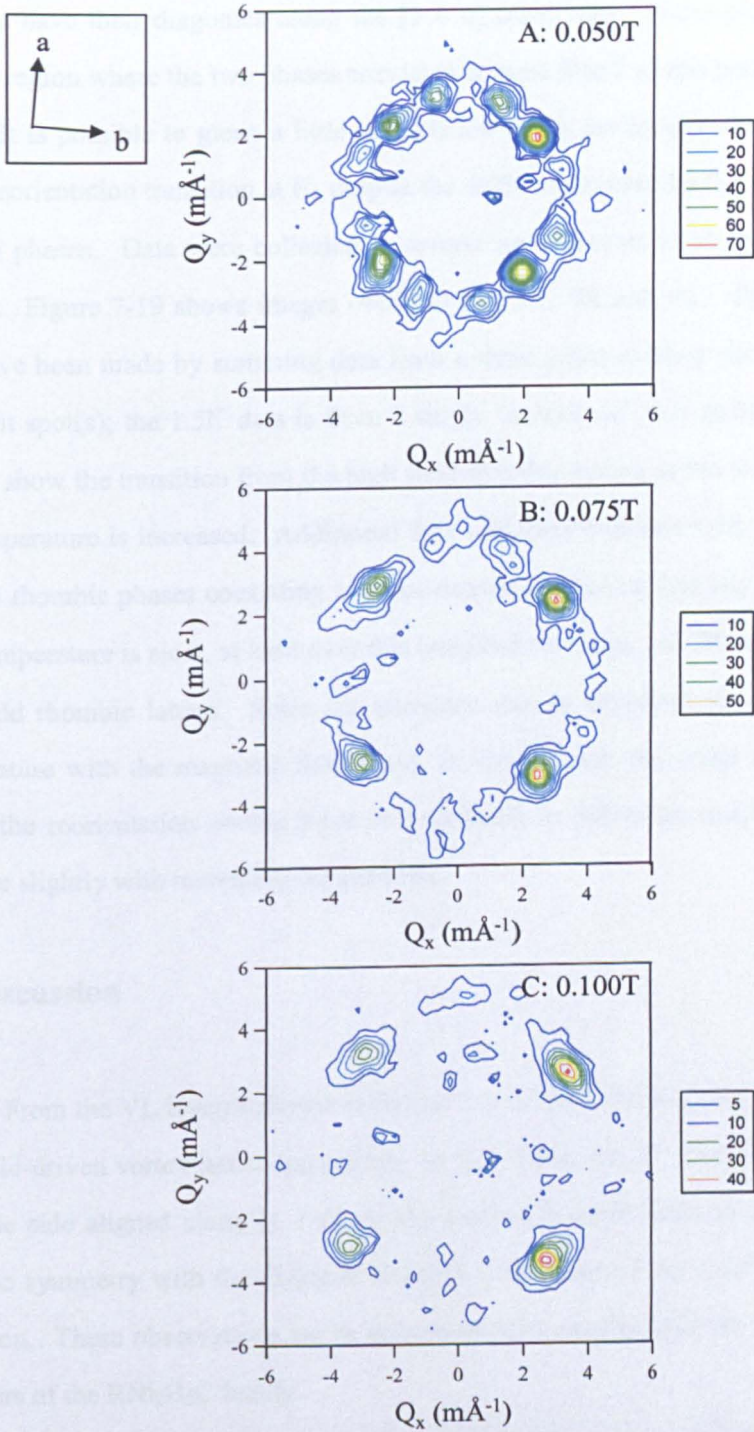
Figure 7-18: SANS images from ErNi₂B₂C at 4K in different applied fields.

domains have their diagonals along the [1 0 0] directions. These pictures suggest that the region where the two phases coexist is at most 50mT at this temperature.

It is possible to glean a little information about the temperature dependence of the reorientation transition at H$_1$ despite the difficulty caused by the coexistence of the two phases. Data were collected at several temperatures in an applied field of 100mT. Figure 7-19 shows images obtained at 1.5K, 5K and 7K. The 5K and 7K data have been made by summing data from a three point rocking curve around the top right spot(s); the 1.5K data is from a single 'rocked on' data collection. These images show the transition from the high field rhombic lattice to the low field one as the temperature is increased. Additional data collected between 1.5K and 5K show the two rhombic phases coexisting to some degree, indicating that any change of H$_1$ with temperature is slow, at least over this temperature range. At 7K we see only the low field rhombic lattice. Since the transition can be observed by increasing the temperature with the magnetic field fixed, H$_1$ (or at least, the range of fields over which the reorientation occurs since it is difficult to define an exact value) must increase slightly with increasing temperature.

7.7 Discussion

From the VL images shown in figures 7-1 to 7-3 ErNi$_2$B$_2$C clearly undergoes two field-driven vortex lattice transitions. In high fields the VL symmetry is square, with the side aligned along [1 1 0]; as the field is lowered there is a transition to rhombic symmetry with the diagonal along [1 0 0] followed by a 45° reorientation transition. These observations are in agreement with results from the non-magnetic members of the RNi$_2$B$_2$C family.

Analysis of the quality and orientation of the VL with respect to the magnetic field at low temperatures shows discrepancies with previously published results. In these experiments, there is no large increase in rocking curve width, which would
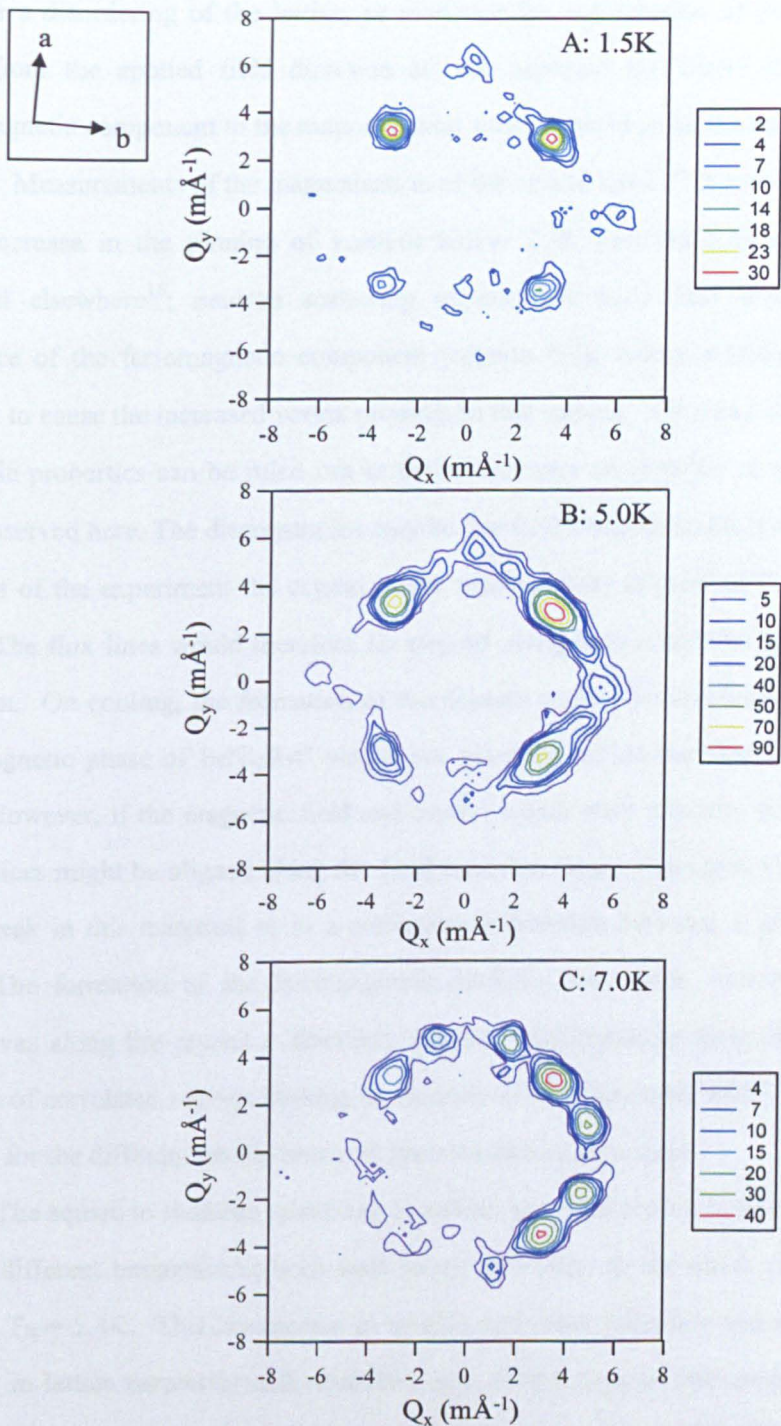
Figure 7-19: SANS images from ErNi₂B₂C at different temperatures in an applied field of 0.1T

indicate a disordering of the lattice, or evidence for any rotation of the flux lines away from the applied field direction as was reported by Yaron *et al*[1]. The ferromagnetic component to the magnetisation was proposed to be the cause of those effects. Measurements of the magnetisation of the crystal used in this work show the same increase in the pinning of vortices below 2.3K (section 6.2) as has been reported elsewhere[15]; neutron scattering experiments have also confirmed the existence of the ferromagnetic component (section 6.4), whose domain walls are thought to cause the increased vortex pinning, in this sample. Thus any difference in magnetic properties can be ruled out as the reason why no disorder or rotation has been observed here. The discrepancies may be due to the experimental technique. At the start of the experiment the crystal *c*-axis was carefully aligned to the magnetic field. The flux lines would therefore be aligned along both *c* and the applied field direction. On cooling, the formation of the domain walls (see section 6.3.2) in the ferromagnetic phase of ErNi₂B₂C would not adversely affect the flux lines in this case. However, if the magnetic field and crystal *c*-axis were not very well aligned, the vortices might be aligned along the field direction (since pinning is known to be quite weak in this material) or in a compromise direction between B and *c* above T_{WF}. The formation of the ferromagnetic domains may force vortices to align themselves along the crystal *c* direction, possibly also breaking them into smaller sections of correlated regions causing an increase in rocking curve width. This may account for the different results obtained from the two experiments.

The square to rhombic symmetry transition at a field H_2 has been observed at several different temperatures both well below and close to the onset of magnetic order at $T_N = 5.8K$. This is expected to be a second order transition and the smooth changes in lattice parameter and azimuthal spot widths support this conjecture. In each case, a single spot observed due to the square lattice in the high field regime continuously splits into two spots which then become two of the twelve first order peaks observed in the rhombic phase. By comparing the data obtained as a function

of field at different temperatures it is possible to follow the general behaviour of the field H_2 with temperature. Comparison of data obtained at 1.5, 5.6 and 6.8K clearly show that H_2 has increased with temperature; moreover, it appears that H_2 increases much more rapidly at higher temperatures. An increase of H_2 with increasing temperature is expected, since H_2 is determined in part by the electronic mean free path which will decrease as the temperature increases. In addition, when the transition is observed by increasing the temperature in a fixed applied field of 200 or 300mT, sharp anomalies are evident in the azimuthal width and intensity at temperatures very close to the magnetic transition at $T_N = 5.8K$.

It is instructive to compare these results with a similar study of the temperature dependence of H_2 in the non-magnetic $LuNi_2B_2C$[10]. In that material, essentially no increase is observed in H_2 up to around 10K ($T_C(0) = 16K$) followed by a rapid increase and eventually a turning away of H_2 from the H_{C2} line. This is in disagreement with the theoretical predictions from which an interception of the two lines would be expected. In $LuNi_2B_2C$, for a range of fields where the square lattice is formed at $T \ll T_C$, the onset of the square-to-rhombic transition was observed at $T/T_C \sim 2/3$. However, recent work[11] on the other non-magnetic compound, YNi_2B_2C, as well as the work on the form factors in both compounds presented in chapter 5, contradict these observations. A detailed study of the square-to-rhombic transition in YNi_2B_2C showed a monotonic increase in H_2, from about 200mT at 2K to a little over 400mT just below $T_C(B)$. A relatively slow variation of H_2 at low temperatures is seen here in $ErNi_2B_2C$. There is also a rapid increase in H_2 that in the Er material apparently occurs in the temperature region near to T_N. Assuming that in these materials the line of H_2 does in fact intersect H_{C2}, as seems to be the case in both non-magnetic compounds, this change in slope may be related to the development of magnetic order in $ErNi_2B_2C$, with the slow temperature dependence below T_N resulting from a general suppression of H_2 in the magnetically ordered

state. Further data collected in higher fields are required to confirm whether H$_2$ meets H$_{C2}$ or turns away from it in ErNi$_2$B$_2$C.

As the reported increase in H$_2$ is smooth in the non-magnetic Lu and Y compounds, the sharp features observed around 5.8K in ErNi$_2$B$_2$C must certainly be associated with the formation of magnetic order at T$_N$ = 5.8K. The applied magnetic field at which the square to rhombic symmetry transition takes place is determined by the distance over which non-local effects are important. These results suggest that at temperatures very close to T$_N$ there is a sharp change in this non-locality range compared to temperatures above and below T$_N$. Gammel et $al.$[12] have studied the effect of the development of magnetic order at T$_N$ on the superconducting coherence length, ξ(T), and penetration depth λ(T) in ErNi$_2$B$_2$C and have found distinct anomalies in both parameters on passing through the magnetic transition. The non-locality range is related to these superconducting parameters as well as the electronic mean free path[9]. At a magnetic transition the electronic properties are generally also affected, so that some variation of the mean free path is likely. This strongly suggests that the variation of both superconducting and normal state electronic properties (and possibly also the magnetic susceptibility) around T$_N$ are involved with the distinctive increase in lattice distortion and reduction of H$_2$ in a narrow temperature range around T$_N$ observed in these experiments.

In section 7.6 data is presented that clearly indicates a small but definite increase in H$_1$, the location of the 45° reorientation transition, with increasing temperature. The coexistence of the two rhombic phases complicates the situation, as the transition apparently takes place over a field range of as much as 50mT. The transition appears to proceed by the gradual increase of one orientation at the expense of the other. This coexistence of the two phases indicates that this transition is of first order, which does not support the alternative of two successive second order transitions[13] instead of a single first order transition. There has to date been little experimental work on the temperature dependence of this transition and as yet

there are no theoretical predictions with which to make any comparisons. A more detailed study of the reorientation transition in the non-magnetic analogue YNi$_2$B$_2$C[11] than was possible for the Er compound in this study shows a slight decrease in H$_1$ with temperature for that material, in contrast to the increase detected here. More extensive and detailed experiments will be required to follow the exact behaviour of this reorientation with temperature so that the behaviour as H$_{C2}$ is approached may be investigated. If it is found that the square-to rhombic transition H$_2$ curves away from H$_{C2}$ rather than meeting it in ErNi$_2$B$_2$C, as has been suggested for LuNi$_2$B$_2$C, it may be that the reorientation at H$_1$ follows the same behaviour, in which case an increase in H$_1$ as observed here would be expected.

Although there is less data available regarding the reorientation transition at H$_1$, there is no evidence for any rapid change in its slope with temperature as is clearly the case for the transition to square symmetry at H$_2$. It is also impossible to determine if the onset of magnetic order at T$_N$ = 5.8K has any impact on the reorientation without carrying out a far more detailed study. It is likely that the nature of this transition, with the coexisting phases, would make it difficult to observe any such effect if it exists.

In this chapter the vortex lattice in magnetic ErNi$_2$B$_2$C has been investigated using small angle neutron scattering. Three different VLs have been observed: square, with the side aligned along [1 1 0] at the highest fields, then rhombic lattices with diagonals along first [1 0 0] and then [1 1 0] as the applied field is reduced. The second order transition from square to rhombic symmetry at a field denoted H$_2$ has been followed and found to increase with temperature, weakly below T$_N$ = 5.8K but more rapidly at higher temperatures; however, a sharp increase in lattice distortion is observed in a narrow temperature region around T$_N$. This phenomenon appears to be due to changes in the superconducting and normal state parameters caused by the rapidly varying magnetic susceptibility. The reorientation of the rhombic lattice at

H_1 appears to be of first order. This critical field was found to increase slightly with temperature, in contrast to recent results on the non-magnetic analogue YNi$_2$B$_2$C[14].

References

[1]   U. Yaron *et al.*, Nature **382** p236-238 (1996)

[2]   M. R. Eskildsen *et al.*, Phys. Rev. Letts. **78** No. 10 p1968 (1997)

[3]   P.L. Gammel *et al.*, Phys. Rev. Letts. **84** No.11 p2497 (2000)

[4]   M. Yethiraj *et al.*, Phys. Rev. Letts. **78** No. 25 p4849 (1997)

[5]   M.R.Eskildsen *et al.*, Phys. Rev. Letts. **79** No. 3 p487 (1997)

[6]   D. McK. Paul *et al.*, Phys. Rev. Letts. **80** No 7 p1517 (1998)

[7]   M.R. Eskildsen *et al.*, Physica B **242** p811 (1998)

[8]   M. Yethiraj *et al.*, Phys. Rev. B **58** No. 22 pR14767 (1998)

[9]   V.G. Kogan *et al.*, Phys. Rev. B **55** No. 14 pR8693 (1997)

[10]   M.R. Eskildsen *et al.*, Phys. Rev. Letts. **86** No. 22 p5148 (2001)

[11]   S.J. Levett *et al.*, to be published

[12]   P.L. Gammel *et al.*, Phys. Rev. Letts **82** No. 8 p1756 (1999)

[13]   A. Knigavko *et al.*, Phys. Rev. B **62** No. 1 p111 (2000)

[14]   S.J. Levett *et al.*, Phys. Rev. B **66** No. 1 p14515 (2002); S.J. Levett *et al.*, Pramana – J. Phys. **58** No. 5-6 p913 (2002)

[15]   P.L. Gammel *et al.*, Phys. Rev. Letts **84** No11 p2497 (2000)

Chapter 8

Summary and Conclusions

In this thesis different aspects of the properties of the rare-earth nickel borocarbides have been investigated through neutron scattering, reinforced by laboratory measurements. The work falls into three categories: the intrinsic properties of the vortex lattice (VL) in the non-magnetic compounds Y- and $LuNi_2B_2C$; the magnetic structures formed in $ErNi_2B_2C$ both with and without the application of a magnetic field; and the VL symmetry transitions and phase diagram in $ErNi_2B_2C$.

In the non-magnetic compounds, the VL was examined through the Fourier components or form factor that governs the intensity of Bragg peaks in SANS experiments. In these materials, the most successful theoretical approach to date incorporates non-local corrections to the London model in order to explain the VL transitions observed in both magnetic and non-magnetic borocarbides. The theory also provides an expression for the form factor. However, our estimation of the ratio of the first two components, F_{11}/F_{10}, in Y- and $LuNi_2B_2C$ produced results (chapter 5) that do not agree well with this theoretical approach. In fact the ratio is much larger than anticipated based on the non-local theory, which in real space corresponds to a less steep drop off of the magnetic field around a flux line than predicted, and is more favourably compared to the standard London model. In addition, as the temperature was increased towards T_C the ratio remained well above the Abrikosov value, which derives from the Ginzburg-Landau theory of superconductivity that should be valid near T_C. Since the anisotropy of the Fermi surface is embedded within the non-local extensions, this failure to tend to the Abrikosov value for F_{11}/F_{10} may be due to another source of anisotropy

107

such as the superconducting gap. Clearly further theoretical efforts will be required to understand both why the current non-local model does not describe the real space variation, and the behaviour at high temperatures. Experimentally, work is in progress to reconstruct the real space VL field distribution with the aid of muon spin rotation data collected from $LuNi_2B_2C$ along with the form factors of higher order Bragg peaks which can be obtained from SANS measurements.

The magnetic properties of $ErNi_2B_2C$ (chapter 6) are important because of the interaction of magnetic order with superconductivity in this material. The development of a low temperature ferromagnetic component has been investigated in zero applied magnetic field. This ferromagnetic component is associated with enhanced pinning of vortices. Changes in the magnetic structure have been observed at both 2.3K, where the increased pinning begins, and at 1.8K. This two-step process has not been observed elsewhere. A model has been developed that provides good agreement with the data collected below 1.8K, although it does not yet account for the behaviour between 1.8K and 2.3K.

The metamagnetic behaviour of $ErNi_2B_2C$ has also been investigated. For fields applied along [2 1 0] and [1 0 0] the number of transitions is greater than expected based on published results, and involve changes in the magnitude of the modulation wave-vector and the distribution of moments, as revealed by the number and intensities of higher order satellites. For these two orientations, though not for fields applied along [1 1 0], a structure similar to a bilayer superlattice is observed in fields in the region of the superconducting upper critical field. No theory has yet been developed to describe the metamagnetic structures, and this should prove a challenging task. Investigations into the VL (via SANS) for fields applied along different directions in the plane may provide the link between the magnetic structures and the behaviour of VL pinning indicated by magnetisation measurements here.

The superconductivity in $ErNi_2B_2C$ was also examined through the vortex lattice (chapter 7). For the first time, the existence of three separate VL phases has been observed in this compound. The second order transition from square to rhombic symmetry has been examined and the critical field, H_2, found to increase overall with increasing temperature. However, H_2 suffers a sharp depression in a narrow temperature range around the magnetic ordering temperature, T_N, in contrast to the smooth increases in H_2 observed in the non-magnetic analogues. This suppression may be related to the changes in the superconducting parameters, normal state electronic properties (via the mean free path) and magnetic susceptibility as magnetic order develops. The slope of H_2 also appears to change markedly on passing T_N. In addition, the low field reorientation (which appears to be of first order) between the two rhombic phases was observed, and this too was found to increase with temperature, which contradicts recent results obtained from the non-magnetic YNi_2B_2C where the reorientation transition field H_1 was shown to decrease slightly with temperature. More detailed data from $ErNi_2B_2C$, as well as the remaining borocarbides, will be required to determine whether this discrepancy is caused by the magnetism in this compound, and whether the onset of magnetic order at T_N impacts on H_1 as it does on H_2.

The rare earth nickel borocarbides continue to throw up new experimental surprises and theoretical challenges, in terms of their superconductivity, magnetic structures and the interaction of the two. Understanding their properties should keep thesis students busy for a while yet.